

Copyright

by

Eunsu Paek

2012

The Dissertation Committee for Eunsu Paek
Certifies that this is the approved version of the following dissertation:

First Principles-based Atomistic Modeling of
the Interfacial Microstructure and Capacitance of Graphene

Committee:

Gyeong S. Hwang, Supervisor

Rodney S. Ruoff

Deji Akinwande

John G. Ekerdt

C. Buddie Mullins

**First Principles-based Atomistic Modeling of
the Interfacial Microstructure and Capacitance of Graphene**

by

Eunsu Paek, B.S.; M.S.Ch.E.

Dissertation

Presented to the Faculty of the Graduate School of
The University of Texas at Austin
in Partial Fulfillment
of the Requirements
for the Degree of

Doctor of Philosophy

The University of Texas at Austin

December

2012

To my mother, Yunnam Kim

Acknowledgements

I would like to gratefully thank my supervisor Dr. Gyeong S. Hwang for his support, patience, and encouragement throughout my graduate studies. I greatly appreciate his giving me an opportunity to pursue my Ph.D. degree in USA, and his guidance was invaluable to me during my years of graduate study at Austin. I thank all the advice he has given me and I am truly grateful for his inspiring way to guide me to become a better scientist. I also thank the other members of my committee: Dr. Rodney S. Ruoff, Dr. Deji Akinwande, Dr. John G. Ekerdt, and Dr. Charles B. Mullins for their invaluable suggestions on my research. I would also like to express my gratitude to my former advisor, Dr. Seung Jong Lee and Dr. Kyung Hyun Ahn, whose passion and education philosophy provided me to establish my stance as a researcher.

I would also like to thank my colleagues as well as the former students in Dr. Hwang's research group. They include Dr. Sangheon Lee, Dr. Kyoung E. Kweon, Yongjin Lee, Alex J. Pak, Dr. Adam Stephens, Chia-Yun Chou, Yu-Hao Tsai, and Dhivya Manogaran. Particularly, I appreciate Dr. Kyoung E. Kweon and Yongjin Lee for their advice always cheered me up whenever I struggled, and I also appreciate Alex J. Pak for his valuable discussions and helping me to solve my problems.

I would also like to express my gratitude to my friends outside of the lab who made my graduate school experience memorable. I thank Taehyun Kang, Dr. Kiyoul Yoon, Sun-mi Lee, Jongsuk Kim, Dr. Cheulhee Jung, Heejung Oh, Jiwon Lee, Minjung Kim, Jungup Park, Jaesung Park, Euisung Jang, and Chaebin Kim. Especially, I

appreciate Heejung Oh for her close friendship and encouragement during my graduate studies.

I would also like to express my gratitude to Rev. Ted Kim at the Immanuel church of Austin. He always guided me to the right way and cheered me up spiritually and mentally whenever I spent hard times.

More importantly, I would like to thank all of my family for all the love and support that they have given me through my graduate school life. I would like to thank my sister Yunhwa Paek, Heejung Paek, and my brother Jongsup Paek. I especially thank my parents for their unconditional love and support to me studying far away from home.

Eunsu Paek

The University of Texas at Austin

December 2012

First Principles-based Atomistic Modeling of the Interfacial Microstructure and Capacitance of Graphene

Publication No. _____

Eunsu Paek, Ph. D.

The University of Texas at Austin, 2012

Supervisor: Gyeong S. Hwang

Graphene has been extensively studied for possible future technical applications due to its unique electronic, transport, and mechanical properties. For practical applications, graphene often needs to be placed in a medium or on a substrate. The interfacial interaction between graphene and other materials can greatly affect the performance of graphene-based devices, but has not been well explored. My thesis research focused on developing a better understanding of the interface of pristine and chemically/mechanically modified graphene sheets with ionic liquids (ILs) as well as amorphous silica (α -SiO₂) surfaces using first principles-based atomistic modeling which combines density functional theory, classical molecular dynamics, and Metropolis Monte Carlo.

The major focus of my thesis research was on investigating the interfacial structure and capacitance between graphene and ILs; graphene-based materials and ILs have been regarded as viable candidates for supercapacitor electrodes and electrolytes, respectively. Particular emphasis was placed on elucidating the relative contributions of the electric double layer (EDL) capacitance at the graphene/IL interface and the quantum capacitance of graphene-like electrodes. More specifically, we first determined the microstructure (such as orientation, packing density, cation-anion segregation) of chosen ILs near planar graphene electrodes with various surface charge densities. Based on the calculated IL microstructure for each system, the EDL capacitance was then evaluated with particular attention to the effect of cation-anion size difference. We also examined the influence of the chemical and mechanical modifications of graphene-like electrodes on the supercapacitor performance. Especially, mechanisms underlying chemical doping-induced enhancement of the total interfacial capacitance were addressed through analysis of electrode quantum capacitance changes resulting from electronic structure modifications. A part of my effort was also devoted to examining the binding interaction of graphene with α -SiO₂ (which is not yet clearly understood despite its scientific and technological importance). In particular, we attempted to evaluate quantitatively the adsorption strength of graphene on the α -SiO₂ surface, which has been under debate mainly due to the difficulty of direct measurement.

Table of Contents

| | |
|--|------|
| List of Tables..... | xii |
| List of Figures..... | xiii |
| Chapter 1: Introduction..... | 1 |
| Chapter 2: Supercapacitor Background..... | 6 |
| 2.1 Electric Double Layer Structure..... | 9 |
| 2.2 Electric Double Layer Capacitance..... | 10 |
| 2.3 Quantum Capacitance..... | 11 |
| Chapter 3: Theoretical Backgrounds..... | 13 |
| 3.1 Molecular Dynamics..... | 13 |
| 3.1.1 Fundamentals..... | 13 |
| 3.1.2 Classical Force Fields..... | 16 |
| 3.2 Metropolis Monte Carlo Bond Switching Method..... | 21 |
| 3.2.1 Valence Force Field Model..... | 21 |
| 3.2.2 Parameter Determination..... | 22 |
| 3.2.3 Metropolis Monte Carlo Simulation..... | 25 |
| 3.3 First Principles Quantum Mechanics..... | 27 |
| 3.3.1 Density Functional Theory..... | 28 |
| 3.3.2 Grimme's DFT-D2 Method..... | 29 |
| Chapter 4: Microstructure of Ionic Liquid/Graphene Interfaces..... | 31 |
| 4.1 Introduction..... | 31 |
| 4.2 Computational Methods..... | 33 |
| 4.3 Molecular Distribution of [BMIM][PF ₆] Ionic Liquid..... | 35 |
| 4.3.1 Near Uncharged Graphene Electrodes..... | 35 |
| 4.3.2 Near Charged Graphene Electrodes..... | 37 |

| | |
|---|-----|
| 4.3.3 Electrode Charge Screening and Cation-Anion Segregation..... | 42 |
| 4.4 Molecular Orientation of [BMIM][PF ₆] Ionic Liquid..... | 44 |
| 4.4.1 Near Uncharged Graphene Electrodes | 44 |
| 4.4.2 Near Charged Graphene Electrodes | 46 |
| 4.5 Anion Size Dependence of Interfacial Ionic Liquid Structure..... | 50 |
| 4.6 Summary..... | 54 |
| Chapter 5: Capacitance of the Ionic Liquids/Graphene Interfaces..... | 56 |
| 5.1 Introduction..... | 56 |
| 5.2 Computational Methods..... | 59 |
| 5.3 Results and Discussion..... | 59 |
| 5.3.1 Electric Double Layer Capacitance..... | 62 |
| 5.3.2 Electrode Quantum Capacitance..... | 64 |
| 5.3.3 Total Interfacial Capacitance..... | 67 |
| 5.4 Anion Size Dependence of Electric Double Layer Capacitance | 70 |
| 5.5 Summary..... | 74 |
| Chapter 6: Nitrogen Doping Effect on Capacitance Enhancement | 77 |
| 6.1 Introduction..... | 77 |
| 6.2 Computational Methods..... | 79 |
| 6.2.1 Density Functional Theory..... | 79 |
| 6.2.2 Classical Molecular Dynamics..... | 81 |
| 6.3 Results and Discussion..... | 84 |
| 6.3.1 Electrode Quantum Capacitance..... | 84 |
| 6.3.2 Electric Double Layer Capacitance..... | 90 |
| 6.3.3 Total Interfacial Capacitance..... | 96 |
| 6.4 Summary..... | 99 |
| Chapter 7: Graphene Adhesion on Amorphous Silica..... | 101 |
| 7.1 Introduction..... | 101 |
| 7.2 Computational Methods..... | 103 |

| | |
|--|-----|
| 7.2.1 Graphene/SiO ₂ Interface Structure Optimization..... | 103 |
| 7.2.2 Van der Waals Parameter Determination..... | 105 |
| 7.3 Results and Discussion..... | 107 |
| 7.3.1 Surface Structure of Amorphous Silica..... | 107 |
| 7.3.2 Structure and Adhesion Strength at Graphene/SiO ₂ Interfaces. | 110 |
| 7.3.3. Morphological Conformity Effect..... | 114 |
| 7.4 Summary..... | 118 |
| Chapter 8: Summary..... | 120 |
| Bibliography..... | 122 |
| Vita..... | 133 |

List of Tables

| | | |
|------------|---|-----|
| Table 2.1: | Advantages and disadvantages of batteries and supercapacitors..... | 7 |
| Table 3.1: | Parameters of the valence force field model employed in this work, which were adjusted to fit DFT-GGA calculations. Units are given in eV..... | 25 |
| Table 4.1: | Predicted peak and average densities of counterions in the first IL layer from electrodes with different charge densities..... | 42 |
| Table 4.2: | Charge densities ($q_{net} = q_- + q_+$), screening parameter (β), and counterion mixing parameter (χ) in the first counterion layer from electrodes with different charge densities..... | 43 |
| Table 6.1: | Calculated partial atomic charges of substitutional N and neighboring C atoms at specified surface charge densities..... | 80 |
| Table 6.2: | Calculated partial atomic charges of pyridine-type N and neighboring C atoms at specified surface charge densities..... | 80 |
| Table 6.3: | Potential drop across the EDL (ϕ_D) and integral capacitance (C_I) for pristine, N ₁ , and N ₃ V graphene systems at $\sigma = \pm 5.43 \mu\text{C}/\text{cm}^2$ | 93 |
| Table 7.1: | 12-6 Lennard-Jones (LJ) Parameters employed in this work | 106 |
| Table 7.2: | Standard deviations of height distributions (σ) of graphene sheets and α -SiO ₂ surfaces, graphene- α -SiO ₂ distances (d_{Gr-SiO_2}) and van der Waals interaction energies (E_{vdW}), and graphene strain energy (E_{st}); 18 different α -SiO ₂ model surfaces are considered. The values are calculated using LJ(DFT-D2) / LJ(Charmm) / LJ(Dreiding) parameter sets..... | 108 |

Table of Figures

- Figure 2.1: Ragone plot which shows the relation between the energy density and power density of the electric energy storage devices..... 8
- Figure 2.2: (a) Schematic of the electric double layer when the electrode is charged positively (b) Potential profile of the electric double layer according to the Gouy-Chapman-Stern model along the direction normal to the electrode surface..... 10
- Figure 3.1: Internal coordinates for bonded interactions: r_i describes bond stretching, θ_i represents the angle term, ϕ_i represents the dihedral angle, the χ_i describes out-of-plane improper dihedral angle..... 17
- Figure 3.2: Training sets used in parameter optimization: (a) k_r from energy variation (per C-C bond) with respect to lattice constant in graphene; (b) k_θ from Stone-Wales (SW) defect in graphene; and (c) k_ϕ and k_ψ from two different sizes of fullerene (C_{36} and C_{60}) and two different nanotube structures [armchair (5,5) and zigzag (8,0)]. Black (blue) filled circles represent atoms comprising 5-membered rings, gray (gold) filled circles are atoms included in 7-membered rings but not in 5-membered rings, and unfilled circles indicate the rest of the lattice atoms..... 23
- Figure 3.3: Illustration of a MC bond-rotation move that involves the 90° rotation of a single bond (B-C) by breaking two bonds (A-B and C-D) and forming two new bonds (A-C and B-D); this bond rotation yields a Stone-Wales (SW) defect (right)..... 27
- Figure 4.1: Schematic of the ionic liquids used in this simulation. (a) BMIM⁺ (1-butyl-3-methylimidazolium), (b) PF₆⁻ (hexafluorophosphate), (c) Cl⁻, (d) TFSI (bis-trifluoromethylsulfonamide)..... 32
- Figure 4.2: Schematic the simulation box. Planar graphene sheets are placed at the two ends of the simulation domain. Periodic boundary conditions are applied in the x and y directions. (a) and (b) represent snapshots when (a) uncharged graphene electrode (b) charged graphene electrode are employed..... 34

- Figure 4.3: Total, BMIM, and PF₆ mass density (ρ_m) profiles along the z-axis near an uncharged graphene electrode which is located at $z = 0$ 36
- Figure 4.4: BMIM and PF₆ mass density (ρ_m) profiles along the z-axis near charged graphene electrodes with different excess charge densities (σ) as specified (in $\mu\text{C}/\text{cm}^2$). Each electrode is located at $z = 0$. The inset in (a) shows the distributions of F and P atoms. 38
- Figure 4.5: Snapshots of counterions in the layer closest to charged electrodes with different excess charge densities as specified (in $\mu\text{C}/\text{cm}^2$); (a)-(c) PF₆, (d)-(f) BMIM. Thin gray lines depict the graphene lattice, and red/pink clusters (left panels) and gray/blue sticks (right panels) represent PF₆ and BMIM, respectively. 39
- Figure 4.6: Space charge density (ρ_q) profiles due to BMIM and PF₆ along the z-axis near charged electrodes with different excess charge densities as specified (in $\mu\text{C}/\text{cm}^2$). Each electrode is located at $z = 0$ 41
- Figure 4.7: Order parameter $\langle P_2(\cos\theta) \rangle$ profiles for BMIM along the z-axis for the angles of the ring plane and butyl chain with respect to the graphene surface normal. 45
- Figure 4.8: Probability distributions for the BMIM ring normal angle with respect to the graphene surface normal in the first IL layer at varying electrode charge as specified (in $\mu\text{C}/\text{cm}^2$). 47
- Figure 4.9: Probability distribution for the BMIM ring normal angle with respect to the graphene surface normal in the BMIM layer adjacent to a negatively charged graphene at $\sigma = -40 \mu\text{C}/\text{cm}^2$. The inset shows the corresponding number density profile of the BMIM ring atoms, suggesting that BMIM forms two sub-layers as indicated by (a) and (b). 48
- Figure 4.10: Number density ($\rho_{\#}$) profiles of butyl chain atoms (C1-C4) along the z-axis near graphene electrodes with different charge densities (σ) as specified (in $\mu\text{C}/\text{cm}^2$). The inset in each panel illustrates how BMIM and PF₆ ions orient near the electrode. 49
- Figure 4.11: Mass density distributions of [BMIM][Cl] at the positive electrode. Different excess charge densities are specified in $\mu\text{C}/\text{cm}^2$. Each electrode is located at $z = 0$. Snapshots displayed to the right correspond

| | |
|---|----|
| to Cl anions in the first adsorbed layer at the specified charge density..... | 51 |
| Figure 4.12: Mass density distributions of [BMIM][TFSI] at the positive electrode; (a)-(c) [BMIM][TFSI] and (d)-(f) distributions of N, S, O, C and F atoms of TFSI anion. Different excess charge densities are specified in $\mu\text{C}/\text{cm}^2$. Each electrode is located at $z = 0$. Molecular configurations displayed to the right correspond to TFSI anions at the specified charge density..... | 52 |
| Figure 5.1: Potential (ϕ) profiles along the z -axis at varying excess charge densities as specified (in $\mu\text{C}/\text{cm}^2$). To facilitate comparisons, the ϕ near the negative graphene electrode is shown on a negative scale, i.e. the shown $\phi = -\phi$. In all cases, $\phi = 0$ for the bulk electrolyte and each electrode is located at $z = 0$ | 61 |
| Figure 5.2: (a) Excess electrode charge density (σ) and (b) differential double layer capacitance (C_D) as a function of the potential drop across the EDL (ϕ_D). In (a), the circles represent data from MD simulations and the solid line is fit from smoothing the data..... | 63 |
| Figure 5.3: Comparison of pristine graphene's density of states (DOS) from theory, experiment and DFT..... | 66 |
| Figure 5.4: Calculated quantum capacitance (C_Q) of pristine graphene based on the DOS (inset). $E = 0$ eV indicates the position of the Fermi level..... | 67 |
| Figure 5.5: Schematic of the graphene/IL interface, with an illustration of the equivalent circuit with series capacitance from the electrode and double layer [(a)] and an idealized potential profile [(b)]..... | 68 |
| Figure 5.6: Total interfacial capacitance (C_T) as a function of applied potential (ϕ_a). The inset shows corresponding EDL capacitance (C_D) and quantum capacitance (C_Q)..... | 69 |
| Figure 5.7: Potential profiles for (a) [BMIM][Cl] and (b) [BMIM][TFSI] at the positive electrode with specified surface charge densities. Each electrode is located at $z = 0$ | 71 |

- Figure 5.8: Differential double layer capacitance (C_D) as a function of potential drop across the EDL (ϕ_D); (a) [BMIM][Cl] and (b) [BMIM][TFSI]. Insets show excess electrode charge density.....73
- Figure 6.1: Schematic of the (a) substitutional nitrogen site (N_1) and (b) trimerized pyridine-type nitrogen site (N_3V). Gray and blue balls are C and N atoms, respectively, and bond lengths are in Å..... 79
- Figure 6.2: Schematic of BMIM, PF_6 , and the simulation box. Planar graphene sheets are placed at the two ends of the simulation domain. White, blue, and gray balls indicate H, N, and C atoms in BMIM, and red and pink balls indicate P and F atoms in PF_6 . Periodic boundary conditions are applied in the x and y directions.....82
- Figure 6.3: Color map (2D) showing the excess charge distribution on neutral (a) N_1 and (b) N_3V graphene. The excess charge is obtained from Bader charge analysis from DFT and plotted using the filled contour plot option in SigmaPlot 12; each region is linearly interpolated with a discrete value of excess charge (in e) as indicated by the color legend.....83
- Figure 6.4: Band structures (left panels) and electronic density of states (right panels) for (a) pristine, (b) N_1 , and (c) N_3V graphene. The dotted red line (left panels) indicate the Fermi level position. The insets (left panels) show the band-decomposed charge density isosurfaces for their respective shaded regions above and below the Fermi level ($\pm 0.0005 e/\text{Å}^3$)..... 86
- Figure 6.5: Comparison of the calculated quantum capacitance (C_Q) of pristine, N_1 , and N_3V graphene as a function of the local electrode potential (ϕ_G).....88
- Figure 6.6: The calculated quantum capacitance (C_Q) for the mixed N-dopant configurations shown in the right panels; (a) N_3V and single N_1 , (b) N_3V and two N_1 , and (c) N_3V and three N_1 89
- Figure 6.7: BMIM and PF_6 mass density (ρ_m) profiles for (a) pristine, (b) N_1 , and (c) N_3V graphene systems along the z -axis. The positive (negative) electrode is located at $z = 0$ Å (100 Å)..... 91

- Figure 6.8: Potential (ϕ) profiles along the z -axis at $\sigma = \pm 5.43 \mu\text{C}/\text{cm}^2$ for the pristine graphene system. The positive (negative) electrode is located at $z = 0 \text{ \AA}$ (100 \AA) and $\phi = 0$ for the bulk electrolyte..... 92
- Figure 6.9: Excess charge density isosurfaces ($\pm 0.0003 e/\text{\AA}^3$) for N_1 and N_3V graphene at varying σ (in $\mu\text{C}/\text{cm}^2$)..... 94
- Figure 6.10: Snapshot of the IL ions closest to the electrode at various excess charge densities (in $\mu\text{C}/\text{cm}^2$). Thin gray sticks depict the graphene lattice. The red/blue clusters and blue/gray sticks represent PF_6 and BMIM, respectively. The BMIM rings have a tendency to lie near the N sites, which are shown as red balls..... 95
- Figure 6.11: The differential double layer capacitance (C_D) as a function of the potential drop across the EDL (ϕ_D) for the pristine graphene system..... 97
- Figure 6.12: (a) Schematic of the idealized potential profile at the graphene/IL interface, and the total interfacial capacitance for (b) pristine, (b) N_1 , and (c) N_3V graphene systems as a function of applied potential (ϕ_a). The insets show relative contributions between C_D and C_Q as a function of ϕ_a 98
- Figure 7.1: (a) Initial configuration of SiO_2 slab, (b) defect-free $a\text{-SiO}_2$ slab structure constructed using continuous random network model based Metropolis Monte Carlo (CRN-MMC) simulations, (c) relaxed graphene/ $a\text{-SiO}_2$ interface structure; two single graphene sheets are placed on the bottom and top surfaces of the $a\text{-SiO}_2$ slab..... 104
- Figure 7.2: DFT-D2 values for the graphene/ $a\text{-SiO}_2$ interaction energy used for LJ parameter optimization. The interaction energies from various force fields as indicated are also plotted for comparison purpose..... 107
- Figure 7.3: Radial distribution functions (RDF) for Si-Si, Si-O, and O-O pairs in $a\text{-SiO}_2$ bulk [(a)] and surface layer [(b)], as illustrated in the insets..... 109
- Figure 7.4: Energy diagram that describes separation of a graphene sheet from a rough surface. (A) graphene on $a\text{-SiO}_2$, (B) work of separation ($W_{sp} = E_{vdW}$) which is required to separate the graphene sheet, (C) adhesion

energy (E_{ad}) which is obtained by taking into account the structural relaxation of graphene after separation.....111

Figure 7.5: Predicted standard deviations of height distributions of graphene (σ_{Gr}) with respect to the a -SiO₂ surface (σ_{SiO_2}) for three parameter sets of LJ parameters employed... 113

Figure 7.6: Variations in the graphene/ a -SiO₂ vdW interaction energy (E_{vdW}) and distance (d_{Gr-SiO_2}) for the selected a -SiO₂ surface with $\sigma_{SiO_2}=3.65\text{\AA}$ and various morphologies of graphene. Selected graphene/ a -SiO₂ interface structures [(A)-(C) as indicated in (b)] are shown in the upper panels..... 115

Figure 7.7: Fast Fourier Transform-based morphological analysis of graphene and a -SiO₂ surface for three different adhesion conditions; (a) optimal, (b) less corrugated, and (c) more corrugated. Corresponding surface contour plots are also shown as insets..... 117

Chapter 1: Introduction

Graphene is a single atomic layer of sp^2 -bonded hexagonal carbon atoms. Although the atomic structure and electronic properties of graphene were theoretically predicted by Wallace in 1947 [1], its fabrication and identification was first done by Geim and coworkers in 2004 [2]. They used a mechanical exfoliation method with Scotch tape to separate a few layers of graphene from a graphite crystal and characterized it by atomic force microscopy (AFM). Since its discovery, graphene has received great attention for potential technical applications due to its unique electronic, transport, and mechanical properties. Extensive experimental and theoretical studies have been undertaken to obtain a fundamental understanding of the synthesis, manipulation and characterization of graphene-based materials, and further expand knowledge on graphene-based device applications. Among many applications, graphene is a potential electrode for supercapacitors particularly due to its high specific surface area of $\sim 2600 \text{ m}^2/\text{g}$. In addition, graphene can be used as a high-performance transistor due to its relatively higher electron conductivity compared to silicon. For those applications, graphene cannot be used as a single freestanding layer; it should be in contact with electrolytes or gate dielectric materials, respectively.

The main goal in the research of supercapacitors is to increase their capacitance in order to enhance the energy density. The interfacial capacitance of graphene in an electrolyte may be governed by $1/C=1/C_Q+1/C_D$ in which C_Q is the quantum capacitance of the graphene electrode and C_D is the capacitance of the electric double layer (EDL) at

the interface. At a semiconductor (or semimetallic) electrode-electrolyte interface, the space charge layer within the electrode act as a capacitor in series with the EDL; likewise, at the graphene-electrolyte interface, the graphene electrode capacitance need to be taken into account. The C_Q of graphene-like materials is directly proportional to the electronic density of states (DOS), and can therefore be enhanced through electronic structure modification by imparting functional groups and impurities and creating corrugations and topological defects. C_D strongly depends on the microstructure of the EDL, thus knowing the electrolyte and electrode structure is important. Ionic liquids (ILs) are excellent electrolytes due to their high chemical tunability, large electrochemical window, low volatility, high thermal stability, and good solvation potential. In the graphene/IL system, both C_Q and C_D make important contributions to the total interfacial capacitance and hence, both must be increased.

In order for graphene to be used for electronic applications, it needs to be supported by a substrate in many cases. Therefore, graphene/substrate interface is of great importance. Amorphous silicon dioxide ($a\text{-SiO}_2$) is an important supporting dielectric material for graphene in many applications e.g. graphene transistor. When graphene is deposited on a $a\text{-SiO}_2$ surface, previous experiments have demonstrated that it is weakly adhered to the $a\text{-SiO}_2$ surface without forming covalent bonds. In addition, many AFM studies have shown that graphene morphology is highly conformal to the topology of the underlying $a\text{-SiO}_2$ surface. In this case, the corrugation of graphene can alter the properties of graphene, such as carrier mobility lowering which could deteriorate the performance of electronic devices. Therefore, the interfacial structure, energetics,

electronic properties must be carefully examined for use of graphene-based materials in targeted applications. However due to the limited capability of current instruments for direct characterization, an atomic level understanding derived from experimental methods tends to be still be far remained elusive. A complementary computational effort is necessary to better understand the interface of graphene with other materials.

Our work focused on developing a better understanding of the nature and behavior of graphene/ILs and graphene/*a*-SiO₂ interfaces using first principles-based atomistic simulations. The content of this dissertation is outlined as follows. In Chapter 2, we present a description of background knowledge for supercapacitors. In Chapter 3, computational methods used in this dissertation work are described, including molecular dynamics (MD), density functional theory (DFT), and Metropolis Monte Carlo (MMC).

In Chapter 4, we present the microstructure of ILs ([BMIM][PF₆], [BMIM][TFSI], [BMIM][Cl]) at the pristine graphene interface based on molecular dynamics calculations. First, the interfacial structure of [BMIM][PF₆] near the graphene electrode with varying charge densities are investigated to provide a molecular description of EDLs, including [BMIM][PF₆] packing and orientation, cation-anion segregation, and electrode charge screening. The microstructure of ILs with different anions is also investigated in terms of differences in packing and orientation.

In Chapter 5 we present the interfacial capacitance between planar graphene and various ILs ([BMIM][PF₆], [BMIM][TFSI], [BMIM][Cl]), with particular attention to the relative contributions of the EDL capacitance at the graphene/IL interface and the quantum capacitance of graphene. Based on the calculated distributions of ILs, we

evaluate the potential variations in ILs and obtain EDL differential capacitances. Then, we employ DFT calculations to estimate the quantum capacitance of pristine graphene with a brief comparison to theoretically predicted and experimentally estimated values. While the total interfacial capacitance is given as a series of the EDL capacitance and the quantum capacitance, our work clearly demonstrates that the quantum capacitance can play a major role in determining the overall performance of graphene/IL-based supercapacitors.

In Chapter 6 we present the influence of N-doping on the interfacial capacitance for [BMIM][PF₆] IL using combined DFT and classical MD calculations. Our particular interest lies in understanding the relative contributions of EDL capacitance and quantum capacitance to the total interfacial capacitance for the N-doped graphene case as compared to the undoped case. We separately investigate two commonly observed N-configurations from experimental characterization: (1) substitutional N in which a C atom is replaced with a N atom and (2) trimerized pyridine-type N in which three two-coordinated N atoms surround a vacancy. We first employ DFT to predict the impact of each type on the electrode quantum capacitance, which is proportional to the electron density of states. We then consider the impact of N-doping on the microstructure, potential variation, and the EDL capacitance. This study suggests that N-doping enhances the quantum capacitance as a result of electronic structure modifications, while the double layer capacitance is virtually unaffected.

In Chapter 7 we examine the structure and adhesion energy of graphene on *a*-SiO₂ using force field calculations. The van der Waals (vdW) interaction between graphene

and $a\text{-SiO}_2$ is computed by employing three different sets of vdW parameters which were extracted from the Charmm and Dreiding force fields and by fitting to semiempirical dispersion corrected DFT calculations. Continuous Random Network model-based Metropolis Monte Carlo (CRN-MMC) simulations are performed to prepare defect-free $a\text{-SiO}_2$ surface models with various degrees of surface roughness; the $a\text{-SiO}_2$ surface structures are analyzed in terms of surface height distribution and Si/O spatial distribution. For different surface morphologies of $a\text{-SiO}_2$, we determine the topology of graphene that leads to the optimal adhesion on each $a\text{-SiO}_2$ surface; the graphene/ $a\text{-SiO}_2$ interface structure is used to estimate the adhesion energy (which is given in terms of the vdW interaction energy between graphene and $a\text{-SiO}_2$ and the strain energy of corrugated graphene on $a\text{-SiO}_2$). Finally we also look at the sensitivity of the adhesive strength to the change of morphological conformity between graphene and $a\text{-SiO}_2$.

In Chapter 8 we summarize this thesis work.

Chapter 2: Supercapacitor Background

There have been increasing demands for electrical energy as the world's population has increased from 2.5 billion to 6.8 billion over the last 50 years, and the demands are expected to continuously increase [3,4]. Nowadays, most of the electrical energy consumed depends on fossil fuels such as coal, gasoline, and natural gas. They are relatively cheap and abundant, but most of these technologies – such as gasoline extraction – are approaching the limits for development. In addition, they emit carbon dioxide, cause acid rain, and have limited resources. Therefore, there is high demand for clean, efficient, and renewable energy sources such as solar- or wind- based energies to replace fossil fuels. However, energy generated from renewable energy does not coincide with the energy use cycle, which makes electrical energy storage (EES) systems essential to store energy for on-demand usage [5]. For example, electricity generated through solar-cells during the daytime can be stored in EES and be used at night when it is needed. Furthermore, EES plays an important role in alleviating short-term fluctuations of electricity demands, which are currently a major source of inefficiency for the grid. In addition, EES systems can be used in hybrid electric vehicles which can mitigate CO₂ emission. Recent high demands for portable devices such as cellular phones and laptop computers also focus on the performance of EES devices.

Electric double layer capacitors (EDLCs) as well as batteries are the most essential technologies among all electric energy storage (EES) devices [6]. While both technologies are electrochemical in nature, they store electric charge in different ways;

Table 2.1 Advantages and disadvantages of batteries and supercapacitors [6].

| | Battery (Li-ion) | Supercapacitors |
|-----------------------------|------------------|-----------------|
| Storage mechanism | Chemical | Physical |
| Specific Energy (Wh/kg) | 10~100 | 1~10 |
| Specific Power (kW/kg) | <1 | 5~10 |
| Charge/Discharge time | 5min ~ 3hours | 1~30 sec |
| Cycle life | 10~50K | >1000K |
| Charge/Discharge efficiency | 0.7~0.85 | 0.85~0.98 |
| Cost (\$/kW) | 75~150 | 25~50 |

batteries store energy by utilizing redox reactions, while EDLCs store energy as charge directly. The advantages and disadvantages of batteries and EDLCs are tabulated in Table 2.1. Although both do not meet today's energy requirements, batteries are widely used in portable electronic devices, enabling our lives to be more convenient. However, batteries often contain harmful materials that can pollute the earth, and also have relatively short cycle-life and low power density. EDLCs show excellent power density (fast charging/discharging time), almost unlimited cycle-life (>100K), large charge/discharge efficiency, and safe charge/discharge processes compared to those of batteries. Therefore, EDLCs are an attractive complement or replacement for traditional batteries [7]. However, the energy density of current state-of-the-art EDLCs must be improved to make them viable options for next-generation EES.

The energy density of EDLCs can be obtained by $E=1/2CV^2$ where C is the capacitance in Farads and V is the usable operating voltage. Two major goals of researchers are to find materials to enhance the capacitance and expand the electrochemical window (V) in order to enhance the energy density. Most commercial

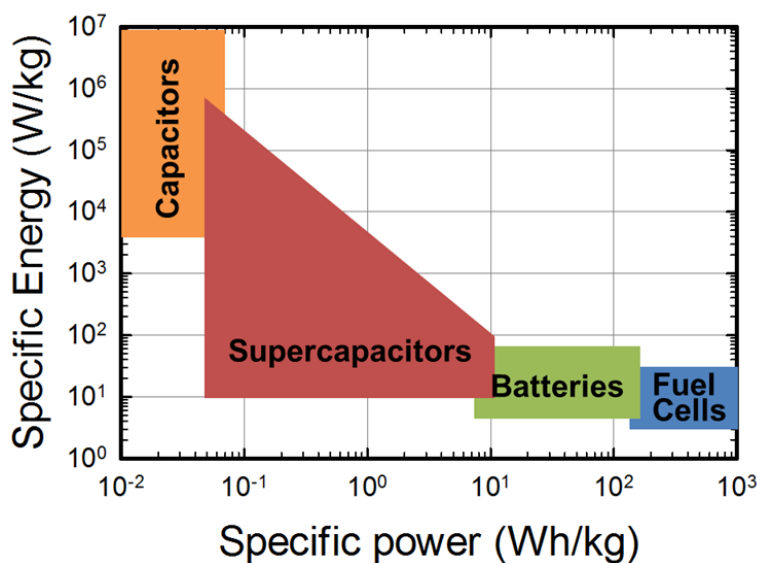


Figure 2.1 Ragone plot which shows the relation between the energy density and power density of the electric energy storage devices.

EDLCs are based on carbon-based materials as the electrode because they are cheap and have versatile forms such as powders, fibers, and foils. Among them, activated carbon is the most favorable electrode material. While aqueous or organic solutions are commonly used as the electrolyte, ionic liquids are a relatively new class of electrolyte with many unique and useful properties. They exhibit high thermal and chemical stability, extremely low volatility, non-flammability, and wide electrochemical windows [8,9], and the IL's properties are highly tunable through the choice of the cation and anion pair [10].

As the voltage is applied to the electrode, the resultant electrostatic forces make the ions accumulate and rearrange at the interface into the most energetically favorable state by effectively screening the electric field. Capacitance is the capability to store charge responding to an applied voltage ($C=Q/V$). The total capacitance (C_{total}) at the

interface of EDLCs can be obtained by the sum of the reciprocal of C_Q and C_{EDL} ($1/C_{total} = 1/C_Q + 1/C_{EDL}$) as the electrode and EDL are assumed to be linked in series. Here, C_{EDL} is the capacitance which arises from the electrolyte side, while C_Q (quantum capacitance) is the capacitance of the electrode itself. The smaller capacitance of the two dominates C_{total} , so both C_Q and C_{EDL} should be taken into account when they are comparable [11]. In order to better understand the underlying mechanism of charge storage and guide the rational design of electrode/electrolyte materials, it is crucial to understand the interfacial behavior during charge/discharge processes.

2.1 Electric Double Layer Structure

When the electrode is charged, the EDL is formed as illustrated in Figure 2.2 (specific adsorption is not considered). One charged layer in the electrode and the other charged layer in the electrolyte behave like a physical capacitor. The EDL in the solution side shows several layers [12]. The innermost layer is the so-called Helmholtz, compact, or Stern layer and it ranges from the electrode surface to the center of the nonspecifically adsorbed counterions. There is no covalent bonding between electrolyte and electrode, so their interaction mainly depends on the electrostatic force. Next to the Helmholtz layer, excess counterions are distributed due to thermal agitation of solution, and this layer is called the diffuse layer. The diffuse layer ranges from the Helmholtz layer to the bulk electrolyte; it is in general a few nanometers depending on the ionic concentration and temperature of the solution. The sum of total excess charge in the Helmholtz and diffuse layers is equivalent to the excess charge in the electrode.

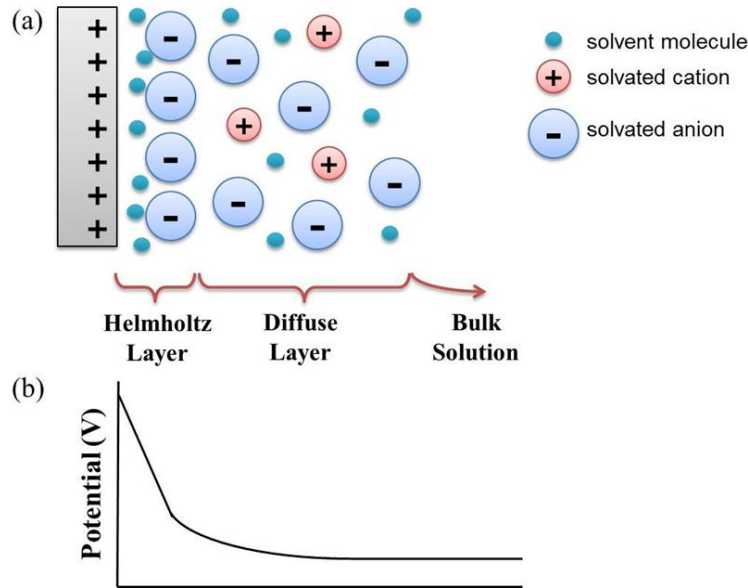


Figure 2.2 (a) Schematic of the electric double layer when the electrode is charged positively (b) Potential profile of the electric double layer according to the Gouy-Chapman-Stern model along the direction normal to the electrode surface.

2.2 Electric Double Layer Capacitance

The potential profile along the direction normal to the electrode surface is illustrated in Figure 2.2 (b) according to the Gouy-Chapman-Stern model [13]. It falls off abruptly in the Helmholtz layer while maintaining a linear trend. However, the potential drop becomes gentle at the diffuse layer. The potential becomes constant at the bulk electrolyte because ions are no longer affected by the surface charge due to complete shielding by the EDL. In the MD simulations, electric potential (ϕ_D) profiles along the surface normal direction can be obtained by solving Poisson's equation, $\nabla^2 \phi(z) = \rho(z) / \epsilon_0$ with $-\nabla \phi|_{ES} = E_{ES}$ where z is the distance from the electrode, ρ is the charge density

averaged over a lateral z -cross section, and ϵ_0 is the vacuum permittivity. The EDL capacitance (C_D) can be obtained from the relationship between σ and ϕ_D , i.e., $C = \sigma/\phi_D$ (integral) or $d\sigma/d\phi_D$ (differential). The differential capacitance is a measure of how the EDL microstructure responds to potential perturbations caused by a variation in σ . Hence, the differential approach is often preferred in investigating the properties of EDLs. The capacitance can be tailored based on the electrolyte materials; however, it is unclear which specific ion-ion and ion-electrode interactions influence the structure and capacitance of EDLs.

2.3 Quantum Capacitance

At a semiconductor (or semimetallic) electrode-electrolyte interface, the space charge layer within the electrode may act as a capacitor in series with the EDL. Likewise, at the IL/carbon interface the carbon electrode capacitance might need to be taken into account for the interfacial capacitance. The quantum capacitance of graphene is defined as $C_Q = d\sigma/d\phi_G$, where $d\sigma$ and $d\phi_G$ refer to the variations of charge density and local potential in graphene, respectively. The quantum capacitance of carbon nanostructures is directly proportional to the DOS. For the pristine graphene sheet, the DOS is symmetric and linear around the Fermi level (E_F). With the analytical expression of σ , the C_Q of graphene is given by:

$$C_Q = d\sigma / d\phi_G = e^2 \int_{-\infty}^{+\infty} D(E) F_T(E - \mu) dE \quad (2.1)$$

where the thermal broadening function [$F_T(E)$] is also expressed as

$$F(E) = \frac{1}{4k_B T} \operatorname{sech}^2 \left(\frac{E}{2k_B T} \right) \quad (2.2)$$

where $D(E)$ is the 2D DOS, E is the relative energy with respect to E_F , e is the elementary charge.

For metallic electrodes with large free electron densities, the C_Q is much larger than C_{EDL} so that the contribution of C_Q can be ignored; hence, C_T is solely determined by C_{EDL} . However, for graphene-like electrodes, C_Q is comparable to C_{EDL} . This explains why the C_T of graphene-like materials is usually much smaller than that of metal electrodes, while exhibiting a peculiar U shape near the potential of zero charge (PZC) [14,15]. While both C_Q and C_{EDL} must be increased to enhance C_T , the C_Q of graphene-like electrodes could be enhanced through electronic structure modifications by creating corrugations and topological defects and imparting functional groups and impurities, but no detailed study has been undertaken to examine the effects of structural disorder and chemical functionalization.

Chapter 3: Theoretical Backgrounds

3.1 Molecular Dynamics

Molecular dynamics (MD) is a computer simulation method which calculates time-dependent trajectories of molecular systems by numerically solving Newton's equation of motion. This method was first introduced in the 1950's by Alder and Wainwright [16,17] to study the behavior of hard spheres, followed by further investigations of simple liquid systems. The first MD simulation of realistic systems was performed in 1970's by Stillinger and Rahman [18] using liquid water. Since then, MD simulations have been extensively carried out to describe diverse materials; contemporary MD simulations are widely used to model biophysical systems in order to address a variety of structural, thermodynamic, and transport properties.

3.1.1 Fundamentals

The Newton's equation of motion is given by

$$\mathbf{F}_i = m_i \mathbf{a}_i \quad (3.1)$$

where \mathbf{F}_i and \mathbf{a}_i are the force and acceleration vectors for a particle i , and m_i is the mass of a particle i . This equation relates the force exerted on a particle to the position and momentum with time.

$$\begin{aligned} F_i &= \frac{dp_i}{dt} \\ \frac{p_i}{m_i} &= \frac{dr_i}{dt} \end{aligned} \tag{3.2}$$

Here, p_i and r_i are the momentum and position vectors for a particle i . Once the force exerted on an atom is obtained, the velocity and position can be calculated by integrating the equation of motion using proper methods such as the velocity Verlet algorithm [19]. Most MD simulations are performed under constraints such as constant N , P , T conditions or constant N , V , T conditions in order to better describe experimental environments [how? There are many different ways to do this. Boundary conditions are also an important consideration].

A simplified description of the procedure for MD simulations is as follows. Initial configurations for the system of interest are created; this process should be done very carefully because unrealistic initial configurations can lead to exceedingly strong initial forces which influence the reliability of the simulation. Initial configurations of crystalline structures are commonly obtained from the known lattice structures, and liquid systems are generated by using the random number generation method. The initial configurations are then relaxed to minimize internal energy prior to run the MD simulation; the commonly used algorithm for the energy minimization is the conjugate gradient method. Initial velocities are assigned to each atom by sampling from a Gaussian (or Maxwell-Boltzmann) distribution by assuming thermal equilibrium at an initial temperature. The system is subsequently heated because the initial temperature due to the assigned velocities is commonly lower than the desired simulation temperature. As the

simulation reaches the desired temperature, the atoms continuously evolve with time until the system reaches equilibrium. The equilibrium state is when properties such as potential, temperature, and internal energy become stable with respect to time as these properties are monitored in each time step. Once the equilibrium state is reached, we extract atom trajectories or thermodynamic properties from the simulation during the time length of our interest. In general, home-made post-processing programs are used in order to further analyze various properties of interest.

MD is a very powerful tool in the sense that it gives quite accurate numbers compared to experiments once reliable interatomic potentials are given. In some properties which are not sensitive to interatomic potential parameters, MD can provide relatively meaningful results with simple potential functions. In this aspect, MD can afford relatively long and large simulations needed for investigating interfacial behavior which higher level *ab initio* calculations cannot perform due to expensive computational cost. The drawback for MD is that the reliability depends on the interatomic force chosen to reproduce the experimental conditions; the interatomic force usually adopts the simplest models representing the essential physics. In addition, some quantum effects cannot be described by using any form of classical force fields. There are also size and time limitations which are commonly limited to around 10^6 atoms and several hundred nanoseconds, respectively.

3.1.2 Classical Force Fields

The success of classical MD simulations strongly depends on the reliability of the force fields (FFs) used. For ILs, all-atom (AA) and united-atom (UA) FFs have been employed, depending on the type of information sought. The AA model describes all atoms explicitly, whereas the UA model treats a group of atoms as a single ‘united’ atom, such as methyl (CH₃) and methylene (CH₂) groups as single interaction centers. Computationally less expensive UA-FFs permit larger-size and longer-time simulations than AA-FFs, but they are limited in their ability to describe configurations of atoms in detail, particularly in the interfacial region.

In MD calculations, the force exerted on each particle can be evaluated by the first derivative of the potential energy, E ,

$$\mathbf{F}_i = -\frac{\partial E(\mathbf{r}^N)}{\partial \mathbf{r}_i} \quad (3.3)$$

where E is a function of the positions of the particles. In the FF formulation, the total energy (E_{total}) of a given system is expressed as the sum of bonding (E_{bond} , E_{angle} , $E_{torsion}$) and pair-wise nonbonding ($E_{nonbond}$) energies. The nonbonding contribution includes the Coulomb interaction of partial atomic charges and the van der Waals (vdW) interaction in the 12-6 Lennard-Jones (L-J) form.

$$E_{total} = \underbrace{E_{bond} + E_{angle} + E_{dihedral} + E_{improper}}_{E_{bonding}} + \underbrace{E_{vdW} + E_{elec}}_{E_{nonbonding}} \quad (3.4)$$

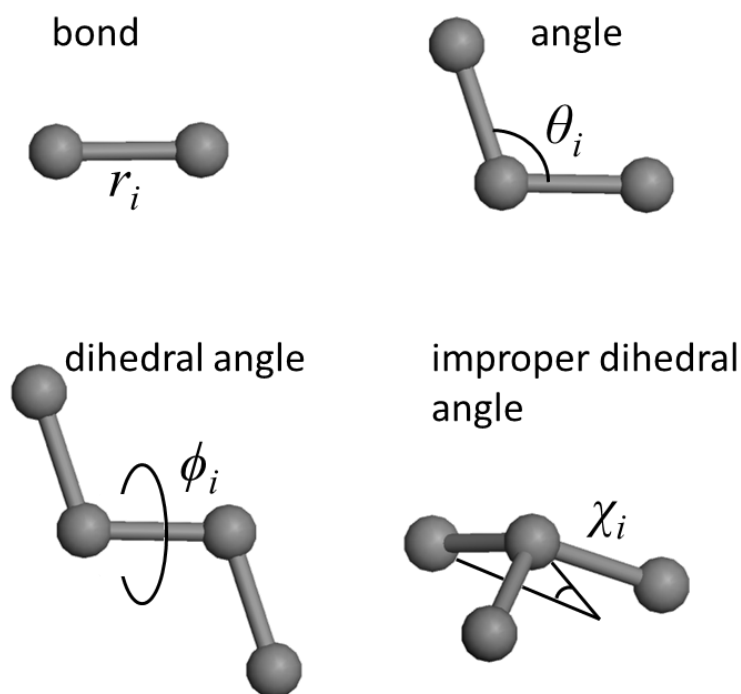


Figure 3.1 Internal coordinates for bonded interactions: r_i describes bond stretching, θ_i represents the angle term, ϕ_i represents the dihedral angle, the χ_i describes out-of-plane improper dihedral angle.

E_{bond} is the energy contribution from two-body interactions of covalently bonded atoms as shown in Fig. 3.1. The simplest form to approximate the bond stretching energy is a harmonic form,

$$E_{bond} = \sum_{bonds} k_{b,ij} (r_{ij} - r_{eq})^2 \quad (3.5)$$

where $k_{b,ij}$ is the force constant of the bond, r_{eq} is the bond length at equilibrium, and r_{ij} is the distance between two bonded atoms ($r_{ij} = |\mathbf{r}_i - \mathbf{r}_j|$). The harmonic approximation allows only small deviations from the equilibrium distance. Another form that is often used to describe more realistic bonds is the Morse potential. All of these FF parameters

for each atom type are typically determined from high-level quantum mechanical calculations combined with experiments. Next, E_{angle} is the energy contribution from three-body angle interactions between two connected bonds. The harmonic approximation is usually used,

$$E_{angle} = \sum_{angles} k_{\theta,ijk} (\theta_{ijk} - \theta_{eq})^2 \quad (3.6)$$

where $k_{\theta,ijk}$ is the force constant, θ_{ijk} is the bend angle for the connected atoms $i - j - k$, and θ_{eq} is the equilibrium angle when the molecule is at rest. The next term is the dihedral angle contribution between four connected atoms $i - j - k - l$; the dihedral angle is defined as the angle between two planes where one contains atoms i, j and k , and the other contains atom j, k and l . So, it is the energy required to rotate a chemical bond as shown in Fig. 3.1. One popular form to describe $E_{dihedral}$ uses a cosine series, which is given by

$$E_{dihedral} = \sum_{dihedrals} k_{\phi,ijkl} \left[1 + \cos(n\phi_{ijkl} - d_n) \right] \quad (3.7)$$

where k_{ijkl} is the dihedral force constant, n is the periodicity parameter (which is 3 in the case of the methyl group), ϕ_{ijkl} is the dihedral angle, and d_n is the phase angle. In order for the covalent bonds to rotate flexibly during simulation, the dihedral force constant is usually an order of magnitude lower than the angle force constant. The above formula is the so-called CHARMM [20] or AMBER [21,22] dihedral style. One other way to describe $E_{dihedral}$ uses the OPLS dihedral form [23,24].

$$E_{dihedral} = \sum_{dihedrals} \left[\frac{k_{1,ijkl}}{2} (1 + \cos \phi_{ijkl}) + \frac{k_{2,ijkl}}{2} (1 - \cos 2\phi_{ijkl}) + \frac{k_{3,ijkl}}{2} (1 + \cos 3\phi_{ijkl}) + \frac{k_{4,ijkl}}{2} (1 - \cos 4\phi_{ijkl}) \right] \quad (3.8)$$

The final term in the intramolecular energy is the $E_{improper}$. The improper angle is the out-of-plane angle at the four atom system (atoms $i - j - k - l$, where j , k and l are all connected to i) between the plane of $i - j - k$ and the plane of $j - k - l$. Thus, the improper energy is the given energy penalty to maintain the planarity of a set of 4 atoms. The improper term is defined in the simulation in the case when sp^2 -hybridized carbon is connected to 3 other atoms such as aromatic rings. A simple harmonic approximation is commonly used to treat the $E_{improper}$.

$$E_{improper} = \sum_{impropers} k_{\chi,ijkl} (\chi_{ijkl} - \chi_{eq})^2 \quad (3.9)$$

where $k_{\chi,ijkl}$ is the improper force constant, χ_{ijkl} is the improper angle, and χ_{eq} is the equilibrium value (typically zero) at rest. The pair-wise nonbonding interactions are composed of the van der Waals (vdW) and electrostatic energies. The vdW energy is usually modeled by the 12-6 Lennard-Jones (LJ) potential,

$$E_{vdW} = \sum_i \sum_{j>i} 4\varepsilon_{ij} \left[\left(\frac{\sigma_{ij}}{r_{ij}} \right)^{12} - \left(\frac{\sigma_{ij}}{r_{ij}} \right)^6 \right] \quad (3.10)$$

where ε_{ij} is the depth of the potential well and σ_{ij} is the distance between atom i and j at the potential minimum. The L-J parameters for unlike atoms were obtained from the Lorentz-Berthelot combination rule, i.e., $\varepsilon_{ij} = \sqrt{\varepsilon_{ij}\varepsilon_{jj}}$ and $\sigma_{ij} = (\sigma_{ii} + \sigma_{jj}) / 2$. The LJ potential is one approximation to describe the vdW energy; the interaction energy sharply

increases towards infinity due to overlap of electron clouds (due to Pauli exclusion principle) when $r_{ij} < \sigma_{ij}$, while the energy becomes attractive due to spontaneously induced dipoles of interacting atoms when $r_{ij} > \sigma_{ij}$. Instead of the 12-6 LJ potential, the 9-6 LJ potential or the Buckingham potential (uses exponential term instead of repulsive 12 term in LJ) is often used to describe the vdW interaction. The Coulomb interaction is employed when electrostatic charges are present.

$$E_{elec} = \sum_i \sum_{j>i} \frac{q_i q_j}{4\pi\epsilon_0 r_{ij}} \quad (3.11)$$

where q_i and q_j are the electrostatic charges of atom i and j , and ϵ_0 is the vacuum permittivity.

The intra- and intermolecular potential energy terms aforementioned here are rather simple and conventional ones. Therefore, each user may choose the appropriate form of the FFs and parameters based on their own systems. For example, if one simulates very large biomolecular system with longer time, a coarse-grained model may be used. The coarse-grained model simplifies the long molecule chain into a few beads, thus limits the number of degrees of freedom. In contrast, when more accurate atomic structures and properties are necessary, MM3 or MM4 FFs can be chosen. These molecular mechanics (MM) FFs involves a lot of parameters with many crossing potentials (*e.g.* stretch-bend) to give higher precision.

3.2 Metropolis Monte Carlo Bond Switching Method

Here, we present a valence force field (VFF)-based Monte Carlo (MC) bond-rotation method capable of identifying stable sp^2 -bonded carbon configurations. The VFF contains four parameters that are adjusted to fit density functional theory (DFT) calculations for both planar and non-planar model structures; the simple VFF model is shown to reliably reproduce the DFT energetics of disordered sp^2 -bonded carbon with various topologies and sizes. The MC bond-rotation method combined with the VFF is demonstrated to be effective in determining minimum-energy sp^2 -bonded carbon structures, such as topological defects and fullerenes with different sizes. The computational approach is also applied to investigate possible configurations of multi-vacancy defects (V_{2n} , $2 \leq n \leq 8$) and their relative stability.

3.2.1 Valence Force Field Model

Within the VFF model, the energetics of sp^2 -bonded carbon structures is evaluated in terms of the increase in energy with respect to the total C-C bond energy corresponding to a single sheet of graphite (referred to as graphene) in the ground state. Here, we adopted a four-parameter VFF model that takes into account the contributions of: (i) two-body bond stretching, (ii) three-body bond bending, (iii) four-body curvature-induced pyramidalization, and (iv) π -orbital misalignment between two adjacent carbon atoms. A more sophisticated VFF model [25] with six parameters has been developed particularly to describe the phonon properties of graphite and nanotubes; however, as demonstrated later the simplified four-parameter model turns out to be sufficient for the

determination of the relative stability of carbon nanostructures that insignificantly deviate in bond topologies from the reference graphene structure.

Given the four-parameter model, we write the energy of sp^2 -bonded carbon as

$$\begin{aligned}
E = & k_r r_0^{-2} \sum_{i,j \in i} (r_{ij} - r_0)^2 + k_\theta \sum_{i,j,k \in i} (\cos \theta_{ijk} - \cos \theta_0)^2 \\
& + k_\phi r_0^{-2} \sum_{i,j < k < l \in i} \left(\frac{3\vec{r}_{ij} \cdot \vec{r}_{ik} \times \vec{r}_{il}}{r_{ij}r_{ik} + r_{ik}r_{il} + r_{il}r_{ij}} \right)^2 + k_\varphi \sum_{i,j \in i} |\vec{\pi}_i \times \vec{\pi}_j|^2
\end{aligned} \tag{3.12}$$

where k_r , k_θ , k_ϕ , and k_φ are adjustable parameters to be determined, the subscripts ij , ik , jl , and ijk represents pairs and triplets involving atoms i , j , k , and l (while j , k , and l are the three neighbors of i), r_{ij} is the interatomic distance between atoms i and j , and θ_{ijk} is the angle between bonds ij and ik . Here, $\vec{r}_{ij} = \vec{r}_i - \vec{r}_j$ where \vec{r}_i is the atomic position vector of atom i , and $\cos \theta_{ijk}$ and π_i are defined as

$$\begin{aligned}
\cos \theta_{ijk} &= \frac{\vec{r}_{ij} \cdot \vec{r}_{ik}}{r_{ij}r_{ik}} \\
\vec{\pi}_i &= 3 \frac{\vec{r}_{ij} \times \vec{r}_{ik} + \vec{r}_{ik} \times \vec{r}_{il} + \vec{r}_{il} \times \vec{r}_{ij}}{r_{ij}r_{ik} + r_{ik}r_{il} + r_{il}r_{ij}}
\end{aligned} \tag{3.13}$$

Note that in the summations double counting of triple interactions is avoided. [25]

3.2.2 Parameter Determination

The four parameters (k_r , k_θ , k_ϕ , k_φ) were adjusted to fit DFT-GGA calculations in the following sequence that corresponds to an increase in the degrees of freedom of each training set: (1) k_r ; (2) k_θ ; and (3) k_ϕ and k_φ ; training sets employed in parameter

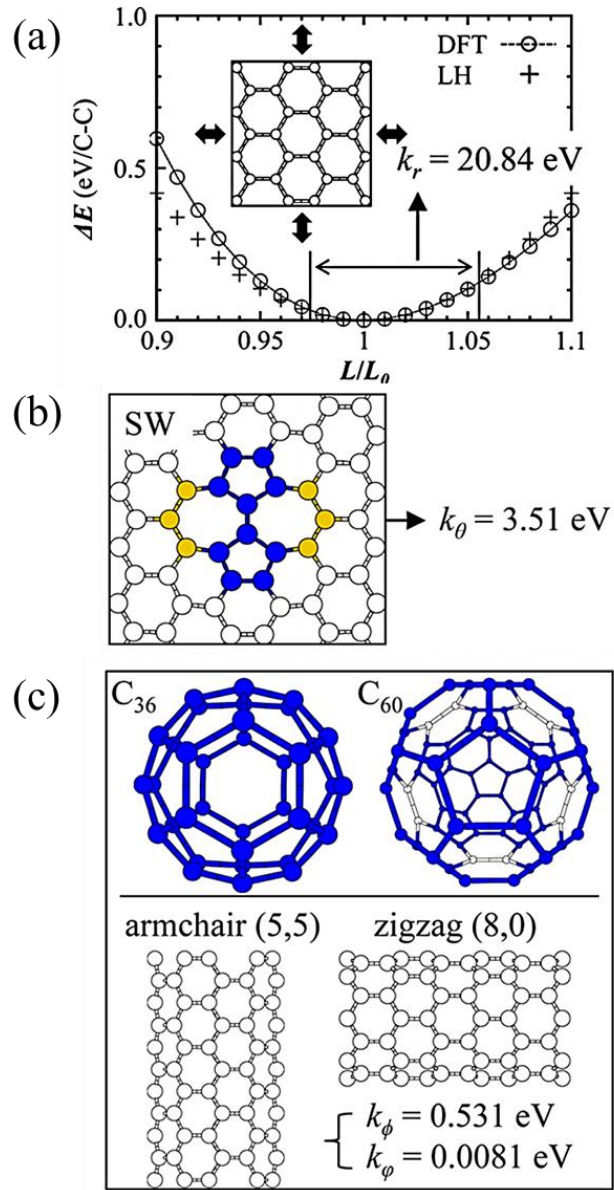


Figure 3.2 Training sets used in parameter optimization: (a) k_r from energy variation (per C-C bond) with respect to lattice constant in graphene; (b) k_θ from Stone-Wales (SW) defect in graphene; and (c) k_ϕ and k_φ from two different sizes of fullerene (C_{36} and C_{60}) and two different nanotube structures [armchair (5,5) and zigzag (8,0)]. Black (blue) filled circles represent atoms comprising 5-membered rings, gray (gold) filled circles are atoms included in 7-membered rings but not in 5-membered rings, and unfilled circles indicate the rest of the lattice atoms.

optimization are illustrated in Fig. 3.2. The best-fit parameters are listed in Table 3.1, which were obtained through minimization of the cross-validation error (ζ) given by $\zeta^2 = 1/N \sum_{n=1}^N (E_{DFT}^{(n)} - E_{VFF}^{(n)})^2$, where $E_{DFT}^{(n)}$ and $E_{VFF}^{(n)}$ refer to the DFT and VFF energies, respectively, of the n th and N total models in the training set; the energies were evaluated based on fully-relaxed structures (with the same network) from each calculation.

For the GGA value of $r_0 = 1.424\text{\AA}$ (and the hexagon interior angle of $\theta_0 = 120^\circ$), k_r was first optimized based on the total energy variation of graphene as a function of lattice constant (-2% to 5%) [see Fig. 3.2 (a)], and then k_θ was adjusted to match the formation energy of a single Stone-Wales (SW) defect that is made by a 90° degree in-plane rotation of a C-C bond about its center [Fig. 3.2 (b)]; the resulting pentagons and heptagons have interior angles varying from 100° to 141° . For the DFT calculations, we used a 4-atom supercell for the lattice constant variation and a 288-atom (6×12 unit cells) supercell for the SW defect formation energy; the respective Brillouin-zone (BZ) integrations were performed using $8 \times 12 \times 1$ and $2 \times 2 \times 1$ (Monkhorst-Pack) k -point meshes.

Next, we determined k_ϕ and k_φ simultaneously using two different sizes of fullerene (C_{36} and C_{60}) and two different nanotube structures [armchair (5, 5) and zigzag (8, 0)] [Fig. 3.2 (c)]. The strain in nonplanar conjugated carbon structures arises from pyramidalization and π -orbital misalignment [26]. Very little π -orbital misalignment, if any, exists in fullerene structures; for instance, the π -orbitals of C_{60} are perfectly aligned [27]. Hence, the strain in fullerenes is predominantly caused by pyramidalization [27]. On the other hand, in the case of nanotubes π -orbital misalignment tends to be the main

source of strain with a minor contribution of pyramidalization; for instance, the armchair (5, 5) structure consists of two types of C-C bonds with π -orbital misalignment angles of either $\varphi = 0^\circ$ or 21.3° , while the pyramidalization angle of its sidewall is only $\phi \approx 6.0^\circ$ [28]. For the fullerene calculations, we employed a cubic periodic supercell of 20 Å sides (which is sufficiently large to avoid unphysical interactions with the periodic images. The periodic supercells for the armchair and zigzag nanotubes include 10 unit cells (corresponding to 2.47 nm long according to the DFT-GGA) and 6 unit cells (2.56 nm long) along the tube axis, respectively; the lateral separation between the (periodic image) tube centers is about 20 Å. Γ -point BZ sampling was used for the DFT calculations of both fullerenes and nanotubes.

Table 3.1 Parameters of the valence force field model employed in this work, which were adjusted to fit DFT-GGA calculations. Units are given in eV.

| k_r | k_θ | k_ϕ | k_φ |
|-------|------------|----------|-------------|
| 20.84 | 3.51 | 0.531 | 0.0081 |

3.2.3 Metropolis Monte Carlo Simulation

For a defective system, its atomic structure is allowed to evolve toward thermodynamic equilibrium through MC bond-rotation moves, as depicted in Fig. 3.3. Similar to the Wooten-Winer-Weaire (WWW) bond transposition scheme [29], a bond-rotation move involves the breaking of new bonds (A-C and B-D). In a perfect hexagonal lattice, such bond-rotation leads to SW defect formation (where four adjacent hexagons

are transformed into two pentagons and two heptagons). The acceptance or rejection of each bond switching move is determined using probability

$$P = \min[1, \exp(-\Delta E / k_B T)] \quad (3.14)$$

where ΔE is the energy difference between the old and the trial configuration; the old and trial structures were fully relaxed by the Polak and Ribiere's conjugate gradient method [30]. Successive MC bond - rotation moves enable one to search all possible configurations of a sp^2 -bonded carbon system, regardless of kinetic barriers associated.

According to earlier theoretical calculations [31,32], the barriers for C-C bond rotations are in the range of 4–10 eV, depending on the local atomic configuration. Given the large barriers, thermally-activated bond rotation appears to be infrequent under typical annealing conditions (< 1000 °C); however, the structural interconversion via the bond rotation mechanism is likely facilitated by moderate-energy electron irradiation. Very recently Kotakoski *et al.*[33] provided evidence that irradiation-induced topological defects can gradually undergo transformation into more stable configurations through successive bond rotations under continued electron-beam exposure (in which electron energies were just above the threshold for atom displacement). As demonstrated later our MC bond-rotation scheme combined with the four-parameter VFF model well describes the structural relaxation process and effectively determines the minimum-energy configurations of disordered (sp^2 -bonded) carbon nanostructures of various dimensions.

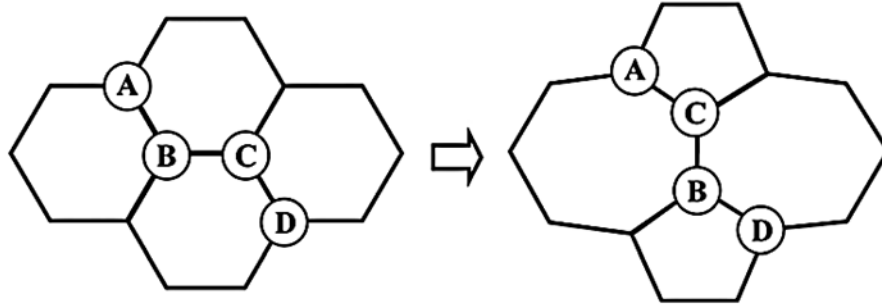


Figure 3.3 Illustration of a MC bond-rotation move that involves the 90° rotation of a single bond (B-C) by breaking two bonds (A-B and C-D) and forming two new bonds (A-C and B-D); this bond rotation yields a Stone-Wales (SW) defect (right).

3.3 First Principles Quantum Mechanics

Quantum mechanical calculations are based on obtaining the quantum mechanical wave function by solving the Schrödinger equation.

$$\hat{H}\psi = E\psi \quad (3.15)$$

The Hamiltonian (\hat{H}) is given by

$$\hat{H} = \sum_{\alpha} -\frac{\hbar^2}{2M_{\alpha}} \nabla_{\alpha}^2 + \sum_i -\frac{\hbar^2}{2m_e} \nabla_i^2 + \frac{1}{2} \sum_{i \neq j} \frac{e^2}{|\vec{r}_i - \vec{r}_j|} + \frac{1}{2} \sum_{\alpha \neq \beta} \frac{Z_{\alpha} Z_{\beta} e^2}{|\vec{R}_{\alpha} - \vec{R}_{\beta}|} + \sum_{i, \alpha} -\frac{Z_{\alpha} e^2}{|\vec{r}_i - \vec{R}_{\alpha}|} \quad (3.16)$$

where the first two terms are the kinetic energies of the electrons and nuclei, the remaining three terms are the potential energies of the electron-electron, nuclei-nuclei, and electron-nuclei interactions. Fundamentally, the Schrödinger equation can be solved analytically for a single electron system (e.g. a hydrogen atom), but can only be solved

numerically for poly-electronic systems. Therefore, we use several approximations to numerically solve the corresponding equations. The Born-Oppenheimer approximation decouples the electronic and ionic structure calculations since the electrons are much faster than the heavier ions. That is, electronic equations are solved first assuming ions are fixed, then the ions are subsequently evolved as classical particles assuming the electrons are fixed. The electronic system is described by the Hamiltonian,

$$\hat{H} = \sum_i -\frac{\hbar^2}{2m_e} \nabla_i^2 + \frac{1}{2} \sum_{i \neq j} \frac{e^2}{|\vec{r}_i - \vec{r}_j|} + \sum_i V_{ext}(\vec{r}_i) \quad (3.17)$$

which is given by the sum of the kinetic energy of electrons, interaction of electrons with each other, and interaction of electrons with the external potential from the ions.

3.3.1 Density Functional Theory

Density functional theory (DFT) is one approach for the calculation of the electronic structure. DFT is based on the Hohenberg-Kohn theorem [34] that all properties of the system are a functional of the ground state electron density $\rho(r)$. In the Kohn and Sham approach [35], the many-body problem in the interacting electron system is replaced by that of non-interacting electrons in an effective potential. The Kohn-Sham one electron operator then can be given by the set of equations; in the non-interacting electron system, the difference with the interacting electron system is represented by the term called the exchange-correlation energy $E_{xc}[\rho(r)]$. Though we can obtain the electronic structure of the many-body system by solving the Kohn-Sham equations for non-interacting electrons, the exact form of the $E_{xc}[\rho(r)]$ is not known, except for a free

electron gas. Therefore, a reasonable approximation of $E_{xc}[\rho(r)]$ is essential to obtain accurate results. The simplest[or one simple] approximation is the local density approximation (LDA); this method treats the $E_{xc}[\rho(r)]$ as dependent only on the density at each point, the same as in a homogeneous electron gas. Another approach is the generalized-gradient approximation (GGA) in which $E_{xc}[\rho(r)]$ takes the density and its gradient into account.

3.3.2 Grimme's DFT-D2 method

In order to include the vdW interaction which is not taken into account in current DFT functionals, a pragmatic approach has been given by the DFT-D method [36]. The total energy becomes $E_{\text{DFT-D}} = E_{\text{KS-DFT}} + E_{\text{disp}}$, where the semi-empirical dispersion correction term (E_{disp}) is added to the conventional Kohn-Sham DFT energy ($E_{\text{KS-DFT}}$). In the Grimme's DFT-D2 method [171], E_{disp} is described as the attractive pair-wise force field with parameters that are optimized with respect to popular functionals. E_{disp} is given by

$$E_{\text{disp}} = -\frac{s_6}{2} \sum_i \sum_j \frac{C_6^{ij}}{r_{ij}^6} f_{\text{damp}}(r_{ij}) \quad (3.18)$$

where C_6^{ij} is a dispersion coefficient for the atom pair i and j and s_6 is a global scaling factor. The global scaling parameter (s_6) depends on the functional, such that $s_6=0.75$ for PBE, 1.2 for BLYP and 1.05 for B3LYP functionals. The damping function (f_{damp}) is used to avoid near-singularities for small distance, and given by

$$f_{damp}(r^{ij}) = 1 / \left[1 + e^{-d(r^{ij}/R_0^{ij}-1)} \right] \quad (3.19)$$

where d is the damping parameter and R_0^{ij} is the sum of atomic vdW radii.

Chapter 4: Microstructure of Ionic Liquid/Graphene Interfaces

4.1 Introduction

Ionic liquids (ILs) are a relatively new class of materials with many unique and useful properties. They exist in the liquid state at room temperature, and exhibit high thermal and chemical stability, extremely low volatility, non-flammability, and wide electrochemical windows. [37,38] The IL's properties are highly tunable through the choice of the cation and anion pair. [39] Over recent years, room temperature ILs have received considerable research attention due to their broad range of potential applications.[40] In particular, the ionic nature of ILs makes them an excellent choice for “solvent-free” electrolytes in electrochemical double layer capacitors (EDLCs) or supercapacitors.[7,41]

The performance of EDLCs is largely determined by the microstructure and capacitance of the electrical double layers (EDLs) at the interface between ILs and electrodes. Hence, recently the structure and behavior of ILs in the vicinity of electrified surfaces have been studied using a variety of experimental and theoretical techniques.[42-46] The IL ions are found to be alternatively stacked near a charged electrode, due to strong electrode-ion and ion-ion electrostatic interactions;[9,43,45] the distinct alternative layering can be possible by the fact that solvent-free dense ILs typically have a small Debye length on the order of ion size.[47] Although the layered structure tends to extend up to a few nanometers, several previous studies[42] suggest that the EDL potential

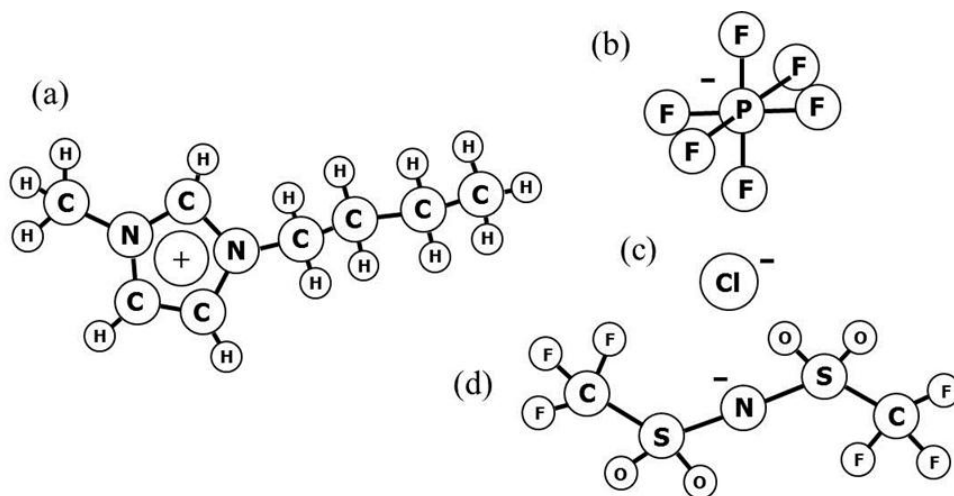


Figure 4.1 Schematic of the ionic liquids used in this simulation. (a) BMIM^+ (1-butyl-3-methylimidazolium), (b) PF_6^- (hexafluorophosphate), (c) Cl^- , (d) TFSI^- (bis-trifluoromethylsulfonyl-imide)

drop mainly occurs within the first layer of counterions (which is typically 3-5 Å thick). The interfacial behavior is hardly explained by the standard Gouy-Chapman-Stern (GCS) model [48] of dilute aqueous electrolytes in which the EDL is typically composed of a compact inner layer and a diffuse outer layer.

In this work, we examine the microstructure of graphene in IL 1-butyl-3-methylimidazolium hexafluorophosphate ($[\text{BMIM}][\text{PF}_6]$), 1-butyl-3-methylimidazolium bis(trifluoromethylsulfonyl) imide ($[\text{BMIM}][\text{TFSI}]$), 1-butyl-3-methylimidazolium chloride ($[\text{BMIM}][\text{Cl}]$) using a classical molecular dynamics (MD). First, we investigate the microstructure of $[\text{BMIM}][\text{PF}_6]$ near the graphene electrode by varying the electrode surface charge using MD simulations to provide a molecular description of EDLs, including $[\text{BMIM}][\text{PF}_6]$ packing and orientation, cation-anion segregation, and electrode charge screening.

4.2 Computational Methods

In this work, we employed AA-FFs in the frame of OPLS-AA [49,50] (Optimized Potential for Liquid Simulations/All Atom), as an explicit description of the electrolyte-electrode interface is necessary. We used the FF parameters for [BMIM][PF₆] from Pádua *et al.*,[51,52] while allowing PF₆ to be fully flexible based on the geometrical parameters from Borodin *et al.*[53] The L-J parameters of graphene are from Battezzati *et al.*[54] To confirm the validity of the FFs, we calculated the bulk density of [BMIM][PF₆] for 500 ion pairs in a cubic box; the predicted density is 1.33 g/cm³ at P = 1 atm and T = 300 K, which is in good agreement with previous experiments[55] (1.36 g/cm³) and calculations[56,57] (1.32-1.35 g/cm³).

Figure 4.2 shows a schematic of the simulation system which consists of [BMIM][PF₆] ion pairs bounded between two graphene electrodes. The lateral size of the graphene sheets is $34.18 \times 34.53 \text{ \AA}^2$, corresponding to 448 C atoms. The distance between the electrodes (d_{Gr-Gr}) was chosen large enough such that the bulk properties of [BMIM][PF₆] IL were reached in the middle region of the system for various electrode excess charge densities (σ); it turns out that $d_{Gr-Gr} = 70 \text{ \AA}$ is sufficient when $\sigma \leq 7 \text{ \mu C/cm}^2$, while $d_{Gr-Gr} = 100 \text{ \AA}$ at $\sigma \geq 8 \text{ \mu C/cm}^2$.

Initially, 213 [BMIM][PF₆] pairs for $d_{Gr-Gr} = 70 \text{ \AA}$ (346 pairs for $d_{Gr-Gr} = 100 \text{ \AA}$) were randomly placed in a three-dimensional (3D) domain with dimensions of $37.6 \times 38 \times 64 \text{ \AA}^3$; periodic boundary conditions were imposed in the x and y directions. The x and y dimensions were slowly decreased to the target value of $34.18 \times 34.53 \text{ \AA}^2$ (which is equal to the lateral size of graphene) over 500 ps. Then, the graphene electrodes were

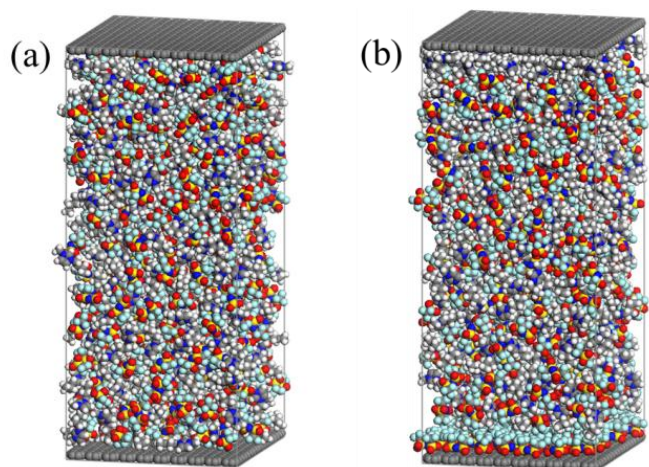


Figure 4.2 Schematic the simulation box. Planar graphene sheets are placed at the two ends of the simulation domain. Periodic boundary conditions are applied in the x and y directions. (a) and (b) represent snapshots when (a) uncharged graphene electrode (b) charged graphene electrode are used.

inserted at 3 \AA above and below the $[\text{BMIM}][\text{PF}_6]$ IL domain. All MD simulations reported herein employed the velocity Verlet algorithm[58] to integrate Newton's equation of motion with a time step of 1 fs.

We first ran MD at 1000 K for 1.2 ns, followed by 3 ns at 300 K to equilibrate the system. Production runs were carried out for 4 ns with atomic positions recorded every 4 ps. All runs were in the NVT ensemble with the temperature controlled by a Nose-Hoover thermostat[59] with a 100 fs damping parameter. Graphene sheets were kept rigid, and the C-H bonds in BMIM were constrained using the Shake algorithm.[60] We used spherical cutoff radii of 12 \AA and 16 \AA for the vdW and Coulomb interactions, respectively. Electrostatic interactions beyond the cutoff radius of 16 \AA were calculated using a particle-particle particle-mesh (PPPM) scheme[61] in reciprocal space; the inter-

slab interactions in the z direction were removed by inserting a large vacuum space between the graphene sheets.[62] All MD simulations were performed with the Large-scale Atomic/Molecular Massively Parallel Simulator (LAMMPS) program.[63] All MD results reported herein were obtained from the average of five independent simulations with different initial atomic configurations.

4.3. Molecular Distribution of [BMIM][PF₆] Ionic Liquid

4.3.1 Near Uncharged Graphene Electrodes

Figure 4.3 shows the mass density profiles of BMIM and PF₆ (with a bin size of 0.1 Å) along the direction normal to the graphene surface. The profiles exhibit noticeable oscillations which dampen away from the electrode; the layering behavior is found to extend about 25-30 Å, after which the IL structure becomes nearly bulk-like. The first layer that starts around 2.6 Å from the electrode has an average density of 1.59 g/cm³ which is about 20% greater than the bulk density of 1.33 g/cm³. The average densities of the second and third layers are predicted to be 1.33 g/cm³ and 1.29 g/cm³, respectively, while their respective peak densities are 1.5 and 1.1 times larger than the bulk density, respectively.

The oscillations are indicative of layered IL structure formation at the interface, as also suggested by previous studies.[56,57,64,82] This is apparently attributed to the vdW force that draws IL ions close to the graphene surface, leading to the formation of the first IL layer where BMIM and PF₆ are packed together to maximize the IL-graphene vdW interaction. A detailed analysis of the atomic arrangement of BMIM and PF₆ will follow.

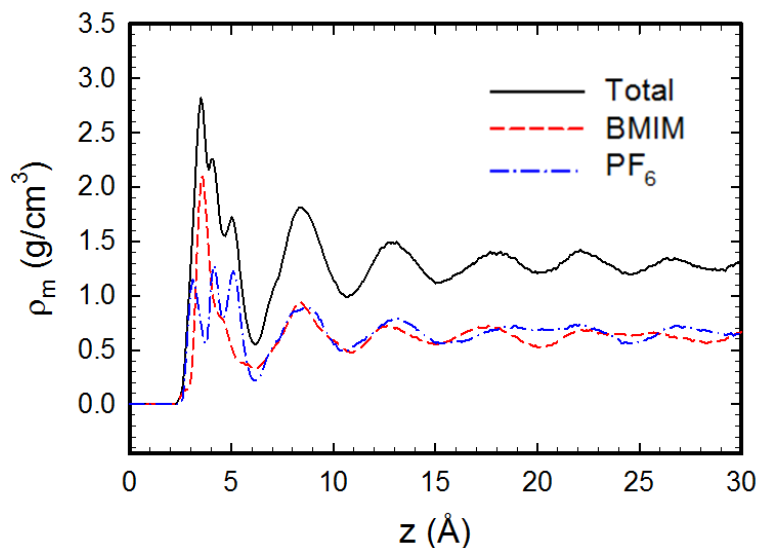


Figure 4.3 Total, BMIM, and PF_6 mass density (ρ_m) profiles along the z -axis near an uncharged graphene electrode which is located at $z = 0$.

According to our calculations, the predicted vdW energy of 11 kcal/mol for the BMIM-graphene interaction tends to be substantially larger than 5 kcal/mol for the PF_6 -graphene interaction; however, in the first layer BMIM and PF_6 are maintained at the same number density ($\sim 5.6 \times 10^{-3} \text{ \AA}^{-3}$) to satisfy the condition of charge neutrality. It is also worth noting that the strength of vdW energies is an order of magnitude greater than the thermal energy at room temperature ($kT \approx 0.59$ kcal/mol); hence, the first-layer ions are expected to have a rather rigid, or solid-like, structure due to suppression of their thermal fluctuations. In comparison, at an IL/vacuum interface, ions may also rearrange to reduce the surface free energy, but only a marginal increase in the surface layer number density without distinct layering is observed.[65,66]

4.3.2 Near Charged Graphene Electrodes

To emulate the charged electrodes, we assigned excess positive (negative) charge equally to the C atoms in graphene located at $z = 0 \text{ \AA}$ ($z = 70$ or 100 \AA); here, the excess charge density was varied from $\sigma = \pm 1$ to $\pm 60 \text{ \mu C/cm}^2$ (specific values for σ are indicated by the circles in Fig. 5.2). A charged electrode creates an electric field, which causes the rearrangement of IL ions near the electrode to screen the electric field. Figure 4.4 shows how the electrode charging influences the distribution of BMIM and PF₆; as the electrode is increasingly charged, the segregation between BMIM and PF₆ accordingly increases. When the electrode is positively charged [Fig. 4.4 (a)-(c)], anionic PF₆ is attracted while cationic BMIM is repelled. At $\sigma = +10 \text{ \mu C/cm}^2$ [(a)], BMIM still remains partially mixed with the PF₆ first layer. However, at $\sigma = +40 \text{ \mu C/cm}^2$ [(c)], BMIM is clearly segregated from the PF₆ layer. Similarly, PF₆ forms a second layer with some mixing in the BMIM first layer when $\sigma = -10 \text{ \mu C/cm}^2$ [(d)]. When $\sigma = -40 \text{ \mu C/cm}^2$ [(f)], PF₆ has a more distinct layer with a smaller degree of mixing. More quantitative analysis of the degree of mixing will be discussed later.

The alternative layering of PF₆ and BMIM is apparently due to the electrostatic interaction between them. For instance, BMIM cations, which accumulate near the negative electrode, attract PF₆ anions; this process repeats to form multi-stacked alternately charged layers. As illustrated in Fig. 4.4, the distinct multi-layering is found to extend about 3 nm from a charged electrode, while the thickness of each alternating [BMIM][PF₆] layer tends to be 7-9 \AA ; overall, the results are consistent with previous experimental observations of the ordering of ILs in the vicinity of various charged

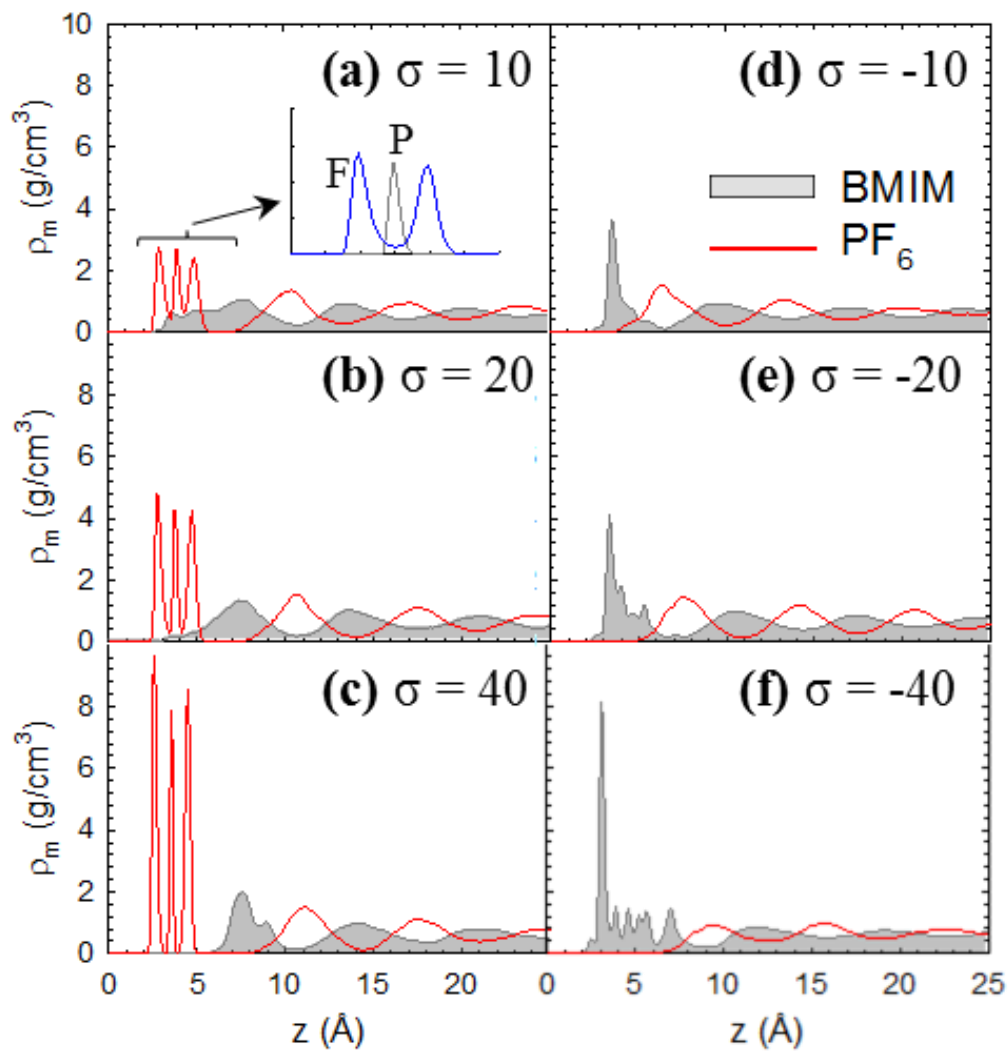


Figure 4.4 BMIM and PF_6 mass density (ρ_m) profiles along the z -axis near charged graphene electrodes with different excess charge densities (σ) as specified (in $\mu\text{C}/\text{cm}^2$). Each electrode is located at $z = 0$. The inset in (a) shows the distributions of F and P atoms

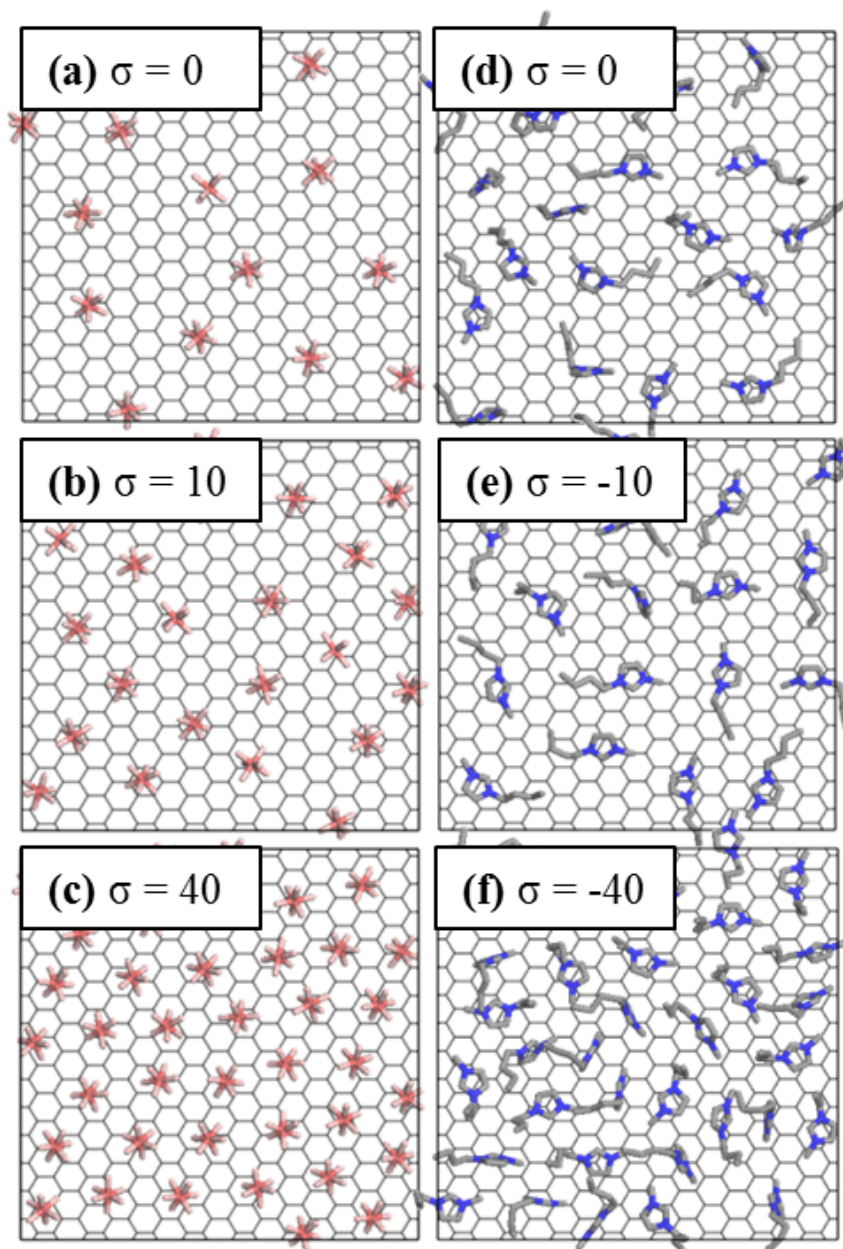


Figure 4.5 Snapshots of counterions in the layer closest to charged electrodes with different excess charge densities as specified (in $\mu\text{C}/\text{cm}^2$); (a)-(c) PF_6 , (d)-(f) BMIM. Thin gray lines depict the graphene lattice, and red/pink clusters (left panels) and gray/blue sticks (right panels) represent PF_6 and BMIM, respectively.

surfaces.[43,67,68]

For the same amount of electrode charge $|\sigma|$, as shown in Fig. 4.4, the PF_6 density near the positive electrode is consistently greater than the BMIM density near the negative electrode. At $|\sigma| = 10 \mu\text{C}/\text{cm}^2$, the first-layer PF_6 density ($= 1.45 \text{ g}/\text{cm}^3$) is 113% greater than the bulk PF_6 density ($= 0.68 \text{ g}/\text{cm}^3$), whereas the first-layer BMIM density ($= 0.87 \text{ g}/\text{cm}^3$) is only 34% greater than the bulk BMIM density ($= 0.65 \text{ g}/\text{cm}^3$). At $|\sigma| = 40 \mu\text{C}/\text{cm}^2$, the first-layer densities of PF_6 and BMIM are 312% and 116% greater than their respective bulk densities.

Figure 4.5 depicts the arrangement of counterions in the first layer for various σ . The snapshots clearly demonstrate that PF_6 accumulates more densely than BMIM, which is due to their steric differences. The smaller size of PF_6 allows them to pack more tightly than BMIM; moreover, PF_6 can pack into a well-ordered lattice-like structure due to its highly symmetric compact configuration, unlike BMIM with a rather complex geometry.

The rearrangement of ions in response to the excess electrode charge causes the interfacial space charge density to deviate from the neutral case. Figure 4.6 shows the space charge density profiles attributed to the respective ion species along the direction normal to the electrode with varying σ , as calculated from the number densities and partial charges of each atom; each profile features fluctuations near the electrodes which gradually dampen until nearly flat in the bulk region. Near the positive electrodes [(a)-(c)], the negative (positive) sharp peaks correspond to planarly-aligned negatively-charged F (positively-charged P) atoms in PF_6 . The comparatively broadened

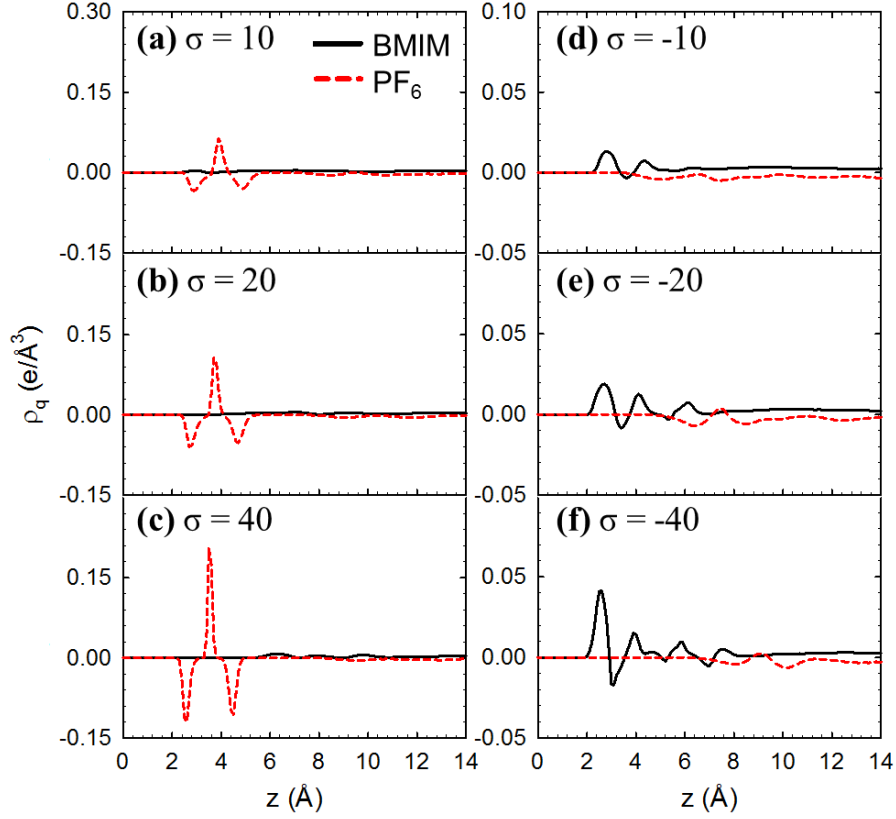


Figure 4.6 Space charge density (ρ_q) profiles due to BMIM and PF_6 along the z -axis near charged electrodes with different excess charge densities as specified (in $\mu\text{C}/\text{cm}^2$). Each electrode is located at $z = 0$.

fluctuations near the negative electrodes [(d)-(f)] reflect the relatively even partial charge distribution over the atoms in the BMIM ring, as detailed later. Overall the positive/negative charge densities are proportional to the number densities of [BMIM][PF_6] molecules, as the charges on PF_6 and BMIM are equal in magnitude (± 1).

4.3.3 Electrode Charge Screening and Cation-Anion Segregation

Table 4.2 summarizes[69] the net charge (q_{net}) densities of the first layers for various σ , together with corresponding positive (q_+) and negative (q_-) charge densities. We assessed how well the first layer of ions (counterion-rich) screens the electrode charge using a screening parameter $\beta = -q_{net}/\sigma$; that is, if $\beta > 1$ the electrode charge is overscreened. According to this analysis, both positive and negative electrodes tend to be overshielded by the first-layer ions unless σ is fairly large ($> 50 \mu\text{C}/\text{cm}^2$).

For a given $|\sigma|$, the PF_6 -rich layer is found to overscreen more than the BMIM-rich layer; note that the β values are 1.84 and 1.29, respectively, at $\sigma = +10$ and $-10 \mu\text{C}/\text{cm}^2$. This is related to the packing efficiency difference between PF_6 and BMIM, i.e., smaller PF_6 ions are crowded into the first layer more effectively than larger BMIM ions, as also indicated by the mass density profiles [Fig. 4.4].

Table 4.1 Predicted peak and average densities of counterions in the first IL layer from electrodes with different charge densities.

| σ [$\mu\text{C}/\text{cm}^2$] | ρ_{\max} [g/cm^3] | ρ_{avg} [g/cm^3] |
|--|--|--|
| 10 | 2.75 | 1.45 |
| 20 | 4.78 | 1.90 |
| 40 | 9.68 | 2.80 |
| -10 | 3.70 | 0.87 |
| -20 | 4.09 | 0.99 |
| -40 | 8.12 | 1.69 |

Table 4.2 Charge densities ($q_{net} = q_- + q_+$), screening parameter (β), and counterion mixing parameter (χ) in the first counterion layer from electrodes with different charge densities.

| Σ ($\mu\text{C}/\text{cm}^2$) | q_{net} ($\mu\text{C}/\text{cm}^2$) | q_- ($\mu\text{C}/\text{cm}^2$) | q_+ ($\mu\text{C}/\text{cm}^2$) | β | χ |
|---|--|--|--|---------|--------|
| 10 | -18.4 | -26.9 | 8.5 | 1.84 | 0.68 |
| 20 | -32.0 | -37.5 | 5.5 | 1.60 | 0.85 |
| 40 | -53.9 | -53.9 | 0.0 | 1.35 | 1.00 |
| 100 | -85.3 | -85.3 | 0.0 | 0.85 | 1.00 |
| -10 | 12.9 | -7.1 | 20.0 | 1.29 | 0.65 |
| -20 | 25.1 | -0.5 | 25.6 | 1.25 | 0.98 |
| -40 | 44.6 | -0.4 | 45.0 | 1.11 | 0.99 |
| -100 | 67.2 | 0.0 | 67.2 | 0.67 | 1.00 |

As $|\sigma|$ increases, the packing density of counterions in the first layer approaches an asymptote defined by steric limitations. Once this limit is reached ($\sigma > 50 \mu\text{C}/\text{cm}^2$), additional counterions form a second layer. Hence, β decreases as $|\sigma|$ increases until both the PF_6 and BMIM layer have $\beta < 1$, i.e. the electrode is underscreened by the first layer. At this limit, PF_6 is found to have a greater packing density than BMIM, as β for the PF_6 layer is greater than that of the BMIM layer.

We also estimated the degree of [BMIM][PF_6] segregation in the first layer by defining a counterion mixing parameter, $\chi = q_{+/-}/(q_{+/-} + q_{-/+})$; that is, χ is the ratio of counterions to total number of ions ($\chi = 1$ if BMIM and PF_6 are completely separated). As summarized in Table 4.2, PF_6 and BMIM tend to mix together at small σ but segregate at large σ . When $\sigma = \pm 10 \mu\text{C}/\text{cm}^2$, the first layers at both electrodes have

around 65-68 % counterions. As σ increases, however, χ increases until the first layer is 100 % counterions, as predicted by the mass density profiles [Fig. 4.4]. This is apparently attributed to the strong electrostatic attraction (repulsion) of the counterion (coion) with the electrode. Interestingly, χ approaches unity more rapidly for BMIM than PF₆; it turns out that BMIM tends to reorient and sterically prevent PF₆ from mixing with BMIM, as discussed in more detail later.

4.4 Molecular Orientation of [BMIM][PF₆] Ionic Liquid

4.4.1 Near Uncharged Graphene Electrodes

As illustrated in the inset of Fig. 4.4 (a), PF₆ arranges to form two planes (each of which is made of three F atoms) parallel to the flat electrode. In this orientation, the three F atoms maximize their vdW interactions with graphene, making this the preferred orientation. The density profile of PF₆ shows a single peak at the second and third layers, indicating that the preferred orientation no longer exists. The first layer of BMIM exhibits a single distinct peak, implying its tendency to lie parallel to the electrode.

The BMIM orientation in the first layer was analyzed in more detail using an order parameter, $P_2(\cos\theta) = \langle (3\cos^2\theta - 1)/2 \rangle$; the results are shown in Fig. 4.7. Here, θ is the angle of the orientation of the ring plane (or butyl chain) with respect to the electrode surface normal. The order parameter (which ranges from -0.5 to 1.0) provides important information about orientation preferences; for instance, $P_2(\cos\theta) = 1$ at $\theta = 0^\circ$, $P_2(\cos\theta) = -0.5$ at $\theta = 90^\circ$, and $P_2(\cos\theta) \approx 0$ if there is no preferred orientation. In the

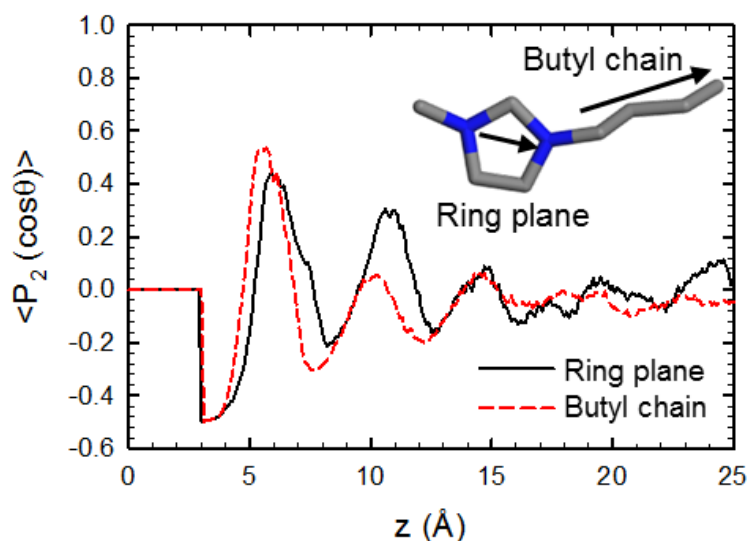


Figure 4.7 Order parameter $\langle P_2(\cos\theta) \rangle$ profiles for BMIM along the z -axis for the angles of the ring plane and butyl chain with respect to the graphene surface normal

first layer, the peak value for the ring plane is -0.5, indicating that the electrode and the imidazole ring of BMIM are parallel. In addition, the value of about -0.5 for the butyl chain implies that it is parallel as well. This is not surprising since the parallel orientation leads to the maximum vdW interaction between BMIM and graphene. At the transition ($z \approx 6 \text{ \AA}$) from the first to second layer, the ring plane value rises and shows a maximum of about 0.45; this implies that the ring plane tends to lie tilted to the electrode surface. In the second layer ($z \approx 8 \text{ \AA}$), the decreased ring plane value (≈ -0.2) indicates that the imidazole ring still has a small tendency to lie flat; however, after the third layer, the orientation preference disappears. Our results are in good agreement with previous theoretical [82,56,57,64,70] and experimental[71] studies.

4.4.2 Near Charged Graphene Electrodes

As expected, the orientation of PF_6 near the positive electrode is found to be analogous to the uncharged electrode case; the additional electrostatic attraction with negatively charged F atoms causes the three PF_6 peaks to become more pronounced, as also seen in the corresponding mass density profiles [Fig. 4.4]. On the other hand, near the negative electrode, PF_6 shows only one broad peak, indicating that PF_6 loses its preferred orientation.

The ring orientation of BMIM in the first layer may vary between 0° and 90° . Figure 4.8 shows the distributions of the BMIM ring orientations[72] when $\sigma = 0$ and $\pm 10 \mu\text{C}/\text{cm}^2$. For $\sigma = 0 \mu\text{C}/\text{cm}^2$, the maximum probability occurs around 10° . The distribution becomes narrower (broader) with the maximum probability around 5° ($25\text{-}40^\circ$) when the electrode is negatively (positively) charged. This suggests that the additional electrostatic attraction enhances the tendency of the BMIM ring to lie parallel to the negative electrode, which has also been observed experimentally;[73,74] recall that the BMIM ring is positively charged. Conversely, the electrostatic repulsion causes the BMIM ring to tilt away from the electrode. We also examined the ring orientation distribution for $\sigma = -40 \mu\text{C}/\text{cm}^2$ in Fig. 4.9. In the highly charged case, as shown in the inset of Fig. 4.9, the BMIM ring distribution exhibits two distinct features – a sharp peak [indicated by (a)] followed by a broad peak [(b)]; it seems that BMIM has two types of ring orientations, as seen in Fig. 4.9. In the (a) layer (closest to the electrode), rings have the expected preference to lie parallel to the electrode, with around 85% of rings less than

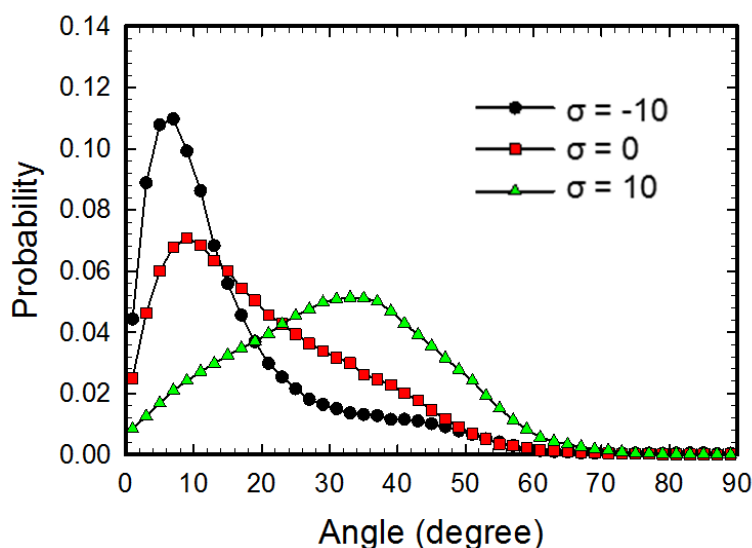


Figure 4.8 Probability distributions for the BMIM ring normal angle with respect to the graphene surface normal in the first IL layer at varying electrode charge as specified (in $\mu\text{C}/\text{cm}^2$)

10° . The rings in the (b) layer, however, exhibit a relatively level distribution which suggests that the rings are tilted with no preferred orientation.

Figure 4.10 presents the number density profiles of C atoms (C1-C4) in the butyl chain, which can describe the chain orientation. The insets of Fig. 4.10 also illustrate how the orientations of PF_6 and BMIM change as the electrode charge varies from 0 to $\pm 40 \mu\text{C}/\text{cm}^2$. When $\sigma = -10 \mu\text{C}/\text{cm}^2$, all four C atoms have overlapping peaks [(b)], indicating that the butyl chain is parallel to the electrode. However, when $\sigma = -40 \mu\text{C}/\text{cm}^2$, the chain is bent into a perpendicular orientation, as indicated by the segregated peaks in Fig. 4.10 (a). As a result, additional BMIM rings can pack in parallel into layer (a). However, rings in layer (b) cannot pack in parallel as a result of the steric interference from the butyl chain.

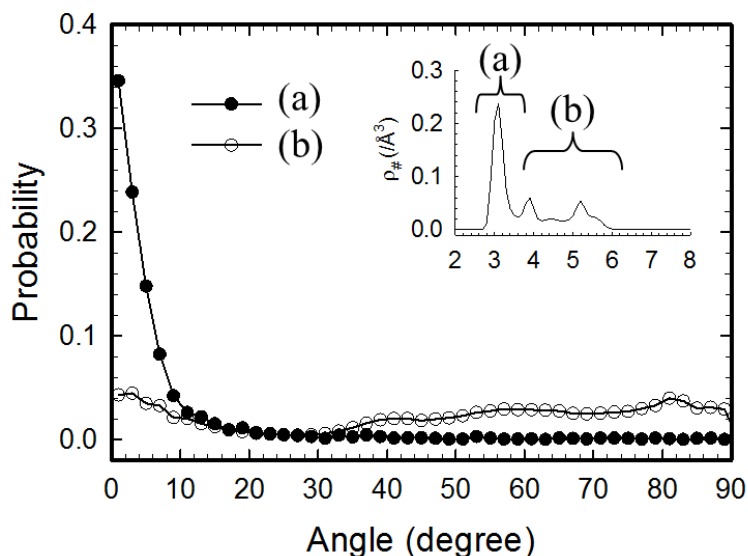


Figure 4.9 Probability distribution for the BMIM ring normal angle with respect to the graphene surface normal in the BMIM layer adjacent to a negatively charged graphene at $\sigma = -40 \mu\text{C}/\text{cm}^2$. The inset shows the corresponding number density profile of the BMIM ring atoms, suggesting that BMIM forms two sub-layers as indicated by (a) and (b).

Instead, the rings tend to pack tilted to the electrode as this is the most energetically favorable configuration. When $\sigma = 10 \mu\text{C}/\text{cm}^2$, the C4 peak remains close to the electrode while the other peaks shift away. As the BMIM ring is repelled from the electrode, the butyl chain rotates away from the electrode; C4, however, apparently remains anchored near the electrode due to its vdW interaction with the electrode. When $\sigma = 40 \mu\text{C}/\text{cm}^2$, all four peaks have shifted away, indicating that the butyl chain is no longer anchored; that space is instead occupied by PF_6 .

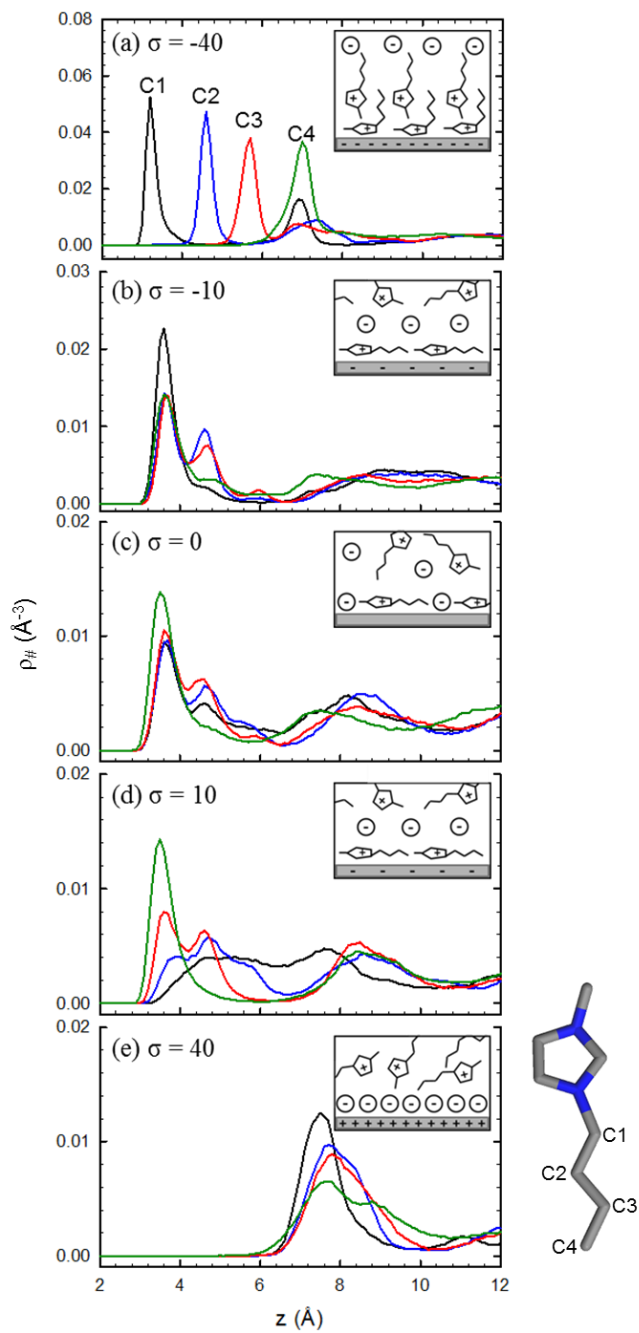


Figure 4.10 Number density ($\rho_{\#}$) profiles of butyl chain atoms (C1-C4) along the z -axis near graphene electrodes with different charge densities (σ) as specified (in $\mu\text{C}/\text{cm}^2$). The inset in each panel illustrates how BMIM and PF_6 ions orient near the electrode.

4.5 Anion Size Dependence of Interfacial Ionic Liquid Structure

We first examined the rearrangements of the constituent ions near the electrified graphene surface. When the electrode surface is charged, counterions accumulate close to the surface due to electrostatic forces. The counterions form an EDL that screens the electric surface charge. A comprehensive description of the EDL microstructure is necessary to reliably understand the role of anion choice on the system performance.

Figure 4.11 and Figure 4.12 show mass density profiles for [BMIM][Cl] and [BMIM][TFSI], respectively, in the direction normal to the electrode surface (z -axis). They illustrate the formation and nature of EDLs adjacent to the positively charged electrode under different conditions of electrode charging (0, 10, 40 $\mu\text{C}/\text{cm}^2$) and IL anion size (Cl⁻, TFSI⁻). We choose to only show the mass density profiles at the positively charged electrodes since we are primarily interested in the effects of anion choice on the EDL. Incidentally, the electrochemical performance of the EDLs at the negatively charged electrodes is virtually the same regardless of the anion choice, as we will present in the next section. Interested readers can refer to previous studies that have extensively investigated the structure and orientation of the EDL at negatively charged electrodes for BMIM-based ILs [42-45,56,65,73].

When the electrode is uncharged ($\sigma = 0 \mu\text{C}/\text{cm}^2$), the mass density profiles of BMIM and Cl [Fig. 4.11 (a)] show some layering that extends to 10-15 Å from the electrode surface. This is in good agreement with other simulation studies that have reported layering up to 15-20 Å for [BMIM][PF₆][56,64]. This multi-layering is indicative of a well-ordered region in which the microstructure is dominated by ion-ion

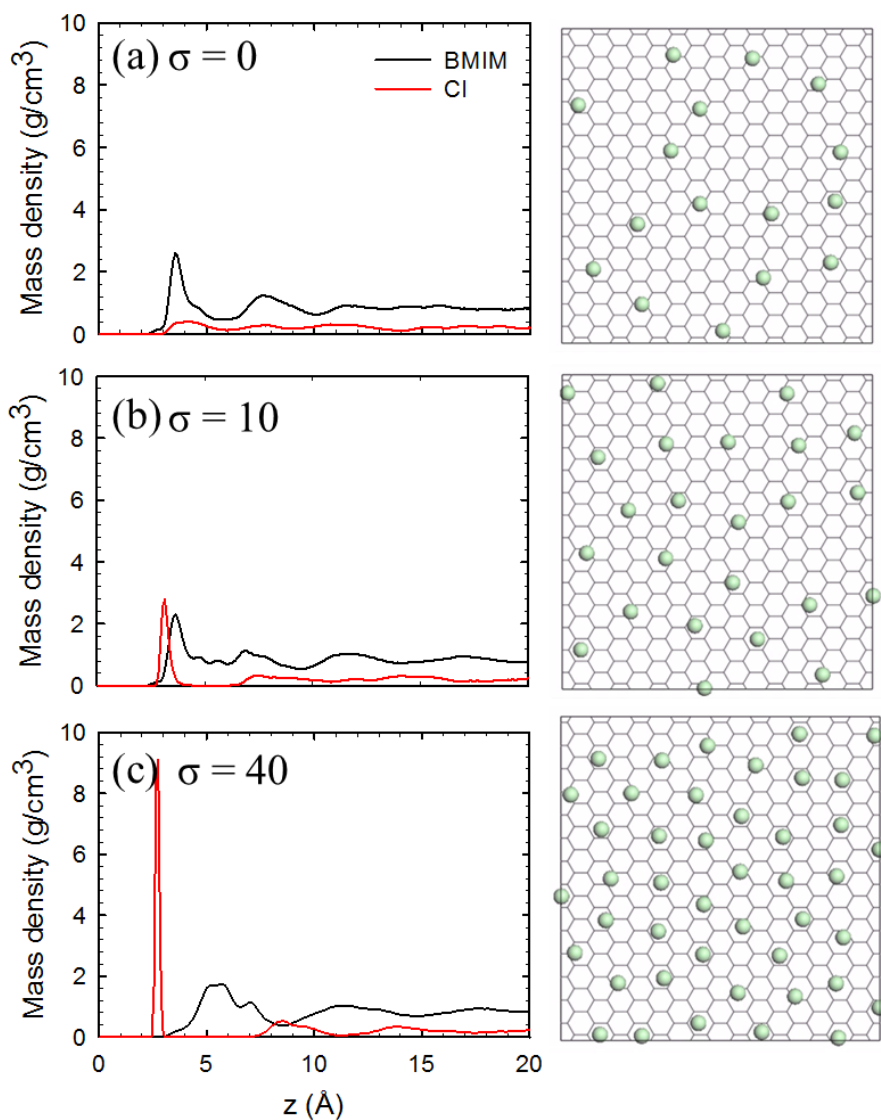


Figure 4.11 Mass density distributions of [BMIM][Cl] at the positive electrode. Different excess charge densities are specified in $\mu\text{C}/\text{cm}^2$. Each electrode is located at $z = 0$. Snapshots displayed to the right correspond to Cl anions in the first absorbed layer at the specified charge density.

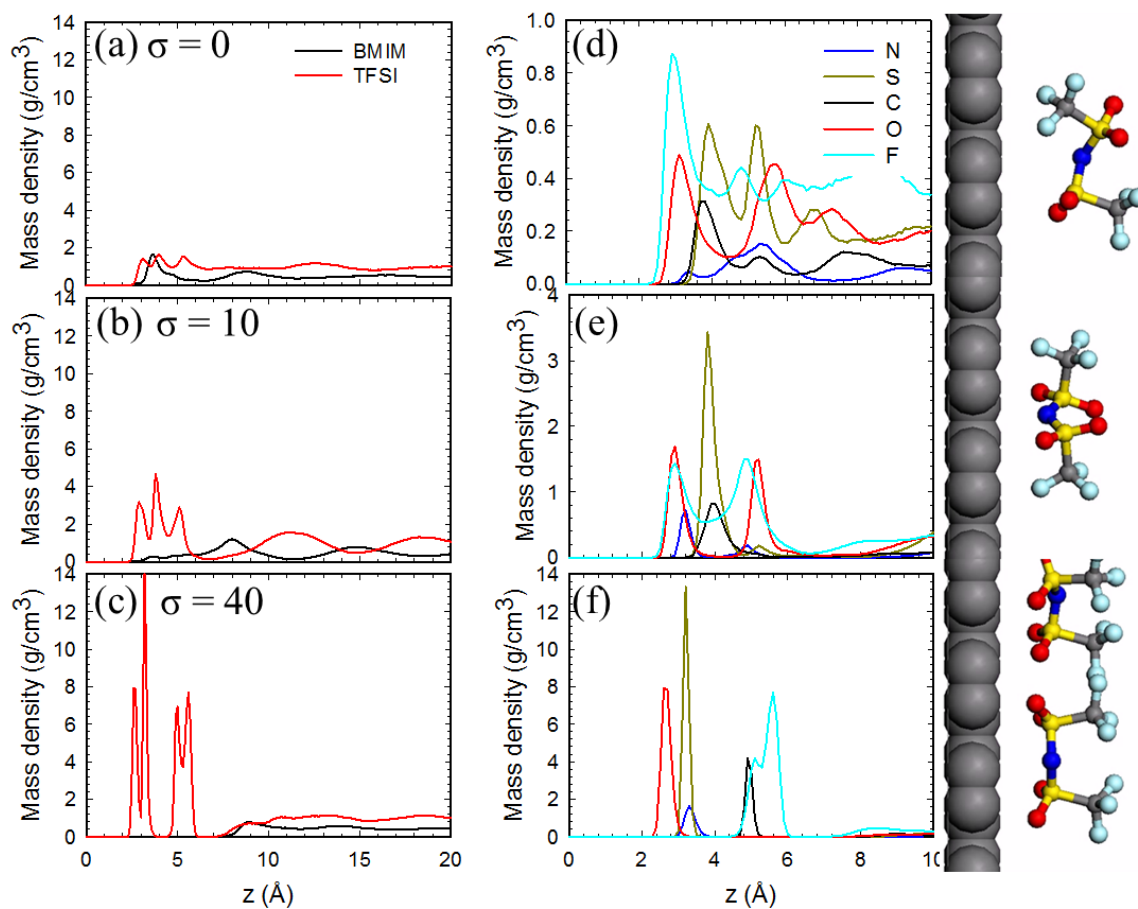


Figure 4.12 Mass density distributions of [BMIM][TFSI] at the positive electrode; (a)-(c) [BMIM][TFSI] and (d)-(f) distributions of N, S, O, C and F atoms of TFSI anion. Different excess charge densities are specified in $\mu\text{C}/\text{cm}^2$. Each electrode is located at $z = 0$. Molecular configurations displayed to the right correspond to TFSI anions at the specified charge density.

and ion-electrode interactions. The distinct first peak located around 3.5-4.0 Å arises due to the van der Waals attraction between the graphene sheet and [BMIM][Cl]. When $\sigma = 10 \mu\text{C}/\text{cm}^2$ [Fig. 4.11 (b)], the first Cl peak becomes pronounced and shifts towards the positively charged electrode while the first BMIM peak remains at nearly the same

position. When the electrode is further charged to $\sigma = 40 \mu\text{C}/\text{cm}^2$ [Fig. 4.11 (c)], the first Cl peak becomes thinner and more pronounced while the BMIM peak shifts away from the electrode.

Compared to the Cl case, the sterically larger TFSI⁻ case shows rather different behavior in its formation of EDLs. When $\sigma = 0 \mu\text{C}/\text{cm}^2$ [Fig. 4.12 (a)], the mass density profile reveals layering that extends up to 20 Å which is in good agreement with recent simulations.[80] The first layer of TFSI contains three peaks. As shown in the inset, F and O atoms constitute the closest peak to the electrode, C, S and N atoms constitute the middle peak, and the remaining SO₂ and CF₃ groups constitute the third peak. In this case when van der Waals interactions dominate, the preferred configuration of [TFSI] anions is shown in the snapshot in Figure 4.12.

At $\sigma = 10 \mu\text{C}/\text{cm}^2$, the three anion peaks become more distinguished while the BMIM⁺ peak shifts away from the electrode [Fig. 4.12 (b)]. The inset reveals that the first peak is attributed to O, F, and N atoms. Now, electrostatic interactions compete with van der Waals interactions and attract these atoms towards the electrode. The center peak is attributed to S and C and the final peak is attributed to O and F atoms. Hence, the TFSI anions reconfigure and align the five backbone atoms parallel to the electrode surface as shown in the snapshot in Figure 4.12 (b). At $\sigma = 40 \mu\text{C}/\text{cm}^2$, four distinct peaks are shown in the mass density profile [Fig. 4.12 (c)]. The first two peaks correspond to O, N, and S atoms. Among the atoms comprising TFSI, N and O are the most negatively charged ($q_N = -0.66e$, $q_O = -0.53e$). Electrostatics now dominate over van der Waals interactions, drawing these atoms closest to the electrode. In addition, the

weakly charged CF_3 groups ($q_{\text{CF}_3} = -0.13e$) fold away from the electrode, as indicated by the last two peaks. By doing so, the effective footprint of TFSI is reduced, allowing more anions to pack into the interfacial layer to screen the surface charge. In the Cl case, the anions are essentially point charges which can efficiently pack into a single layer. In contrast, the TFSI anions must undergo a series of reconfigurations in response to the charge state of the electrode.

4.6 Summary

We evaluated the microstructure of ionic liquid (IL) [BMIM][PF₆], [BMIM][TFSI], and [BMIM][Cl] near graphene electrode as a function of applied potential. Using classical molecular dynamics simulations with the OPLS-AA force field, we first determined the microstructure of [BMIM][PF₆] near the graphene electrode with varying excess surface charge densities ($\sigma = 0$ to $\pm 60 \mu\text{C}/\text{cm}^2$).

Our MD simulations clearly demonstrate the distinct alternative layering of BMIM and PF₆ in the vicinity of an electrified graphene surface, which is found to extend about 3 nm from the planar electrode while the thickness of each alternating [BMIM][PF₆] layer tends to be 7-9 Å. Analysis of the interfacial structures also shows that (i) the relatively smaller PF₆ anions are packed more densely than BMIM cations near the corresponding counter electrodes, (ii) the small and symmetric PF₆ anions pack into lattice-like structures near the counter electrode, unlike the large and complex-shaped BMIM cations, (iii) both positive and negative electrodes tend to be overshadowed by the first-layer ions unless σ is fairly large ($> 50 \mu\text{C}/\text{cm}^2$), and (iv) PF₆ counterions align a

plane of fluorine atoms parallel to the electrode. Similarly, BMIM counterions also tend to align parallel to the electrode; when $\sigma > 40 \mu\text{C}/\text{cm}^2$, the alkyl tails bend away from the electrode to allow additional packing of BMIM rings. Our results corroborate well with previous theoretical and experimental studies.

Chapter 5: Capacitance at the Ionic Liquid/Graphene Interfaces

5.1 Introduction

Besides the interfacial structure of ILs, the differential EDL capacitance in ILs has been extensively measured and characterized. The capacitance-potential ($C-\phi$) curve for ILs with metal electrodes commonly shows a convex parabolic shape with one maximum or two local maxima, which is the so-called bell-shaped or camel-shaped curve. [75-78] On the other hand, in aqueous electrolytes the EDL capacitance is known to exhibit a minimum near the potential of zero charge (PZC) and increases with applied electrode potential, yielding a concave or U-shaped $C-\phi$ curve.[48] Kornyshev[79] derived an elegant analytical expression based on the Poisson-Boltzmann lattice-gas model which suggested that the $C-\phi$ curve shape can be a function of void fraction, or compressibility, near the electrolyte-electrode interface. His work inspired many attempts to explain the $C-\phi$ curves in various shapes. Molecular-level computer simulations have been used to examine the relationship between the capacitance and microstructure of EDLs.[45,80-82] Earlier studies [83-86] tend to well capture the general trends in the formation of an EDL in response to an applied electrode potential. However, they have also shown that the EDL structure and capacitance can be a complex function of many factors such as the size, configuration and polarizability of ions, the effective dielectric constant in the electrolyte solution, and the non-electrostatic

interaction of ions with the electrode surface, which are not yet clearly understood; this leaves room for further investigation.

Carbon-based nanomaterials (such as porous carbon, carbon nanotubes, and graphene) have been regarded as viable candidates for supercapacitor electrodes due to their high surface area and good electrical conductivity. As suggested by recent computational studies, the EDL capacitance in ILs with carbon-based electrodes can be significantly influenced by the shape and surface topology of the electrode. [87-90] In addition, some experimental efforts have been made to enhance the capacitance of carbon-based EDLCs through electrode doping and functionalization.[91-93] At a semiconductor (or semimetallic) electrode-electrolyte interface, the space charge layer within the electrode may act as a capacitor in series with the EDL[94-96]; likewise, at the IL/carbon interface the carbon electrode capacitance might need to be taken into account for the interfacial capacitance. Randin and Yeager[94] first applied the semiconductor “space charge” capacitance picture for graphite with NaF. Gerischer *et al.*[97,98] later amended this theory to incorporate the electronic density of states (DOS) of graphite within the framework of semiconductor theory; their analysis suggested that the finite DOS of graphite near the Fermi level resulted in the dominance of the space charge contribution to the measured capacitance. Luryi,[99] however, first formalized the concept of quantum capacitance for low-dimensional materials such as graphene and metallic carbon nanotubes, in which the space charge treatment is inapplicable. The quantum capacitance of carbon nanostructures is directly proportional to the DOS, and can thus be altered by tuning the electronic structure through doping, functionalization,

and mechanical deformation. This may suggest that the previously observed improvements in capacitor performance from the chemical and/or mechanical modifications of carbon-based electrodes could be attributed to the enhancement in not only EDL capacitance but also quantum capacitance. Despite its importance, the relative role played by electrode and EDL in determining the interfacial capacitance still remains unclear.

In this work, we examine the interfacial capacitance graphene in IL 1-butyl-3-methyl-imidazolium hexafluorophosphate ([BMIM][PF₆]), 1-butyl-3-methyl-imidazolium bis(trifluoromethylsulfonyl) imide ([BMIM][TFSI]), 1-butyl-3-methyl-imidazolium chloride ([BMIM][Cl]) using a combination of classical molecular dynamics (MD) and density functional theory (DFT) calculations. Our particular interest lies in understanding the relative contributions of EDL capacitance and quantum capacitance to the total interfacial capacitance between graphene and [BMIM][PF₆]. Based on the microstructure of [BMIM][PF₆] near the graphene electrode by varying the electrode surface charge using MD simulations, and use the calculated distributions of BMIM and PF₆ ions to evaluate the potential variations in [BMIM][PF₆] and successively EDL differential capacitances. Then, we employ DFT calculations to estimate the quantum capacitance of pristine graphene with a brief comparison to theoretically predicted and experimentally estimated values. While the total capacitance at the graphene/IL interface is given as a series of the EDL capacitance and the quantum capacitance, our work clearly demonstrates that the quantum capacitance can play a major role in determining the overall performance of graphene/IL-based supercapacitors.

5.2 Computational Methods

Our DFT calculations were performed within the Perdew-Wang 91 generalized gradient approximation (GGA-PW91),[100] using the Vienna Ab initio Simulation Package (VASP).[101] We employed the projector augmented wave (PAW) method to describe the interaction between core and valence electrons,[102] and a planewave basis set with a kinetic energy cutoff of 400 eV. For the electronic structure calculation of pristine graphene, we used a 4-atom rectangular sheet with dimensions of $4.272 \times 2.466 \text{ \AA}^2$; here, the GGA-optimized lattice constant of 2.466 \AA was employed, which is slightly larger than the experimental value of 2.461 \AA . Periodic boundary conditions were employed in all three directions with a vacuum gap of 10 \AA in the vertical (z) direction to separate the system from its periodic images. A $(21 \times 21 \times 1)$ k -point grid in the scheme of Monkhorst-Pack[103] was used for the Brillouin zone sampling.

5.3 Results and Discussion

5.3.1 Electric Double Layer Capacitance

As demonstrated in the previous section [Fig. 4.6], the electrode excess surface charge (σ) creates an electric field at the surface (E_{ES}) that causes IL ions to redistribute, which in turn gives rise to a charge imbalance in space near the electrode. The resulting electric-potential (ϕ) profile along the surface normal direction can be obtained by solving Poisson's equation:

$$\nabla^2 \phi(z) = \rho(z) / \epsilon_0 \quad \text{with} \quad -\nabla \phi \Big|_{ES} = E_{ES} \quad (5.1)$$

where z is the distance from the electrode, ρ is the charge density averaged over a lateral z -cross section, and ε_0 is the vacuum permittivity. According to Gauss' law, $E_{ES}(\sigma)$, i.e., $E_{ES} = \sigma / \varepsilon_0$. By integrating Eq. (5.2), we can evaluate the potential variation in the IL electrolyte:

$$\phi(z) = -\frac{\sigma z}{\varepsilon_0} - \frac{1}{\varepsilon_0} \int_0^z (z - z') \rho(z') dz' \quad (5.2)$$

Figure 5.1 shows calculated potential profiles near the positive [(a)] and negative [(b)] electrodes with respect to the bulk potential (which is set equal to 0 V) for various σ as specified. Here, the positive electrode position is set at $z = 0$, and a bin size of 0.1 Å was used in obtaining laterally averaged $\rho(z)$. The results show that the potential changes mostly occur across the EDL, indicating that the accumulated counterions effectively screen E_{ES} . It is also worth noting that at a given σ , the absolute value of the potential drop ϕ_D (the electrode surface potential minus the electrolyte bulk potential) at the positive electrode side is consistently less than that of the negative electrode side. This is primarily due to the cation-anion size difference; that is, smaller PF₆ anions are packed more tightly such that E_{ES} can be screened over a smaller EDL thickness which yields a smaller $|\phi_D|$.

When $E_{ES} = 0$, the vdW interactions between the electrode and IL ions may cause a charge imbalance and consequently a potential drop in the interface region, which is the so-called potential of zero charge (PZC). For the graphene/IL system considered, the PZC turns out to be nearly 0 V, consistent with previous theoretical study;[64] recall that

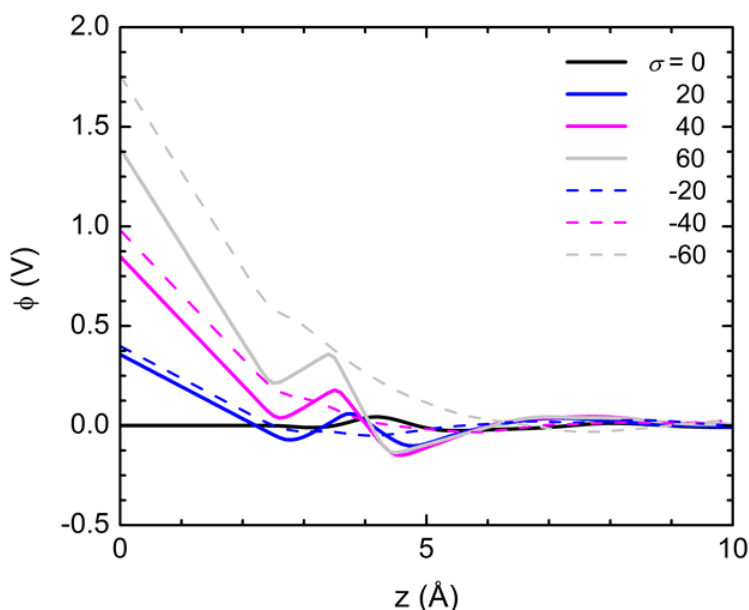


Figure 5.1 Potential (ϕ) profiles along the z -axis at varying excess charge densities as specified (in $\mu\text{C}/\text{cm}^2$). To facilitate comparisons, the ϕ near the negative graphene electrode is shown on a negative scale, i.e. the shown $\phi = -\phi$. In all cases, $\phi = 0$ for the bulk electrolyte and each electrode is located at $z = 0$.

the number densities of BMIM and PF_6 near the electrode are very comparable. The PZC may increase as the size difference between anion and cation increases; the tighter packing of smaller ions than larger ones at the electrode-electrolyte interface can lead to differences in their number densities. Previous studies reported that the respective PZC values for $[\text{OMIM}][\text{PF}_6]/\text{graphite}$ [64] and $[\text{BMIM}][\text{BF}_4]/\text{glassy carbon}$ [77] could be as high as 0.15 V and 0.085 V, respectively; note that OMIM is larger in size than BMIM while BF_4 is smaller than PF_6 , such that both $[\text{OMIM}][\text{PF}_6]$ and $[\text{BMIM}][\text{BF}_4]$ have a larger size difference than $[\text{BMIM}][\text{PF}_6]$.

The capacitance of an EDL can be obtained from the relationship between σ and ϕ_D , i.e., $C = \sigma/\phi_D$ (integral) or $d\sigma/d\phi_D$ (differential). The differential capacitance is a measure of how the EDL microstructure responds to potential perturbations caused by a variation in σ . Hence, the differential approach is often preferred in investigating the properties of EDLs; the differential EDL capacitance (C_D) can be measured using low frequency impedance spectroscopy.[104]

Based on the σ - ϕ_D plot in Fig. 5.2(a), we computed C_D by differentiating σ with respect to ϕ_D ; the data points were smoothed using a negative exponential technique¹⁰⁵ for the first derivative calculation. As presented in Fig. 5.2(b), the predicted C_D - ϕ_D curve is a convex parabola (bell shaped) with a maximum of $4.7 \mu\text{F}/\text{cm}^2$ at $\phi_D = 0.7 \text{ V}$. Here, we should point out that the value of $C_D (= d\sigma/d\phi_D)$ is rather sensitive to the choice of data smoothing scheme, but the overall shape of the C_D curve tends to be more or less same. Note that the peak position appears at a positive value of ϕ_D , which is related to the difference in packing efficiency between cation and anion. That is, smaller PF_6 anions are more effectively packed than larger BMIM cations, yielding a smaller $\Delta\phi_D$ for a given $\Delta\sigma$ and consequently a larger C_D . Likewise, the C_D value monotonically decreases with increasing $|\sigma|$ (or $|\phi_D|$) due to the gradually reduced packing efficiency (as demonstrated earlier), while the PF_6 side consistently exhibits a higher C_D at a given $|\phi_D|$ than the BMIM side. It is also worth noting that the decrease of C_D becomes less steep as $|\phi_D|$ increases at both sides; this is apparently attributed to the continuing saturation of

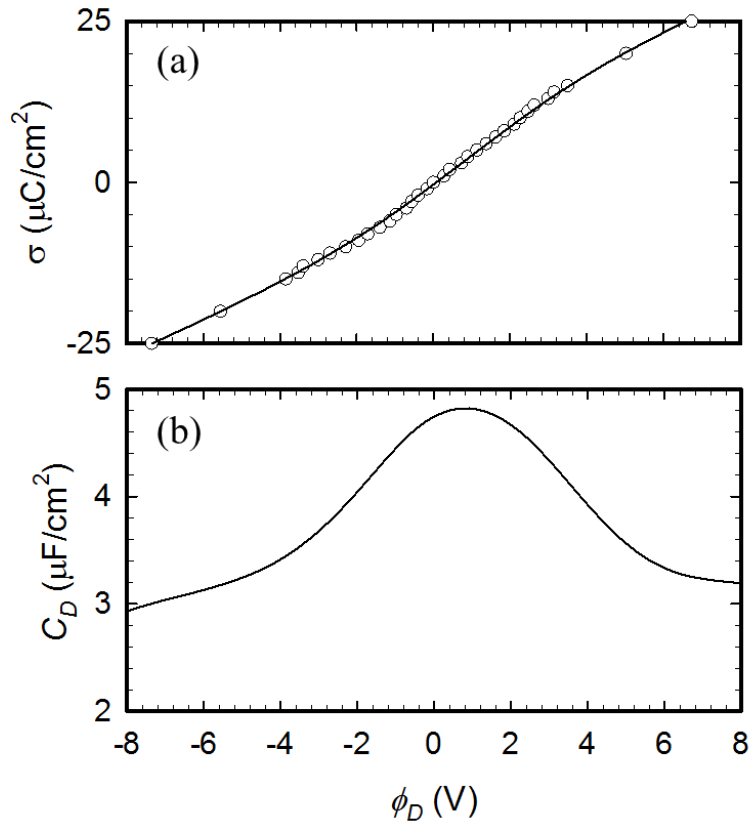


Figure 5.2 (a) Excess electrode charge density (σ) and (b) differential double layer capacitance (C_D) as a function of the potential drop across the EDL (ϕ_D). In (a), the circles represent data from MD simulations and the solid line is fit from smoothing the data (see Ref. 105).

electrode surface by counterions, leading to an increase in EDL thickness as the counterions accumulate in multiple layers.

Besides such bell-shaped features,[75,106] previous experimental and theoretical studies have widely reported that the C_D curve also exhibits various camel-like shapes[76,78] in IL-electrolyte/metal-electrode systems. The shape and magnitude of C_D curve can be a complex function of multiple factors which may include polarizability of

ions at the interface, size difference between cations and anions, and non-electrostatic (specific) adsorption of ions on the electrode surface. For the graphene/IL system, the possible polarization of graphene and IL ions at the interface could significantly affect the electrode charge distribution, the space charge density, and the EDL capacitance. The effect of specific adsorption, however, should be unimportant considering the weak adsorption of [BMIM][PF₆] ions on the pristine graphene surface. Nonetheless, our calculations and previous other studies[75,76,78,106] unequivocally demonstrate that the C_D of EDLs decreases with increasing $|\phi_D|$ due to the reduced packing efficiency of ions; this is particularly true when $|\sigma|$ is large enough such that the electrostatic forces play a dominant role in determining the EDL structure. We should note, however, that the impact of graphene-based electrodes with structural and chemical modifications on the structure and capacitance of EDLs remains largely unknown.

5.3.2 Electrode Quantum capacitance

Two-dimensional (2D) graphene-based electrodes have been found to have a quantized capacitance.[99] The quantum capacitance of graphene is defined as $C_Q = d\sigma/d\phi_G$, where $d\sigma$ and $d\phi_G$ refer to the variations of charge density and local potential in graphene, respectively. For the pristine graphene sheet, the DOS is symmetric and linear around the Fermi level (E_F). In addition, if we assume the graphene electrochemical potential μ is rigidly shifted by $e\phi_G$, [107] the excess charge density σ from the electron density (n) can be written by:

$$\sigma = e(n_o - n_\mu) = e \int_{-\infty}^{+\infty} D(E) [f(E) - f(E - e\phi_G)] dE \quad (5.3)$$

where $D(E)$ is the 2D DOS, $f(E)$ is the Fermi-Dirac distribution function, E is the relative energy with respect to E_F , e is the elementary charge, and the subscripts o and μ refer to the neutral and non-neutral cases, respectively. With the analytical expression of σ , the C_Q of graphene is given by:

$$C_Q = d\sigma / d\phi_G = e^2 \int_{-\infty}^{+\infty} D(E) F_T(E - \mu) dE \quad (5.4)$$

where the thermal broadening function [$F_T(E)$] is also expressed as $F_T(E) = -df/dE = (4kT)^{-1} \text{sech}^2(E/2kT)$.

For the 2D graphene case, we can approximate the DOS near the Dirac point by[108]

$$D(E) \approx \frac{g_s g_v}{2\pi (\hbar v_F)^2} |E| \quad (5.5)$$

where g_s and g_v are the respective spin and valley degeneracies ($= 2$), \hbar is the reduced Planck's constant, and v_F is the Fermi velocity of carriers ($\approx 10^8$ cm/s).[109] Recall that $E(k)$ is approximately linear near the Dirac point.[110] The DOS of graphene can also be calculated using DFT calculations. Figure 5.3 presents a comparison of the DOS obtained from our DFT calculations and from Eq. (5.5), showing good agreement.

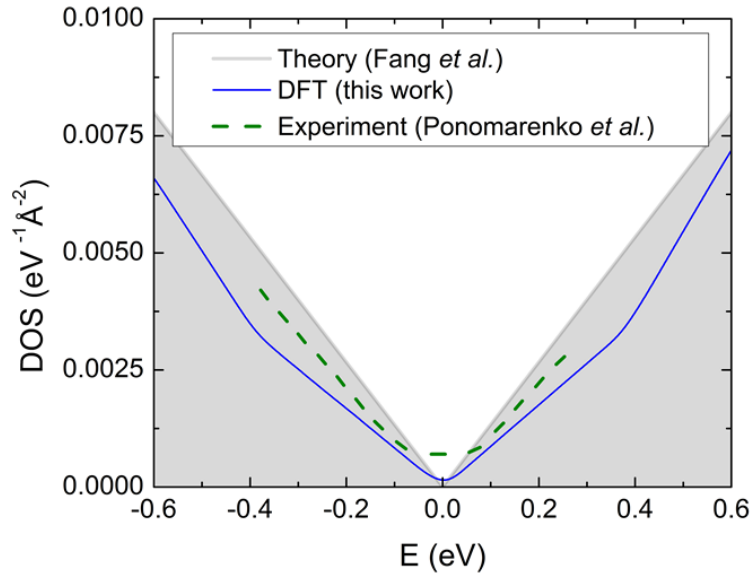


Figure 5.3 Comparison of pristine graphene's density of states (DOS) from theory (Ref. 108), experiment (Ref. 113), and DFT.

A few groups have recently attempted to determine the C_Q of graphene based on measurements of graphene-gated systems[95,111-113] from which the graphene C_Q is decoupled from the oxide capacitance (C_{ox}). However, the experimental C_Q values remain widely scattered and often significantly deviate from the above calculation results especially near $\phi_G = 0$, [113] as illustrated in Fig. 5.4. One possible source of this disagreement is from the estimation of C_{ox} , which is calculated either from Hall measurements or geometrically ($C_{ox} = \epsilon_0 \epsilon_r / t_{ox}$, where t_{ox} is the oxide layer thickness). Other possible sources include defects in the graphene, the oxide surface, and/or potential fluctuations within the electrode as a result of the graphene-oxide surface interaction. As shown in Fig. 5.4, the calculated C_Q (300 K) for the pristine graphene based on the DOS

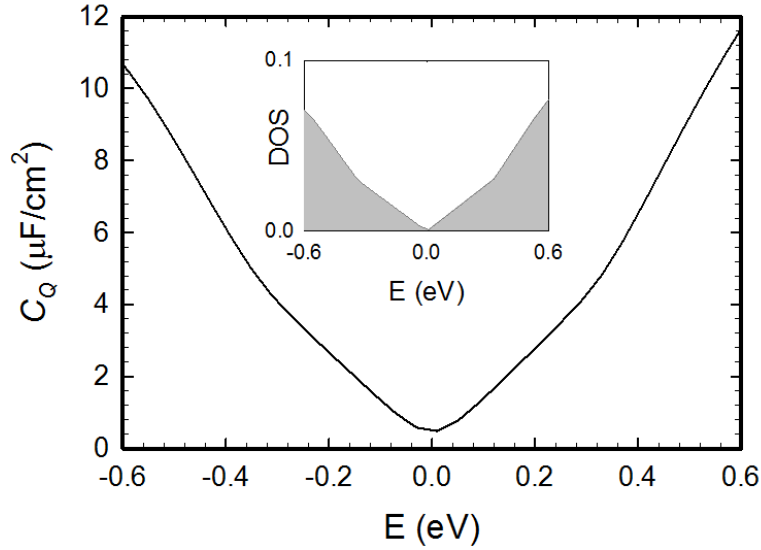


Figure 5.4 Calculated quantum capacitance (C_Q) of pristine graphene based on the DOS (inset). $E = 0$ eV indicates the position of the Fermi level

from DFT exhibits a U-shaped curve, contrary to C_D , with a minimum around 0.58 $\mu\text{F}/\text{cm}^2$; note that $C_Q \neq 0$ when $\phi_G = 0$ due to the thermal broadening of the electron energy distribution, and as expected the C_Q curve is symmetric about $\phi_G = 0$. We should note that the possible influence of graphene-IL interactions on the DOS and C_Q have been neglected in this analysis for simplicity. However, we expect the qualitative impact of the DOS and C_Q on the total capacitance (described below) to remain the same.

5.3.3 Total interfacial capacitance

The total capacitance (C_T) at the electrode/IL interface can be represented as a series of C_Q and C_D , as shown in Fig. 5.5, i.e., $1/C_T = 1/C_Q + 1/C_D$. With the C_Q and C_D

Schematic of total capacitance

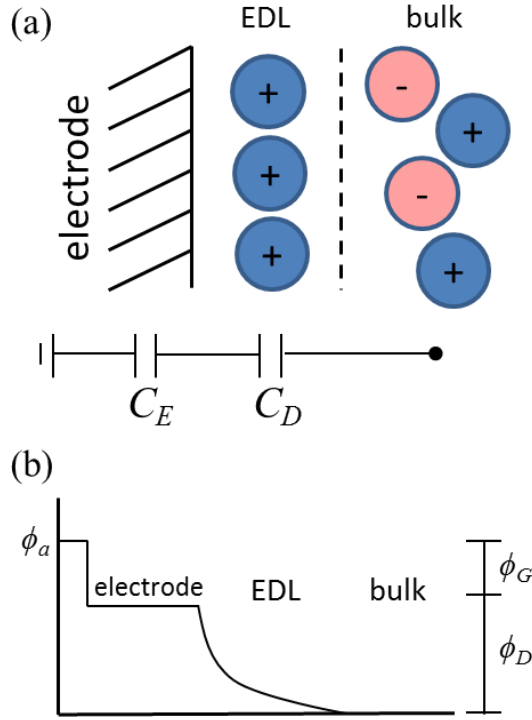


Figure 5.5 Schematic of the graphene/IL interface, with an illustration of the equivalent circuit with series capacitance from the electrode and double layer [(a)] and an idealized potential profile [(b)].

values calculated above, we estimated C_T as a function of applied potential ϕ_a (with respect to the potential of the bulk electrolyte, i.e., $\phi_a = \phi_G + \phi_D$) as shown in Fig. 5.5. Here, the relationship between C_Q and C_D with ϕ_a was obtained through σ ; recall that $C_Q/C_D \propto \sigma \propto \phi_G/\phi_D$. The C_T curve is U-shaped, in direct contrast to the bell-shaped C_D curve [Fig. 5.2 (b)]; this is apparently attributed to the dominance of C_Q when ϕ_a is sufficiently small ($|\phi_a| < 1.0$ V). With increasing ϕ_a , the contribution of C_D becomes

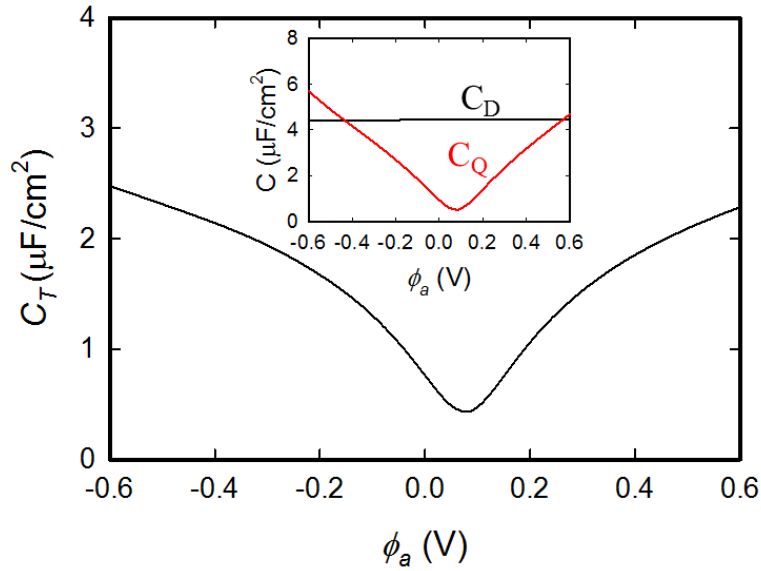


Figure 5.6 Total interfacial capacitance (C_T) as a function of applied potential (ϕ_a). The inset shows corresponding EDL capacitance (C_D) and quantum capacitance (C_Q).

important. Recent experiments[77,95,96] have also broadly shown evidence for similar U-shaped C_T curves in supercapacitors based on graphite-like electrodes and IL electrolytes; some specific features such as minimum/maximum values, peak/valley positions and curvature vary case by case, possibly due to the strong dependence of C_Q and C_D on the structure and purity of the carbon-based electrodes. Now it is worth pointing out that, unlike the carbon-based case, the capacitance of metal electrodes (such as platinum and gold) is much larger than C_D ; hence, $C_T \approx C_D$, which could explain why the metal/IL interface mostly exhibits a bell-shaped or camel-shaped C_T curve. [75,76,78,106]

Our study clearly highlights the important role of C_Q in determining the capacitance performance of graphene-based supercapacitors. Knowing that the C_Q of graphene-like materials is directly related to the DOS, the modification of the electrode electronic structure by substitutional dopants, functional groups, and/or structural disorder/strain will significantly affect the overall capacitor performance of graphene/IL systems; however, the effect of the chemically and/or mechanically modified graphene-based electrodes still remains largely unexplored, and is, we think, an important subject for further research.

5.4 Anion Size Dependence of Electrical Double Layer Capacitance

Figure 5.7 depicts the potential over the channel length calculated at several surface charge densities for [BMIM][Cl] (a) and [BMIM][TFSI] (b). In all cases, the charge densities listed were applied to both the positive electrode ($z = 0 \text{ \AA}$) and negative electrode ($z = 100 \text{ \AA}$). Each curve in Figure 5.7 demonstrates features predicted by the Helmholtz model, namely a sharp, linear potential drop in the Helmholtz layer. The profiles near the negative electrode in both Figures 3A and 3B display similar characteristics – the potential drop and the length scale of the potential drop are indistinguishable at each surface charge density. The potential drop, V_{DL} , is defined by $V_{electrode} - V_{bulk}$ in which $V_{electrode}$ is the electrode potential and V_{bulk} is the screened bulk potential. In both anion cases, the adsorption of [BMIM] ions onto the negative electrode is virtually unaffected by the anion choice.

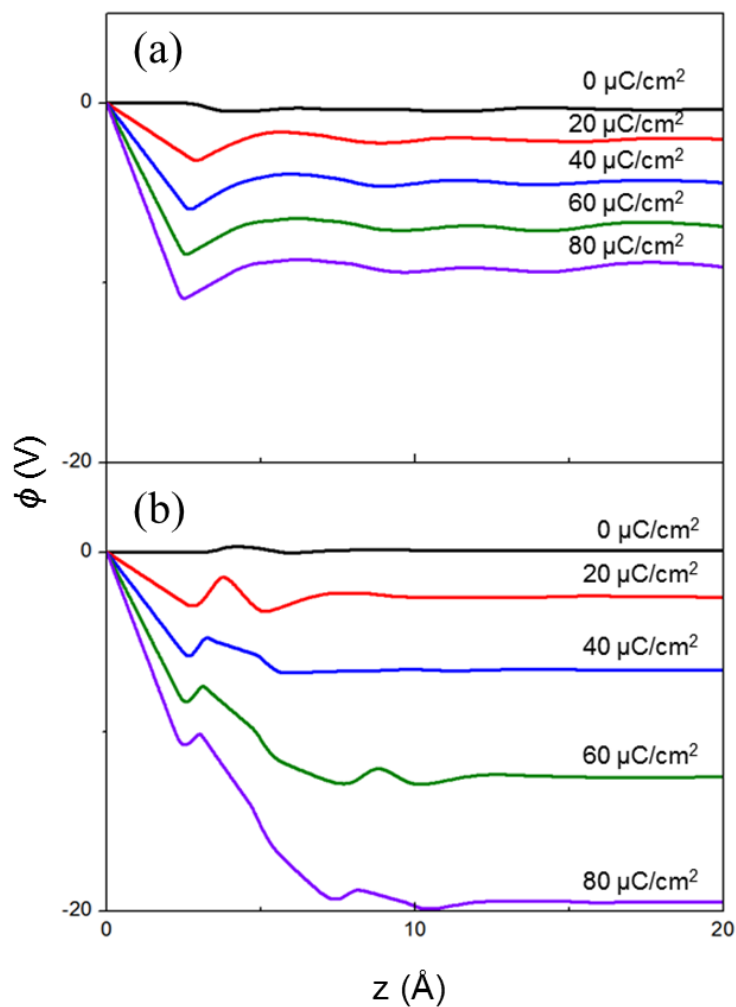


Figure 5.7 Potential profiles for (a) [BMIM][Cl] and (b) [BMIM][TFSI] at the positive electrode with specified surface charge densities. Each electrode is located at $z = 0$

A comparison of the profiles in Fig. 5.7 (a) and (b) near the positive electrodes highlight differences that can be quantified in terms of the potential drop and its characteristic length scale – the distance in which the bulk is effectively screened from the surface charge. In Fig. 5.7 (a), the potential drop occurs over a length scale of 3-4 Å

for all surface charge densities. This length scale is exactly the thickness of the [Cl] EDL calculated from the mass density profiles, further enforcing that the important physics occur in the EDL. In Fig. 5.7 (b), the potential drop occurs over larger length scales.

At low surface charge densities up to $40 \mu\text{C}/\text{cm}^2$, the length scale is 4-7 Å. Above this, the length scale increases to 8-12 Å, which reflects the formation of an additional layer of [TFSI] anions at the positive electrode interface. Once again, the potential drop occurs over a length scale that equals the thickness of the EDL.

In addition, magnitude of the potential drop across the [TFSI] EDL for each surface charge density shown in Fig. 5.7(b) is twice as large as that of the [Cl] EDL while comparable to the potential drop across the [BMIM] EDL. At $\sigma = 80 \mu\text{C}/\text{cm}^2$, for example, $\phi_D = 10 \text{ V}$ for the [Cl] EDL while $\phi_D = 20 \text{ V}$ for the [TFSI] EDL and $\phi_D = -20 \text{ V}$ for the [BMIM] EDL. The potential drop across the [Cl] EDL is much less than that across the [TFSI] layer due to differences in packing. The [Cl] anions pack into a dense, single layer such that the charge is highly localized in a thin layer. On the other hand, [TFSI] anions pack into much thicker layers with charge delocalized across the layer. Assuming the dielectric properties of the two anion EDLs are similar, it follows from Poisson's equation that VDL across the [TFSI] EDL is greater than that of the [Cl] EDL due to the charge delocalization from poor packing.

Figure 5.8 shows the capacitance-voltage profiles for [BMIM][Cl] (a) and [BMIM][TFSI] (b). In both Fig. 5.8 (a) and (b), the capacitance decays significantly at the negative electrode as the potential is increased. This similarity between the two is expected since the [BMIM] EDL does not noticeably change when paired with either [Cl]

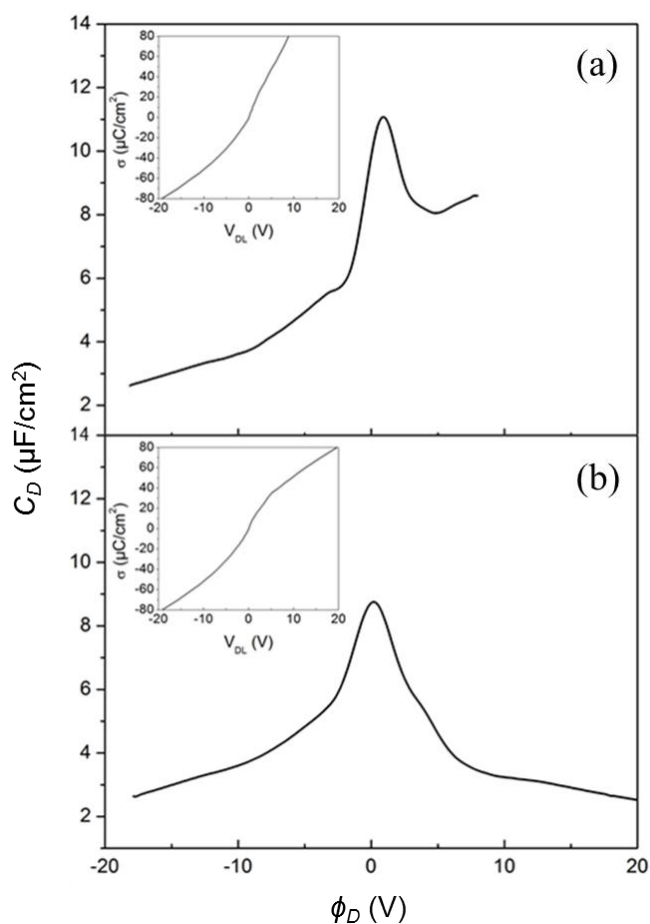


Figure 5.8: Differential double layer capacitance (C_D) as a function of potential drop across the EDL (ϕ_D); (a) [BMIM][Cl] and (b) [BMIM][TFSI]. Insets show excess electrode charge density.

or [TFSI].

Near the potential of zero charge, both curves exhibit bell-shaped characteristics similar to that previously predicted from the mean-field theory by Kornyshev [79]. The capacitance of the [TFSI] EDL saturates at 0.2 V ($8.8 \mu\text{F}/\text{cm}^2$) whereas the [Cl] EDL capacitance saturates at 0.9 V ($11.1 \mu\text{F}/\text{cm}^2$). This indicates that [TFSI] anions adsorbed

on the electrode saturate the surface at a lower potential than [Cl] anions. The comparatively greater capacitance of the [Cl] EDL to the [TFSI] EDL is expected since the V_{DL} of the [TFSI] EDL is greater than the [Cl] EDL's at the same surface charge density. However at high potentials, the capacitance continues to decay in the [TFSI] EDL while the capacitance plateaus in the [Cl] EDL.

5.5 Summary

We evaluated the interfacial capacitance between graphene and ionic liquid (IL) [BMIM][PF₆], [BMIM][TFSI], and [BMIM][Cl] as a function of applied potential (ϕ_a). Here, the total capacitance (C_T) at the graphene/IL interface is given as a series of the electric double layer (EDL) capacitance (C_D) and the quantum capacitance of graphene (C_Q), i.e., $1/C_T = 1/C_D + 1/C_Q$. Using classical molecular dynamics simulations with the OPLS-AA force field, we first determined the microstructure of [BMIM][PF₆] near the graphene electrode with varying excess surface charge densities, and then used the spatial ion distributions obtained to calculate the potential variations in [BMIM][PF₆] and successively EDL differential capacitances. The quantum capacitance of pristine graphene was estimated from the electronic density of states (DOS) calculated using density functional theory (DFT).

From the calculation results of potential profiles and EDL capacitances, we see that (i) the potential changes mostly occur within the first layer of counterions, providing evidence of one-ion thick compact EDL formation, (ii) the potential drop across the EDL was consistently larger at the negative electrode compared to the positive electrode, (iii)

the EDL capacitance showed distinct, bell-shaped characteristics, and (iv) the capacitance of the “wings” at positive potential saturated at a higher value than at negative potential. Analysis of the EDL structure reveals that those observations are primarily attributed to differences in the size and shape of PF₆ anions and BMIM cations. While the packing efficiencies of both ions decrease with increasing $|\sigma|$, the PF₆ anion has an overall higher packing density than the BMIM cation. Note that in our calculations all atom charges were kept fixed; however, we also conceive that the shape and magnitude of the C_D curve can be a significant function of atomic polarization at the graphene/IL interface. Nonetheless, according to this work and other previous studies, it is highly plausible that the C_D of EDLs decreases with increasing $|\sigma|$ due to the reduced packing efficiency of ions, resulting in bell-shaped or camel-shaped C_D curves.

The C_Q of pristine graphene calculated based on the DOS from DFT exhibits a U-shaped curve, contrary to the bell-shaped C_D , with a minimum of nearly zero. As a consequence, the C_T at the graphene/IL interface is predicted to be U-shaped (which has been also seen by previous experiments), due to the dominance of C_Q when the applied potential is sufficiently small ($|\phi_a| < 1.0$ V, while the contribution of C_D becomes important with increasing ϕ_a). Our work clearly highlights the importance of C_Q in graphene-based supercapacitors, although more sophisticated calculations might be required for improved predictions of C_D by taking into account the aforementioned atomic polarization. Note that the C_Q of graphene-based materials is directly related to the electronic structure which can be modified by substitutional dopants, functional groups, and/or structural disorder/strain. However, the impact of such chemical and/or

mechanical modifications on the capacitor performance of graphene/IL systems remains largely unexplored, which warrants further investigation.

Chapter 6: Nitrogen Doping Effect on Capacitance Enhancement

6.1 Introduction

Electric double layer capacitors (EDLCs), also known as supercapacitors, have garnered much attention as electrical energy storage devices owing to their high rate capabilities and long cycle lifetimes. [114,115] Ionic liquids (ILs), “solvent-free” ions that are in the liquid state at room temperature, are a promising class of electrolytes due to their wide electrochemical windows, high chemical and thermal stability, extremely low volatility, and non-flammability.[116–119] Carbon-based materials (such as porous carbon, carbon nanotubes, and graphene) have been regarded as a viable candidate for supercapacitor electrodes due to their high surface area and good electrical conductivity. However due to the lower energy density of EDLCs compared to other electrochemical storage devices,[114,115,118] efforts must be made to increase their capacitance.

Experiments have shown that nitrogen (N) doping of graphene-like electrodes can significantly enhance EDLC capacitance in comparison to undoped electrodes. Jeong *et al.*[120] reported a specific capacitance around 280 F/g for N-doped graphene in aqueous and organic electrolytes, a four-fold increase from undoped graphene; they claimed that the capacitance increased due to enhanced binding interactions between N dopants in the basal plane and electrolyte ions. Other researchers also showed that N-doped graphene can increase the capacitance by 20-40% [121,122] in KOH[121] or Et₄NBF₄/propylene

carbonate[122], or by 3 times in KOH[123]; this improvement may be attributed to pseudocapacitive effects, although the exact mechanisms remain unknown.[121, 123]

While the interactions between dopants and electrolyte may influence the double layer capacitance, the total capacitance can also be affected by the electrode's capacitance. Recent experimental[124,125] and theoretical[126] work have shown that the total capacitance (C_T) of an ionic liquid/graphene-based electrode is given as a series of the double layer capacitance (C_D) and quantum capacitance (C_Q); the capacitance strongly depends on the relative contributions from both. Luryi[127] proposed that the C_Q of low dimensional materials such as graphene is proportional to the electronic density of states (DOS), which may be altered from chemical modification. To date, however, the effects of N-doping on both C_Q and C_D have yet to be reported.

In this work, we investigate the influence of N-doping on the interfacial capacitance (C_T) for 1-butyl-3-methyl-imidazolium hexafluorophosphate ([BMIM][PF₆]) IL using combined density functional theory (DFT) and classical molecular dynamics (MD) calculations. Our particular interest lies in understanding the relative contributions of EDL capacitance and quantum capacitance to the total interfacial capacitance with N-doped graphene and [BMIM][PF₆] as compared to the undoped case. For our systems, pseudocapacitive effects should be insignificant since [BMIM][PF₆] is chemically inert. We have chosen to separately investigate two commonly observed N-configurations from experimental[120,128] characterization: (1) substitutional N (N_1) in which a C atom is replaced with a N atom and (2) trimerized pyridine-type N (N_3V) in which three two-

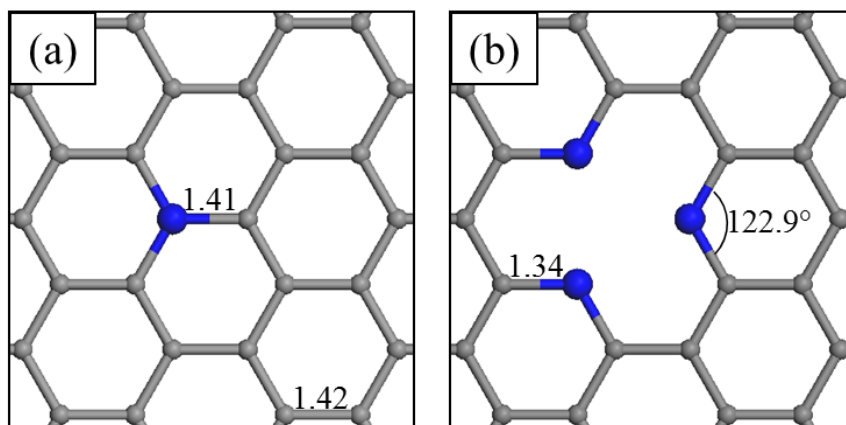


Figure 6.1 Schematic of the (a) substitutional nitrogen site (N_1) and (b) trimerized pyridine-type nitrogen site (N_3V). Gray and blue balls are C and N atoms, respectively, and bond lengths are in Å

coordinated N atoms surround a vacancy. We first employ DFT to predict the impact of each type on C_Q , which is proportional to the DOS.[126] We then consider the impact of N-doping on the microstructure, potential variation, and C_D of the EDL using DFT/MD simulations. Finally, we compare the capacitance of the two N-doped cases to the undoped case.

6.2 Computational methods

6.2.1 Density functional theory

The atomic and electronic structures of N-doped and pristine graphene sheets were calculated using DFT within the Perdew-Wang 91 generalized gradient approximation (GGA-PW91),[129] as implemented in the Vienna Ab initio Simulation Package[130] (VASP). We employed the projector augmented wave (PAW) method to

Table 6.1 Calculated partial atomic charges of substitutional N and neighboring C atoms at specified surface charge densities.

| | $\sigma = 0$ | $\sigma = 5.43$ | $\sigma = -5.43$ |
|---|--------------|-----------------|------------------|
| N | -1.14 | -1.13 | -1.15 |
| C | 0.28 | 0.29 | 0.27 |
| C | 0.27 | 0.28 | 0.26 |
| C | 0.27 | 0.28 | 0.26 |

Table 6.2 Calculated partial atomic charges of pyridine-type N and neighboring C atoms at specified surface charge densities.

| | $\sigma = 0$ | $\sigma = 5.43$ | $\sigma = -5.43$ |
|---|--------------|-----------------|------------------|
| N | -1.12 | -1.10 | -1.14 |
| C | 0.65 | 0.65 | 0.64 |
| C | 0.56 | 0.56 | 0.56 |
| N | -1.11 | -1.10 | -1.14 |
| C | 0.58 | 0.59 | 0.58 |
| C | 0.66 | 0.67 | 0.66 |
| N | -1.14 | -1.12 | -1.13 |
| C | 0.54 | 0.55 | 0.62 |
| C | 0.63 | 0.56 | 0.59 |

describe the interaction between ion cores and valence electrons,[131] and a planewave basis set with a kinetic energy cutoff of 400 eV. In this work, we considered two different N-doping configurations including single N atom substitution (referred to as N_1 hereafter) and trimerized pyridine-type (N_3V), as illustrated in Fig. 6.1. The pristine/ N_1 and N_3V graphene sheets were modeled using rectangular 32-atom (corresponding to $8.544 \times 9.866 \text{ \AA}^2$) and 112-atom ($17.088 \times 17.265 \text{ \AA}^2$) supercells, respectively; here, the GGA-optimized lattice constant of 2.466 \AA was employed, which is slightly larger than the experimental value of 2.461 \AA . Periodic boundary conditions were employed in all three directions with a vacuum gap of 10 \AA in the vertical (z) direction to separate the graphene system from its periodic images. For the Brillouin zone integration, we used a $(12 \times 12 \times 1)/(6 \times 6 \times 1)$ Monkhorst-Pack mesh of k -points to determine the optimal geometries and total energies of the 32-atom/112-atom systems, and sufficiently increased the k -point mesh to ensure convergence of electronic structure calculations. The optimized structures for the N_1 and N_3V systems from our DFT-GGA calculations are presented in Fig. 6.1; the predicted lattice distortions induced by N-doping are in good agreement with previous calculation results[132]. N-doping induced changes in the atomic charge distribution of graphene were determined using grid-based Bader analysis, and are shown in Table 6.1 and Table 6.2.

6.2.2 Classical molecular dynamics

We employed MD simulations with the OPLS-AA force field[133,134] to determine the microstructure of [BMIM][PF₆] near the graphene electrode; details on the

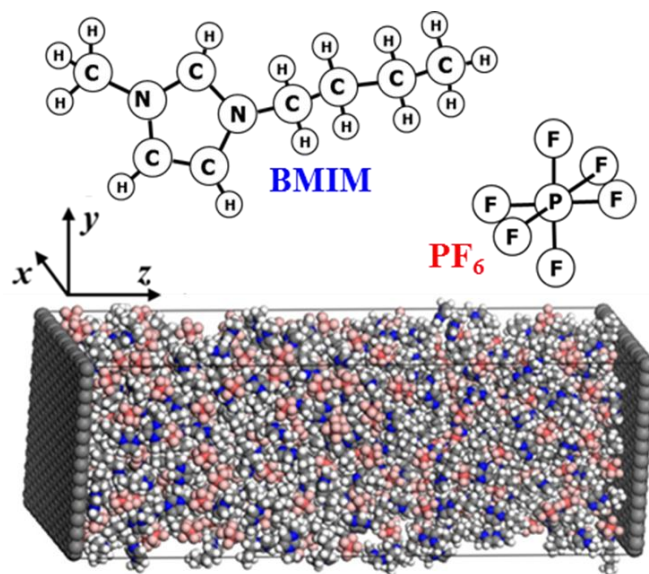


Figure 6.2 Schematic of BMIM, PF_6 , and the simulation box. Planar graphene sheets are placed at the two ends of the simulation domain. White, blue, and gray balls indicate H, N, and C atoms in BMIM, and red and pink balls indicate P and F atoms in PF_6 . Periodic boundary conditions are applied in the x and y directions.

force field parameters can be found in Ref. 126. As illustrated in Fig. 6.2, the simulation system considered consisted of 346 $[\text{BMIM}][\text{PF}_6]$ pairs between two electrodes separated by 100 Å; the lateral size of each graphene electrode is $34.18 \times 34.53 \text{ \AA}^2$, corresponding to 448 C atoms. The distance between the electrodes was chosen large enough such that the electrolyte maintained bulk properties in the middle region of the system.

For the N-doped graphene structures, 12 substitutional N atoms (corresponding to 2.7 at.% doping concentration) and 4 trimerized pyridine-type defects were distributed in the N_1 and N_3V graphene systems, respectively. We investigated uncharged and charged electrodes with a surface charge density of $\sigma = \pm 5.43 \text{ \mu C/cm}^2$. In the pristine graphene

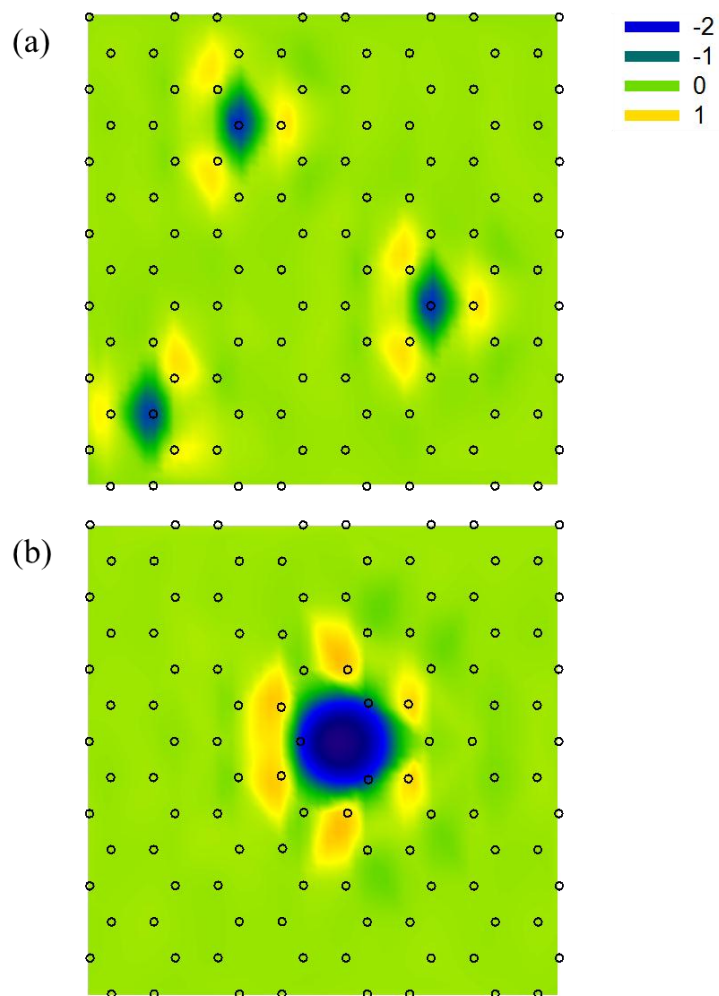


Figure 6.3 Color map (2D) showing the excess charge distribution on neutral (a) N₁ and (b) N₃V graphene. The excess charge is obtained from Bader charge analysis from DFT and plotted using the filled contour plot option in SigmaPlot 12; each region is linearly interpolated with a discrete value of excess charge (in e) as indicated by the color legend.

case, the atomic charges were assigned evenly throughout the lattice (± 0.0089 e /atom when $\sigma = \pm 5.43$ $\mu\text{C}/\text{cm}^2$). However in the N-doped cases, excess electrons/holes appeared rather concentrated around N atoms; in MD simulations, we used the atomic

charge distributions from the Bader charge analysis for the N_1 and N_3V graphene systems (see Fig. 6.3).

We ran each MD simulation initially at 1000 K for 1.2 ns followed by 3 ns at 300 K to equilibrate the system using 1 fs timesteps. Production runs were carried out for 4 ns with atomic positions recorded every 4 ps. All runs were in the NVT ensemble with the temperature controlled by a Nose-Hoover thermostat[135] with a 100 fs damping parameter. All MD simulations were performed with the Large-scale Atomic/Molecular Massively Parallel Simulator (LAMMPS) program.[136] MD results reported herein were obtained from the average of four independent simulations with different initial atomic configurations. Further details about the MD simulations are described in Ref. 126.

6.3 Results and Discussion

The total interfacial capacitance (C_T) between graphene and [BMIM][PF₆] IL was computed from a series of the electric double layer (EDL) capacitance (C_D) and the quantum capacitance of graphene (C_Q), i.e., $1/C_T = 1/C_D + 1/C_Q$. In the following sections, we present the calculations of C_Q and C_D , and based on the results, discuss their relative contributions to the C_T of the graphene/IL system.

6.3.1 Electrode Quantum capacitance

The quantum capacitance of graphene is defined as $C_Q = d\sigma/d\phi_G$, where $d\sigma$ and $d\phi_G$ refer to the variations of charge density and local potential in graphene, respectively.

Provided that the electrochemical potential μ of the graphene electrode is rigidly shifted by $e\phi_G$, [137] C_Q can be given by [126]

$$C_Q = e^2 \int_{-\infty}^{+\infty} D(E) F_T(E - \mu) dE \quad (6.1)$$

where $D(E)$ is the electron density of states (DOS), $F_T(E)$ is the thermal broadening function $[(4kT)^{-1} \text{sech}^2(E/2kT)]$, E is the relative energy with respect to the Fermi level E_F , and e is the elementary charge.

For pristine graphene, the valence and conduction bands touch and both bands exhibit conical band dispersion near the Dirac point, where the Fermi level is located [Fig. 6.4 (a)]. As also shown in Fig 6.4 (a), the calculated DOS of graphene using DFT-GGA is clearly demonstrated to be symmetric and linear near the Dirac point.

The electronic structure of graphene can be substantially altered by the presence of N impurities and/or C vacancies. Figure 3 also shows the band structure and DOS of N-doped graphene sheets considered. In the case of N_1 (single N atom substitution) graphene [Fig. 6.4 (b)], the Fermi level shifts up into the conduction band of pristine graphene due to electron injection into the π -electron system; note that N has one more electron than C, and thus each $N \rightarrow C$ substitution provides an extra electron to the graphene. The extra electron tends to spread rather broadly over the N atom and its neighboring C atoms, as demonstrated by the isosurface plot of the corresponding band-decomposed charge densities [Fig. 6.4 (b)]. While the Fermi level position is a function of N concentration, at a 3.1 at.% doping level, there exists one partially-filled defect state near the Fermi level; therefore, we can expect that the largely delocalized state will be

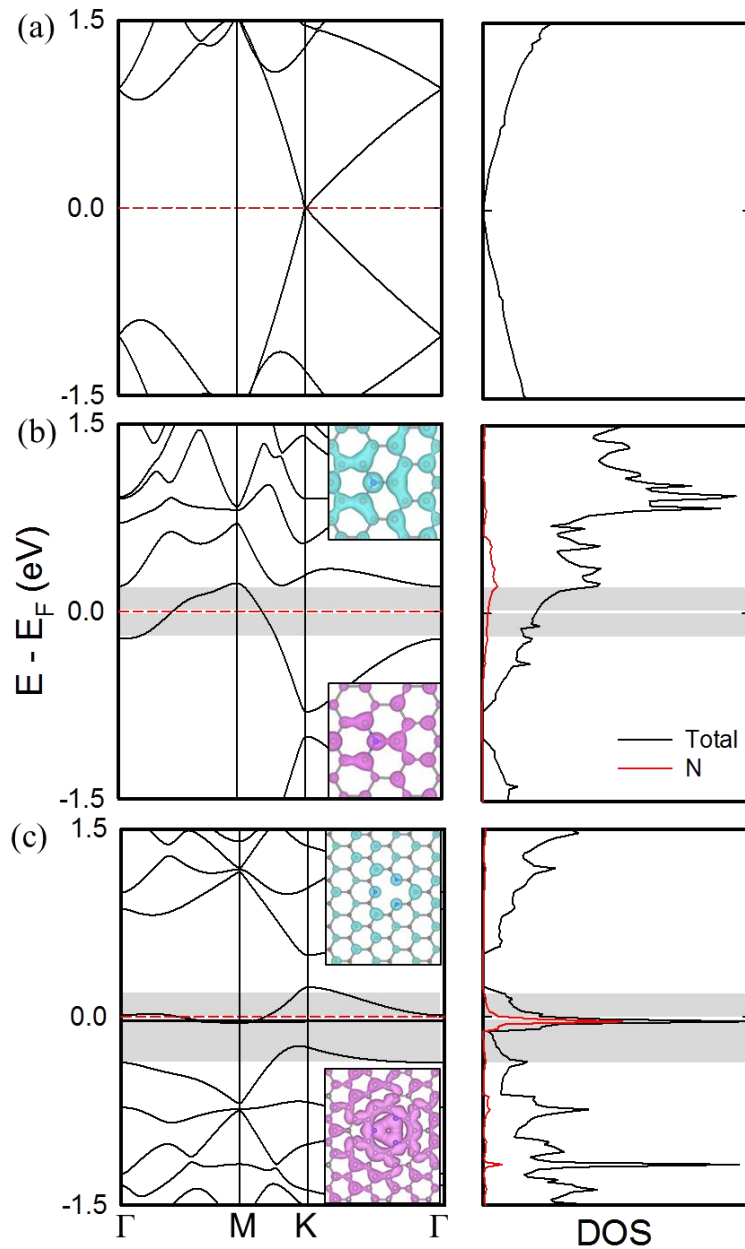


Figure 6.4 Band structures (left panels) and electronic density of states (right panels) for (a) pristine, (b) N_1 , and (c) N_3V graphene. The dotted red line (left panels) indicate the Fermi level position. The insets (left panels) show the band-decomposed charge density isosurfaces for their respective shaded regions above and below the Fermi level ($\pm 0.0005 e/\text{\AA}^3$).

first emptied (or filled) when extra holes (or electrons) are added (see the corresponding charge density isosurface plots in Fig. 6.4 (b)).

In the case of N_3V (trimerized pyridine-type) graphene [Fig. 6.4(c)], the Fermi level moves down inside the valence band of pristine graphene due to electron deficiency; note that N_3V has one less electron than C_4 (defect-free graphene). At 2.7 at.% of N-doping, our band structure calculation shows the existence of three states near the Fermi level. i.e., two degenerate quasi-localized states and one partially-filled delocalized state. The distinct DOS peak at 0.05 eV below E_F is due primarily to the quasi-localized states associated with N lone pairs, as shown by the corresponding (band-decomposed) charge density isosurface plot. We can expect, therefore, that when excess holes are injected, the states associated with the N lone pairs will be emptied first.

Using Eq. 6.1 with the calculated DOS, we obtained the C_Q of the pristine, N_1 , and N_3V graphene systems at 300 K, as presented in Fig. 6.5. The C_Q of pristine graphene is U-shaped with a minimum around $0.45 \mu\text{F}/\text{cm}^2$ at $\phi_G = 0$ V. The C_Q for N_1 and N_3V at $\phi_G = 0$ V are around 22 and $44 \mu\text{F}/\text{cm}^2$, respectively; this dramatic improvement is apparently due to the additional impurity states near E_F . In the N_1 graphene case, C_Q gradually increases as ϕ_G increases and peaks at $45 \mu\text{F}/\text{cm}^2$ at $\phi_G = 0.3$ V. As ϕ_G decreases below 0 V, C_Q tapers towards $0 \mu\text{F}/\text{cm}^2$ at -0.85 V. In the N_3V graphene case, C_Q sharply decreases to around $5\text{-}10 \mu\text{F}/\text{cm}^2$ when $\phi_G < -0.2$ V and $0 \mu\text{F}/\text{cm}^2$ when $\phi_G = 0.4$ V.

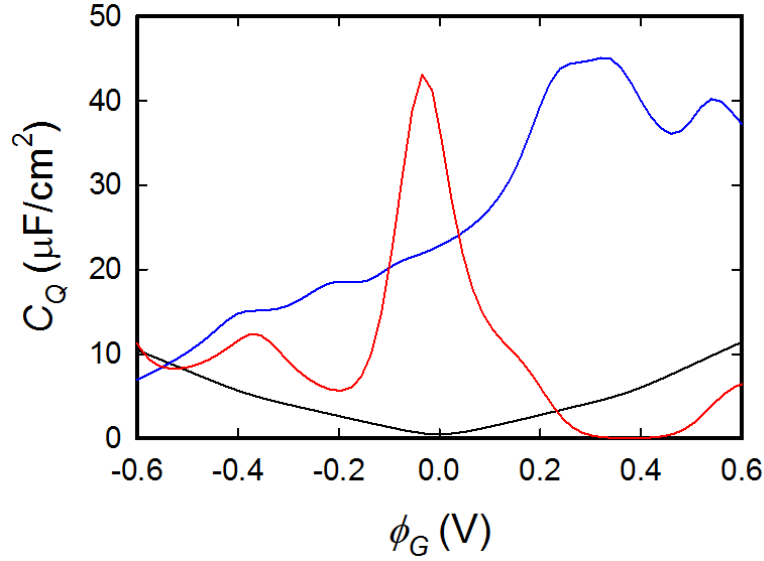


Figure 6.5 Comparison of the calculated quantum capacitance (C_Q) of pristine, N_1 , and N_3V graphene as a function of the local electrode potential (ϕ_G)

We have thus far presented an analysis pertaining to two ideal types of N doping in graphene; in reality, however, a fabricated N-doped graphene electrode may have numerous types of N-dopants and other possible structural defects.[120,128] In such a mixed system, the impact of the individual dopant types does not alter the electronic structure in simply an additive manner. Additional interactions between dopant types can also create unique states and alter the electronic structure (see Fig. 6.6), but numerous combinations of these mixed dopants exist and is outside the scope of this study. We should also note that the possible influence of graphene-IL interactions on the DOS and C_Q have been neglected in this analysis for simplicity. However, it is clear that N-doping can lead to significant changes in the electrode quantum capacitance.

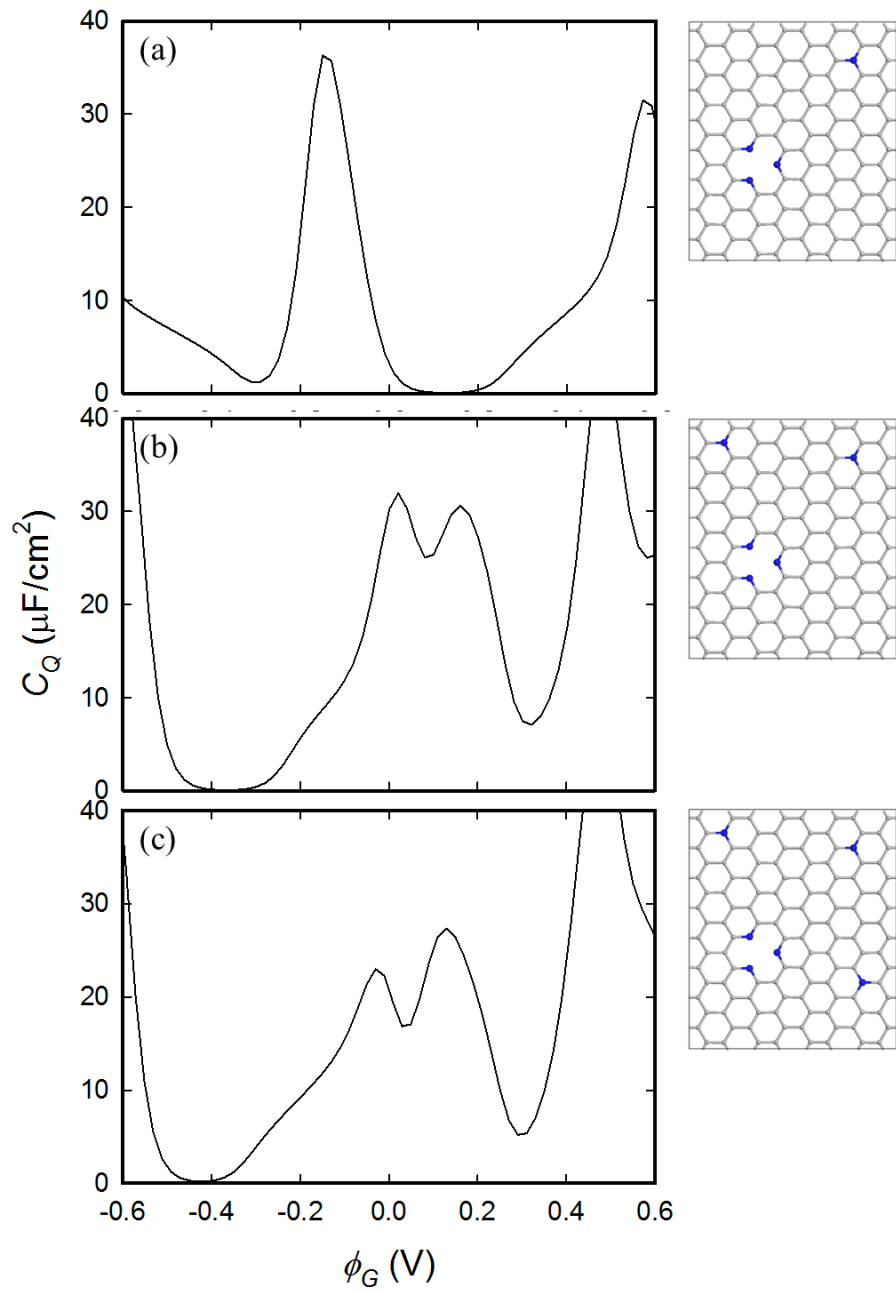


Figure 6.6 The calculated quantum capacitance (C_Q) for the mixed N-dopant configurations shown in the right panels; (a) N₃V and single N₁, (b) N₃V and two N₁, and (c) N₃V and three N₁

6.3.2 Electric Double Layer Capacitance

The capacitance of an EDL can be obtained from the relationship between excess electrode surface charge (σ) and potential drop within the EDL (ϕ_D); that is, $C_I = \sigma/\phi_D$ (integral) or $C_D = d\sigma/d\phi_D$ (differential). We first calculated the integral capacitances at $\sigma = \pm 5.43 \mu\text{C}/\text{cm}^2$ for the pristine, N_1 , and N_3V graphene cases. For each system, the EDL capacitance was evaluated based on the microstructure of [BMIM][PF₆] IL near the electrified electrode determined using MD simulations, as described in the following section.

Figure 6.7 presents a comparison between the mass density profiles of BMIM and PF₆ at $\sigma = \pm 5.43 \mu\text{C}/\text{cm}^2$ for pristine [(a)], N_1 [(b)], and N_3V [(c)] graphene. Each of the panels [(a)-(c)] displays an alternating cation/anion layering that extends 25-30 Å from the electrodes, after which the IL structure becomes nearly bulk-like; this layering behavior is consistent with previous experimental observations.[138-140] Near the positive electrode ($z = 0$ Å), PF₆ exhibits three distinct peaks adjacent to the electrode [in (a)-(c)]; these peaks correspond to planarly-aligned F, P, and F atoms, which arise primarily due to the electrostatic attraction between the positive electrode and the negatively-charged F atoms. Near the negative electrode ($z = 100$ Å), the sharp peak [in (a)-(c)] corresponds to BMIM ions which tends to align parallel to the electrode surface.[141,142]

The presence of N dopants and/or C vacancies affects the charge distribution throughout the electrode surface as stated earlier, which in turn influences the IL

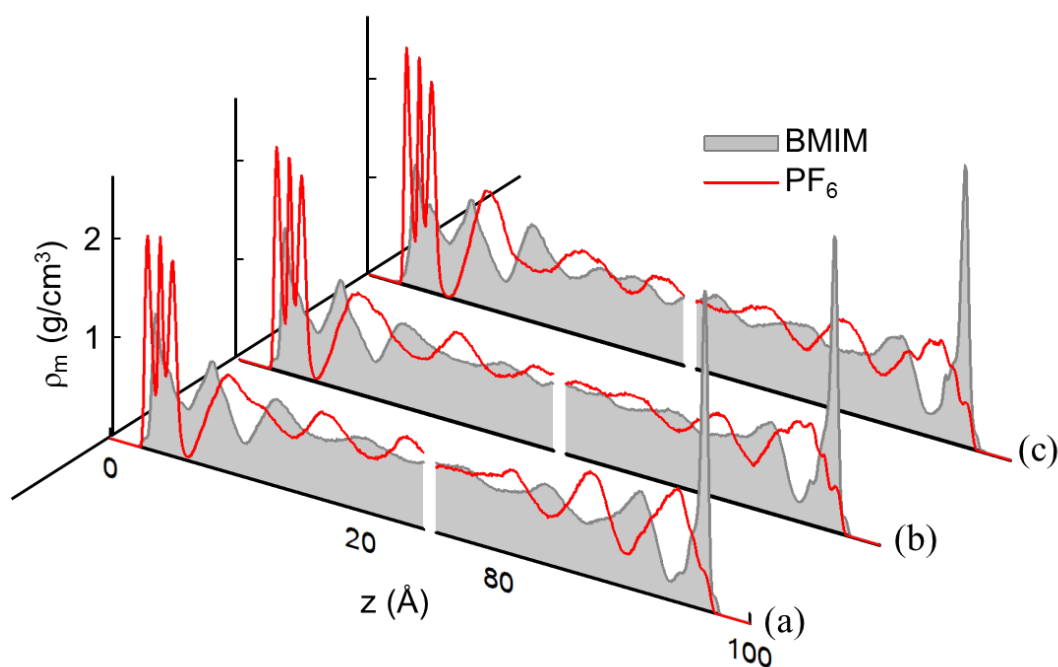


Figure 6.7 BMIM and PF_6 mass density (ρ_m) profiles for (a) pristine, (b) N_1 , and (c) N_3V graphene systems along the z -axis. The positive (negative) electrode is located at $z = 0 \text{ \AA}$ (100 \AA).

arrangement near the surface. In both N_1 and N_3V graphene cases, the positively charged BMIM rings have a tendency to lie near the negatively charged N atoms as a result of their electrostatic attraction [Fig. 6.10]. However, the influence of N doping on the IL distribution along the normal (z) direction appears to be insignificant (when the N concentration is about 2.7% as considered here); note that the average density of the first IL layer deviates at most by 3.3% compared to the undoped case.

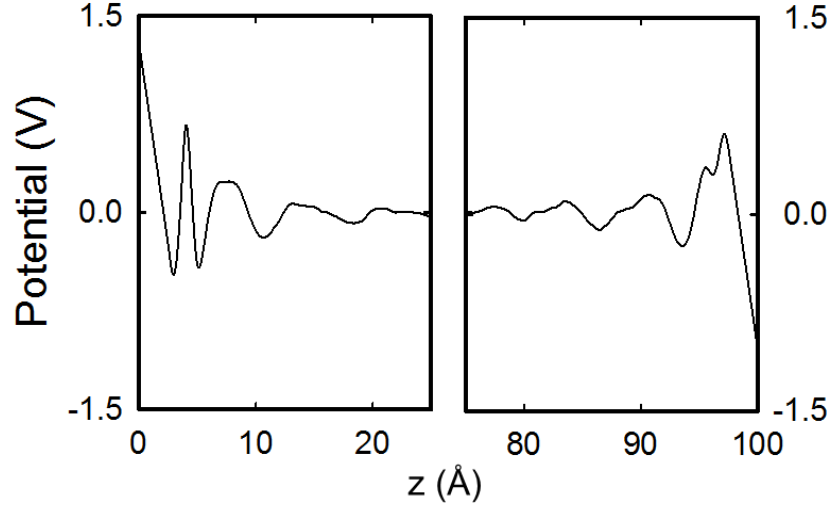


Figure 6.8 Potential (ϕ) profiles along the z -axis at $\sigma = \pm 5.43 \mu\text{C}/\text{cm}^2$ for the pristine graphene system. The positive (negative) electrode is located at $z = 0 \text{ \AA}$ (100 \AA) and $\phi = 0$ for the bulk electrolyte.

For each system, the space charge variation in the IL electrolyte was calculated based on the distribution of IL ions with fixed atomic charges. We then obtained ϕ along the surface normal direction for a given σ from Poisson's equation

$$\phi(z) = -\frac{\sigma z}{\epsilon_0} - \frac{1}{\epsilon_0} \int_0^z (z - z') \rho(z') dz' \quad (6.2)$$

where z is the distance from the electrode, ρ is the charge density averaged over a lateral z -cross section, and ϵ_0 is the vacuum permittivity.

Figure 6.8 shows a calculated potential profile for the pristine graphene case near the positive [left] and negative [right] electrodes with respect to the bulk potential (which is set equal to 0 V) for $\sigma = \pm 5.43 \mu\text{C}/\text{cm}^2$. Here, a bin size of 0.1 \AA was used in obtaining laterally averaged $\rho(z)$. The results show that the potential variation mostly

Table 6.3 Potential drop across the EDL (ϕ_D) and integral capacitance (C_I) for pristine, N₁, and N₃V graphene systems at $\sigma = \pm 5.43 \mu\text{C}/\text{cm}^2$.

| | Pristine | N ₁ | N ₃ V |
|---|----------|----------------|------------------|
| $\sigma = -5.43\mu\text{C}/\text{cm}^2$ | | | |
| ϕ_D (V) | 1.30 | 1.26 | 1.33 |
| C_I ($\mu\text{F}/\text{cm}^2$) | 4.18 | 4.30 | 4.09 |
| $\sigma = 5.43\mu\text{C}/\text{cm}^2$ | | | |
| ϕ_D (V) | -1.02 | -1.00 | -1.05 |
| C_I ($\mu\text{F}/\text{cm}^2$) | 5.30 | 5.41 | 5.18 |

occurs across the EDL, indicating that the accumulated counterions effectively screen the surface electric field. The ϕ_D near the positive (negative) electrode was 1.30 (-1.02) V. The potential profiles for the N₁ and N₃V graphene cases [not shown] are found to exhibit similarity to the pristine graphene case; the variation in ϕ_D among the three systems considered appears to be less than 5% [Table 6.3].

In Table 6.3, we present the predicted C_I at $\sigma = 0$ and $\pm 5.43 \mu\text{C}/\text{cm}^2$ for each case. Note that in actuality, $C_I = \sigma/(\phi_D - \phi_Z)$ [143], where ϕ_Z is the potential of zero charge (which refers to the potential drop in the interface region due to a charge imbalance when $\sigma = 0 \mu\text{C}/\text{cm}^2$). For [BMIM][PF₆] near the intrinsic graphene sheet, the ϕ_Z is nearly zero (≈ 0.02 V). Similarly, the ϕ_Z for the N₁ and N₃V graphene cases are also nearly zero (≈ 0.01 and 0.02 V, respectively). Hence, the expression for C_I is simplified to $C_I = \sigma/\phi_D$ for all three cases. According to our calculations, the C_I values near the negative (positive)

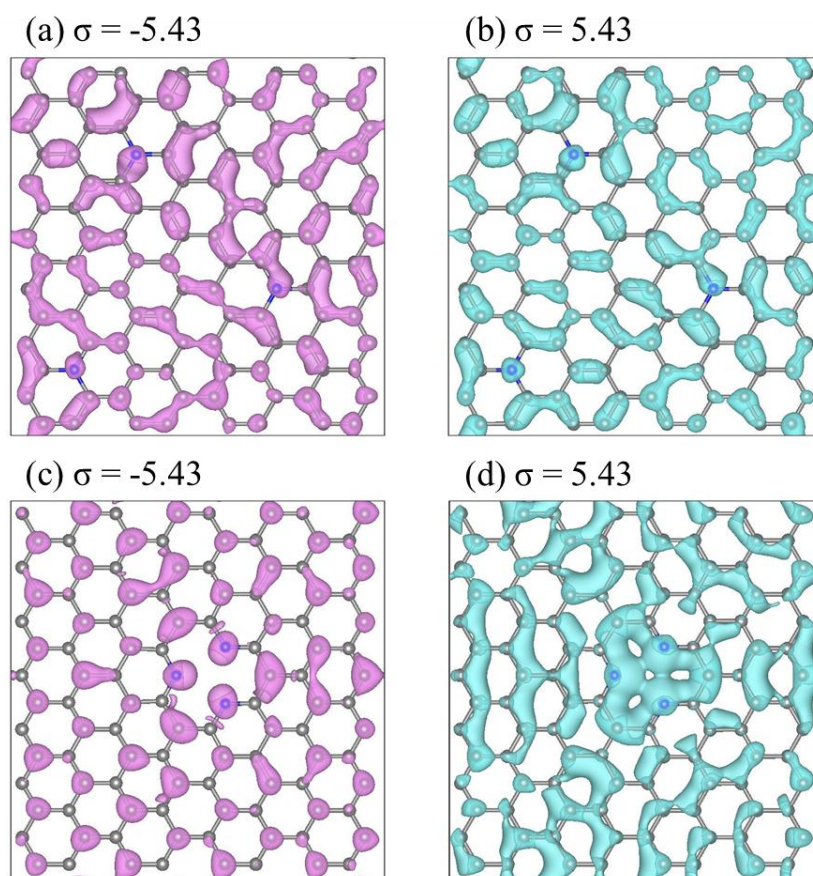


Figure 6.9 Excess charge density isosurfaces ($\pm 0.0003 e/\text{\AA}^3$) for N_1 and N_3V graphene at varying σ (in $\mu\text{C}/\text{cm}^2$).

electrodes of 4.30 and 4.09 (5.41 and 5.18) $\mu\text{F}/\text{cm}^2$ for the N_1 and N_3V graphene systems, respectively, only slightly deviate from 4.18 (5.30) $\mu\text{F}/\text{cm}^2$ for the intrinsic case by at most 2.9%. This clearly suggests that N doping has little effect on the EDL capacitance at the N concentrations considered here ($\approx 2.7\%$ for both N_1 and N_3V graphene). Here, we should note that we neglect the possible polarization of graphene and IL ions at the interface and its effect on the electrode charge distribution, the space charge density, and

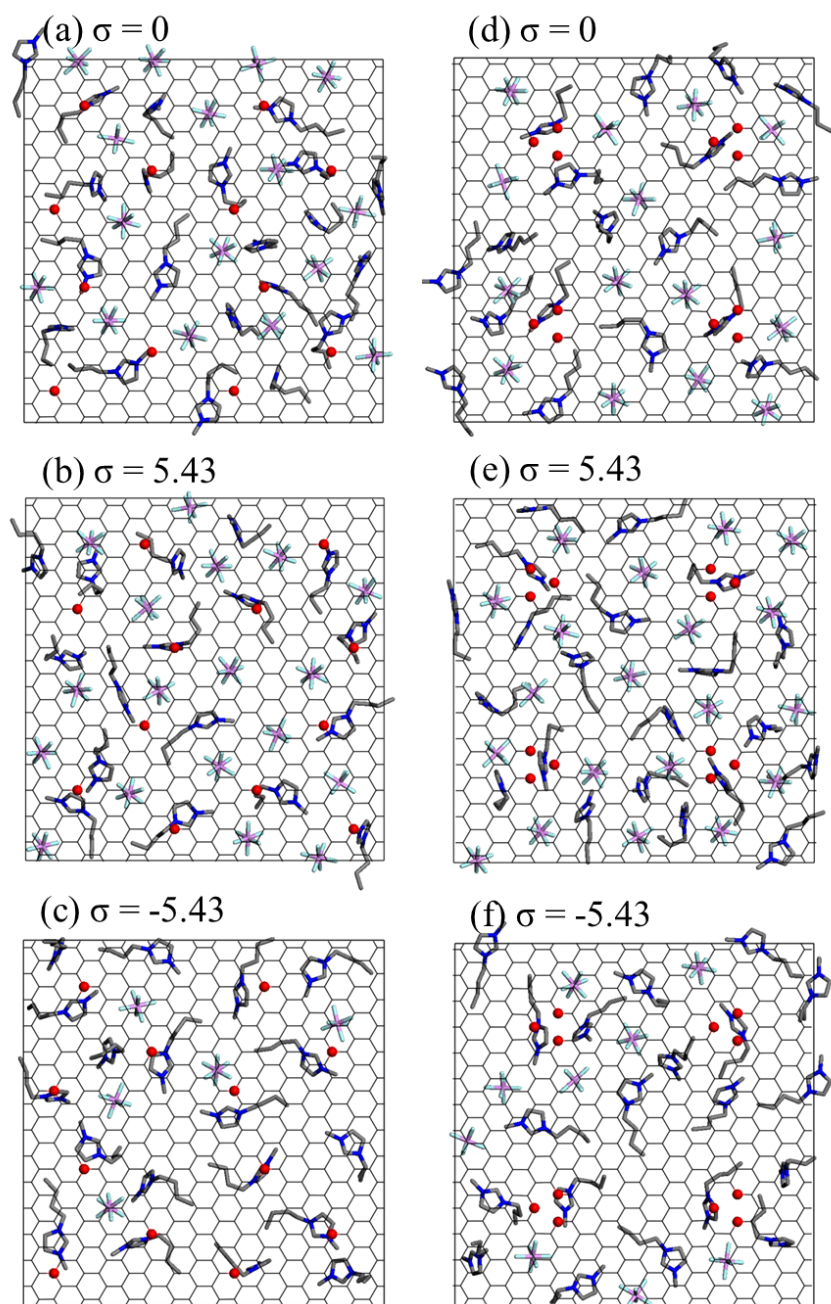


Figure 6.10 Snapshot of the IL ions closest to the electrode at various excess charge densities (in $\mu\text{C}/\text{cm}^2$). Thin gray sticks depict the graphene lattice. The red/blue clusters and blue/gray sticks represent PF_6 and BMIM, respectively. The BMIM rings have a tendency to lie near the N sites, which are shown as red balls.

the EDL capacitance, which merits further investigation. In addition, we cannot exclude the possibility that very high levels of doping might lead to noticeable deviations from the intrinsic case due to multiple factors, including possible specific adsorption of IL ions and enhanced interfacial electrostatic interactions.

6.3.3 Total Interfacial Capacitance

We attempted to evaluate the total interfacial capacitance (C_T) (which is given as a series of the EDL capacitance and the quantum capacitance) as a function of applied potential (ϕ_a). Here, we considered the differential EDL capacitance (C_D) which is often preferred in investigating the properties of EDLs; the C_D is an indicator of how the EDL microstructure responds to potential perturbations caused by a variation in σ , and can be measured using low frequency impedance spectroscopy[144].

Since N-doping has no significant effect on the EDL capacitance, we only calculated the C_D for the intrinsic graphene case (which we assume is representative of both the N_1 and N_3V graphene cases). As shown in Fig. 6.11, the predicted C_D - ϕ_D curve is nearly flat for $|\phi_D| < 0.6$ V with a maximum of $4.7 \mu\text{F}/\text{cm}^2$ at $\phi_D = 0.7$ V. Note that the peak position appears at a positive value of ϕ_D , which is related to the difference in packing efficiency between cation and anion.[126] That is, smaller PF_6 anions are more effectively packed than larger BMIM cations, yielding a smaller $\Delta\phi_D$ for a given $\Delta\sigma$ and consequently a larger C_D . Likewise, the C_D value monotonically decreases with

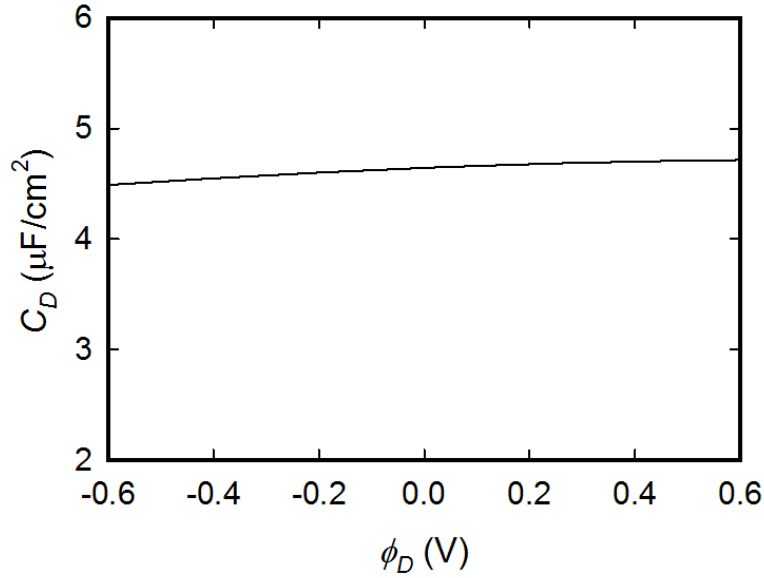


Figure 6.11 The differential double layer capacitance (C_D) as a function of the potential drop across the EDL (ϕ_D) for the pristine graphene system.

increasing $|\sigma|$ (or $|\phi_D|$) due to the gradually reduced packing efficiency, while the PF_6 side consistently exhibits a higher C_D at a given $|\phi_D|$ than the BMIM side [not shown].

Figure 6.12 shows predicted C_T - ϕ_a curves for the pristine [(b)], N_1 [(c)], and N_3V [(d)] graphene systems, from the calculated C_Q and C_D above; recall $1/C_T = 1/C_Q + 1/C_D$. Here, as sketched in the Fig. 6.12 (a), ϕ_a was assumed to be the sum of the local potential of the electrode (ϕ_G) and the potential across the EDL (ϕ_D), i.e., $\phi_a = \phi_G + \phi_D$, while the bulk electrolyte was taken as a reference; the relationship between C_Q and C_D with ϕ_a was obtained through σ (recall that $C_Q/C_D \propto \sigma \propto \phi_G/\phi_D$). The predicted C_T - ϕ_a for pristine graphene is U-shaped, similar to its C_Q equivalent [inset Fig. 6.12 (b)], with a minimum near $0.5 \mu\text{F}/\text{cm}^2$ at $\phi_a = 0$ V. The C_T - ϕ_a curves for the N_1 and N_3V graphene systems also

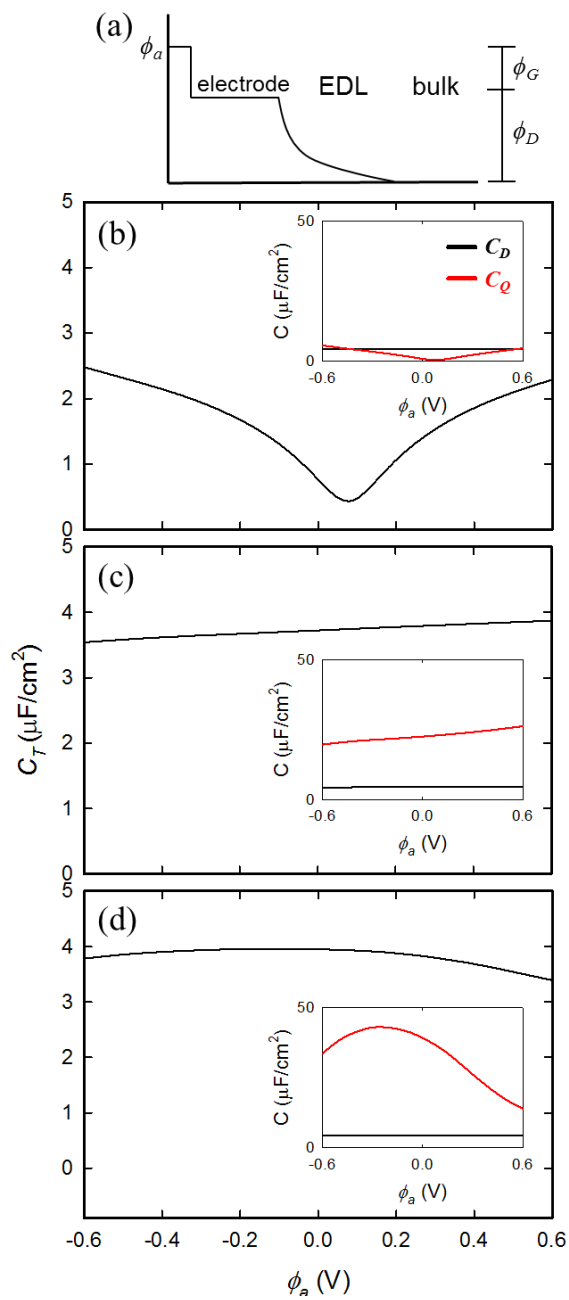


Figure 6.12 (a) Schematic of the idealized potential profile at the graphene/IL interface, and the total interfacial capacitance for (b) pristine, (b) N_1 , and (c) N_3V graphene systems as a function of applied potential (ϕ_a). The insets show relative contributions between C_D and C_Q as a function of ϕ_a .

closely resemble their C_Q equivalents [insets of Fig. 6.12 (c)-(d)]; recall that C_D is relatively flat when $|\phi_a| < 0.6$ V such that it has little impact on the shape of the profile. Both C_T profiles for the N-doped cases show enhanced capacitance in the range $|\phi_a| < 0.6$ V compared to the intrinsic case; it is apparent that this is due to the contribution from C_Q near $\phi_a = 0$ V. As mentioned above, this analysis only pertains to two ideal types of N-doped graphene and does not extend toward systems with mixed N-dopant types. Nonetheless, our study clearly highlights that the enhanced capacitance observed in N-doped supercapacitors can be attributed to increases in the electrode quantum capacitance.

6.3.4 Summary

We evaluated the influence of N doping on the interfacial capacitance for [BMIM][PF₆] ionic liquid (IL) and doped graphene using a combined density functional theory (DFT) and classical molecular dynamics (MD) method, with particular attention to the relative contributions of the quantum and double layer capacitance. We investigated two commonly observed N-configurations from experiments – substitutional N (N₁) and trimerized pyridine-type N (N_{3V}). According to our DFT calculations, both types of N-doping significantly enhanced the quantum capacitance of graphene near the Fermi level when compared to the undoped case; the N₁ graphene showed broad enhancement while N_{3V} graphene had sharp enhancement over a 0.4 V window. Our MD simulations for N₁ and N_{3V} graphene in [BMIM][PF₆] showed that the positively charged BMIM rings had a tendency to lie near the negatively charged N atoms. However, the N doping did not significantly perturb the microstructure of the double layer, which suggested that the

double layer capacitance was virtually unaffected at these doping concentrations. The resulting interfacial capacitance profiles closely resembled their quantum capacitance equivalents. It is evident that the enhanced capacitance observed in N-doped supercapacitors can be attributed to an increase in the electrode's quantum capacitance. This study suggests that other structural and/or chemical modifications to graphene may significantly enhance the interfacial capacitance and warrants further investigation.

Chapter 7: Graphene Adhesion on Amorphous Silica

7.1 Introduction

Due to its unique physical and chemical properties, graphene has received great attention for potential use in a wide range of applications.[145] In particular, graphene has been considered as a promising channel material for future electronic devices.[146] However, the electronic transport properties of graphene placed on an atomically rough substrate can be significantly influenced by its morphological corrugation which is dominated by the graphene-substrate adhesion.[147] Likewise, the adhesion between graphene and other materials may play an important role in determining the performance of many graphene-based devices, let alone their fabrications.

In recent years, several research groups have experimentally characterized graphene adhesion on the surface of amorphous silica ($a\text{-SiO}_2$) which is an important support material for graphene in various applications.[148-152] Earlier atomic force microscopy measurements[148,149] have shown evidence that a highly flexible graphene sheet can conform to the rough $a\text{-SiO}_2$ surface with high fidelity. While the conformal adhesion is thought to be driven mainly by the van der Waals (vdW) force between graphene and $a\text{-SiO}_2$ [148], previous estimates for the graphene/ SiO_2 adhesion energy are widely scattered. Ishigami *et al.* estimated the graphene/ SiO_2 interaction energy to be 0.6 eV/nm^2 based on the interlayer vdW interaction in graphite[148]. A similar value ($\approx 0.63 \text{ eV/nm}^2$) was predicted by Miwa *et al.* using density functional theory (DFT) calculations

with vdW interaction corrections.[153] On the other hand, the adhesion energy measured by Koenig *et al.* is substantially higher, 2.81 eV/nm² for monolayer graphene and 1.93 eV/nm² for multilayer (2-5 layers) graphene.[152] For comparison, experimentally the adhesion energies of graphene on polydimethylsiloxane and copper are reported to be 0.044 eV/nm² by Scharfenberg *et al.*[154] and 4.49 eV/nm² by Yoon *et al.*[155], respectively. It can be very challenging to precisely measure the adhesion strength of a single-atom-thick layer of carbon particularly on an amorphous solid surface using conventional experimental techniques. In addition, the high computational cost of DFT calculations makes them limited to small structural models; for instance, the surface area of *a*-SiO₂ samples employed in previous calculations[153,156,157] is around 1~2 nm², which can be insufficient to replicate properly the *a*-SiO₂ surface roughness and in turn the graphene/*a*-SiO₂ adhesion.

In this work, we evaluate the structure and adhesion energy of graphene on *a*-SiO₂ using force field calculations. The vdW interaction between graphene and *a*-SiO₂ is computed by employing three different sets of vdW parameters which were extracted from the Charmm and Dreiding force fields and by fitting to semiempirical dispersion corrected DFT calculations. Continuous Random Network model-based Metropolis Monte Carlo (CRN-MMC) simulations are performed to prepare defect-free *a*-SiO₂ surface models with various degrees of surface roughness; the *a*-SiO₂ surface structures are analyzed in terms of surface height distribution and Si/O spatial distribution. For different surface morphologies of *a*-SiO₂, we determine the topology of graphene that leads to the optimal adhesion on each *a*-SiO₂ surface; the graphene/*a*-SiO₂ interface

structure is used to estimate the adhesion energy (which is given in terms of the vdW interaction energy between graphene and *a*-SiO₂ and the strain energy of corrugated graphene on *a*-SiO₂). Finally we also look at the sensitivity of the adhesive strength to the change of morphological conformity between graphene and *a*-SiO₂.

7.2 Computational Methods

7.2.1 Graphene/SiO₂ Interface Structure Optimization

As illustrated in Fig. 7.1, we first constructed several defect-free *a*-SiO₂ slabs using continuous random network (CRN) model[158] based Metropolis Monte Carlo (CRN-MMC) simulations [(a) → (b)]. For each slab, 3600 SiO₂ units were placed in a supercell with lateral dimensions of 77.22Å × 77.22Å, yielding a slab thickness of about 20 Å. The top- and bottom-layer Si atoms were all passivated with O atoms, giving two defect-free surfaces. The highly strained initial structures were then relaxed via a sequence of bond transpositions using the MMC sampling based on energetics from Keating-like potentials for silica[159]. During the geometry relaxation of *a*-SiO₂ slab, periodic boundary conditions were employed in both *x* and *y* directions while the *z*-direction was released.

Then, two single graphene sheets were placed respectively on the bottom and top surfaces of the *a*-SiO₂ slab; the initial graphene/SiO₂ system was relaxed using molecular dynamics at 100K for 100 picoseconds, followed by static energy minimization using the conjugate gradient method until the total energy changes between iterations become less than 10⁻⁵ eV [(b) → (c) in Fig. 7.1]. To determine optimal adhesion condition,

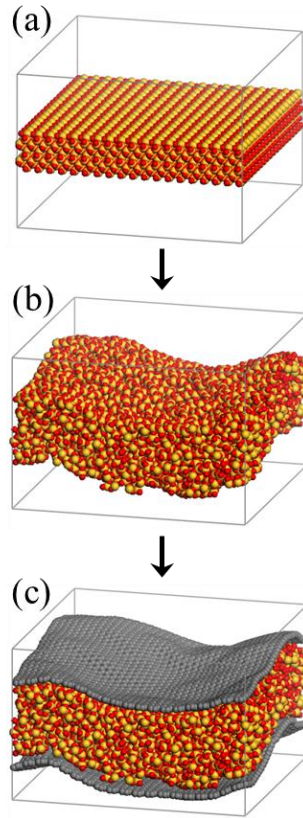


Figure 7.1 (a) Initial configuration of SiO_2 slab, (b) defect-free $a\text{-SiO}_2$ slab structure constructed using continuous random network model based Metropolis Monte Carlo (CRN-MMC) simulations, (c) relaxed graphene/ $a\text{-SiO}_2$ interface structure; two single graphene sheets are placed on the bottom and top surfaces of the $a\text{-SiO}_2$ slab.

different lateral dimensions of graphene sheets were taken into account. We used the AIREBO potential[160,161] for describing the structure and energetics of graphene, and refined the $a\text{-SiO}_2$ slab structure with the CHIK force field[162]. The 12-6 Lennard-Jones (LJ) potential was used to describe the van der Waals (vdW) interaction between $a\text{-SiO}_2$ and graphene. The MD and (static) energy minimization simulations were

performed using the Large-scale Atomic/Molecular Massively Parallel Simulator (LAMMPS) program[163].

7.2.2 Van der Waals Parameter Determination

The predicted graphene/SiO₂ adhesion strength can be strongly dependent on the choice of vdW parameters; therefore, caution is required in selecting them. we employed three different sets of LJ parameters (σ_i , ϵ_i). The parameters were extracted from the Charmm[164] and Dreiding[165] force fields, and also by fitting to the graphene/SiO₂ interaction energies from semi-empirical dispersion corrected density functional theory (DFT-D) calculations[166]; the parameter sets are hereafter referred to as LJ(Charmm), LJ(Dreiding), and LJ(DFT-D), respectively.

The LJ(DFT-D) parameters were obtained as follows. First, three *a*-SiO₂ slabs with 20 SiO₂ units each were constructed using combined CRN-MMC and DFT calculations[158], and then a graphene sheet was placed on top of each slab; the lateral dimensions of the *a*-SiO₂ slabs ($= 8.544 \times 7.399 \text{ \AA}^2$) were adjusted to match those of the 24-atom rectangular graphene supercell with a lattice constant of 2.466Å (calculated). The graphene/SiO₂ interaction energies were calculated by varying the graphene-SiO₂ distance using the DFT-D approach. With the DFT-D data, the optimal values for σ_i and ϵ_i were obtained through minimization of the cross-validation error (ξ);

$$\xi^2 = \frac{1}{N} \sum_{n=1}^N (E_{DFT-D}^{(n)} - E_{LJ}^{(n)})^2, \text{ where } E_{DFT-D}^{(n)} \text{ and } E_{LJ}^{(n)} \text{ refer to the DFT-D and LJ energies,}$$

respectively, of the n^{th} of N total data. Here, the ϵ_{Si}/ϵ_O ratio was fixed at 2 as used in

Table 7.1 12-6 Lennard-Jones (LJ) Parameters employed in this work.

| | ϵ (eV) | σ (Å) |
|---|------------------------------|----------------------------|
| | Charmm / Dreiding / DFT-D2 | Charmm / Dreiding / DFT-D2 |
| S | 0.01301 / 0.013443 / 0.00576 | 3.8264 / 3.8041 / 3.8230 |
| O | 0.00650 / 0.00415 / 0.00288 | 3.1181 / 3.0332 / 3.0669 |
| C | 0.00239 | 3.4121 |

LJ(Charmm). As listed in Table 7.1, the obtained ϵ_{Si} and ϵ_O values are substantially smaller than those in LJ(Charmm), while the σ values are close to each other. As such, as shown in Fig. 7.2, LJ(Charmm) and LJ(Dreiding) tend to overestimate the graphene/SiO₂ interaction energies compared to LJ(DFT-D) and DFT-D.

Our DFT calculations were performed within the Perdew-Burke-Ernzerhof (PBE) generalized gradient approximation[167] using the Vienna Ab initio Simulation Package (VASP)[168]. We employed the projector augmented wave (PAW) method to describe the interaction between core and valence electrons [169], and a planewave basis set with a kinetic energy cutoff of 400 eV. Periodic boundary conditions were employed in all three directions with a vacuum gap of 30 Å in the vertical (z) direction to separate the system from its periodic images. A (6×6×1) k -point grid in the scheme of Monkhorst-Pack[170] was used for the Brillouin zone sampling. We used the semi-empirical approach proposed by Grimme, also known as the DFT-D2 method[171], to take into account the vdW forces within DFT in determining the graphene/SiO₂ adhesion energy.

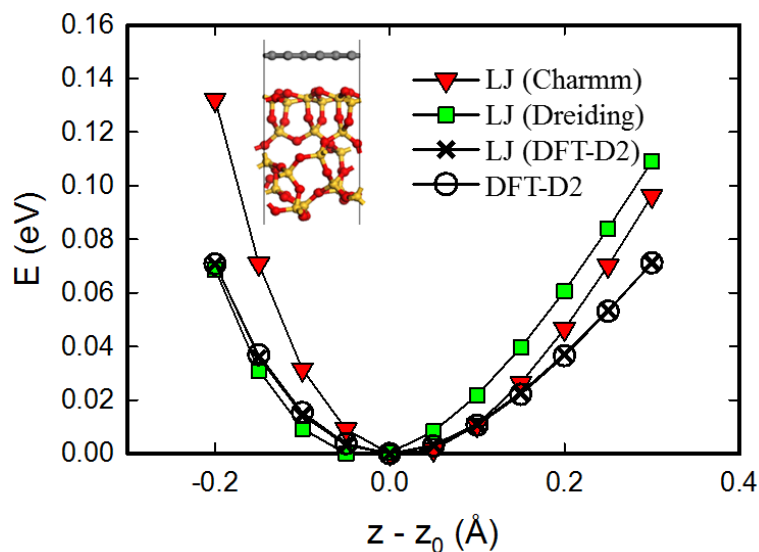


Figure 7.2 DFT-D2 values for the graphene/*a*-SiO₂ interaction energy used for LJ parameter optimization. The interaction energies from various force fields as indicated are also plotted for comparison purpose.

7.3 Results and Discussion

7.3.1 Surface Structure of Amorphous Silica

We first analyzed the atomic structure of 18 different *a*-SiO₂ model surfaces employed in this work; note that the vdW interaction of graphene with the underlying *a*-SiO₂ surface can be a function of surface density and composition. The surface Si and O atoms were chosen such that their surface-projected coordinates have no overlap with those of other atoms nearer the surface; the overlap radii of 2.511Å for Si and 2.252Å for O were selected based on the projection of the average Si-Si and O-O separations.

Table 7.2 Standard deviations of height distributions (σ) of graphene sheets and α -SiO₂ surfaces, graphene- α -SiO₂ distances (d_{Gr-SiO_2}) and van der Waals interaction energies (E_{vdW}), and graphene strain energy (E_{st}); 18 different α -SiO₂ model surfaces are considered. The values are calculated using LJ(DFT-D2) / LJ(Charmm) / LJ(Dreiding) parameter sets.

| α -SiO ₂ (Å) | St. Dev. (σ) | | $\langle d_{Gr-SiO_2} \rangle$ (Å) | E_{vdW} (eV/nm ²) | E_{st} (eV/nm ²) |
|-----------------------------------|-----------------------|--|---------------------------------------|------------------------------------|-----------------------------------|
| | Graphene (Å) | | | | |
| 1.95 | 1.88 / 1.80 / 1.81 | | 4.13 / 3.94 / 3.92 | 0.95 / 1.57 / 1.41 | 0.19 / 0.29 / 0.28 |
| 2.00 | 1.93 / 1.84 / 1.85 | | 4.16 / 3.96 / 3.99 | 0.97 / 1.60 / 1.40 | 0.21 / 0.30 / 0.25 |
| 2.26 | 2.18 / 2.11 / 2.08 | | 4.36 / 4.20 / 4.14 | 0.93 / 1.50 / 1.36 | 0.24 / 0.31 / 0.33 |
| 2.32 | 2.09 / 2.09 / 2.08 | | 4.17 / 3.99 / 4.00 | 0.94 / 1.55 / 1.37 | 0.18 / 0.27 / 0.23 |
| 2.53 | 2.29 / 2.27 / 2.26 | | 4.13 / 3.95 / 4.01 | 0.96 / 1.57 / 1.36 | 0.17 / 0.26 / 0.21 |
| 2.59 | 2.25 / 2.30 / 2.28 | | 4.32 / 4.07 / 4.10 | 0.92 / 1.56 / 1.37 | 0.25 / 0.38 / 0.34 |
| 2.63 | 2.31 / 2.24 / 2.22 | | 4.15 / 3.93 / 3.98 | 0.95 / 1.57 / 1.38 | 0.19 / 0.30 / 0.26 |
| 2.71 | 2.36 / 2.36 / 2.36 | | 4.21 / 3.98 / 4.09 | 0.94 / 1.57 / 1.34 | 0.23 / 0.35 / 0.27 |
| 2.77 | 2.19 / 2.21 / 2.22 | | 4.27 / 4.13 / 4.07 | 0.90 / 1.45 / 1.32 | 0.23 / 0.30 / 0.30 |
| 2.77 | 2.25 / 2.24 / 2.33 | | 4.00 / 3.71 / 4.05 | 1.00 / 1.67 / 1.35 | 0.21 / 0.34 / 0.16 |
| 3.21 | 2.47 / 2.51 / 2.50 | | 4.58 / 4.33 / 4.32 | 0.84 / 1.42 / 1.27 | 0.22 / 0.32 / 0.30 |
| 3.33 | 3.18 / 3.13 / 3.14 | | 4.21 / 3.98 / 3.97 | 0.99 / 1.64 / 1.46 | 0.44 / 0.56 / 0.52 |
| 3.46 | 3.20 / 3.21 / 3.21 | | 4.08 / 3.92 / 3.89 | 1.01 / 1.66 / 1.49 | 0.40 / 0.50 / 0.49 |
| 3.53 | 2.85 / 3.42 / 3.45 | | 5.03 / 4.16 / 4.10 | 0.76 / 1.60 / 1.44 | 0.14 / 0.48 / 0.49 |
| 3.53 | 3.30 / 3.26 / 3.28 | | 4.27 / 4.10 / 4.08 | 0.98 / 1.62 / 1.44 | 0.38 / 0.47 / 0.46 |
| 3.55 | 2.98 / 3.08 / 3.09 | | 4.34 / 4.06 / 4.19 | 0.87 / 1.48 / 1.25 | 0.19 / 0.31 / 0.23 |
| 3.61 | 2.99 / 3.04 / 3.09 | | 4.39 / 4.11 / 4.19 | 0.81 / 1.39 / 1.20 | 0.14 / 0.27 / 0.22 |
| 3.65 | 3.28 / 3.26 / 3.26 | | 4.21 / 3.97 / 3.96 | 1.00 / 1.67 / 1.48 | 0.43 / 0.55 / 0.52 |
| 2.91±0 | 2.55±0.47 | | 4.28±0.22 | 0.93±0.07 | 0.25±0.09 |
| .56 | / 2.57±0.53 | | / 4.03±0.13 | / 1.56±0.08 | / 0.36±0.10 |
| | / 2.58±0.53 | | / 4.06±0.10 | / 1.37±0.08 | / 0.32±0.11 |

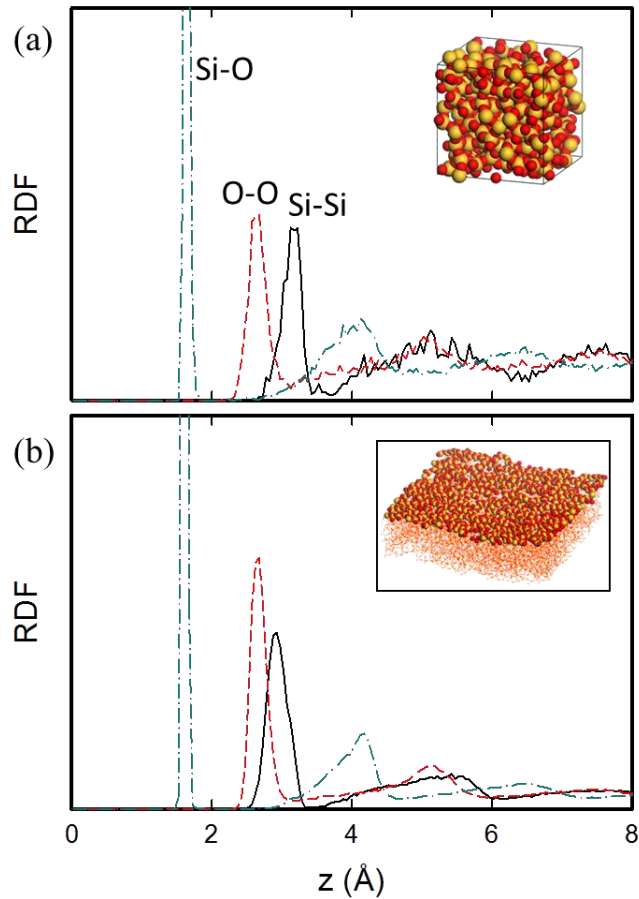


Figure 7.3 Radial distribution functions (RDF) for Si-Si, Si-O, and O-O pairs in *a*-SiO₂ bulk [(a)] and surface layer [(b)], as illustrated in the insets.

The defect-free *a*-SiO₂ surfaces mostly show Gaussian height distributions; as summarized in Table 7.2, the standard deviation (σ_{SiO_2}) varies from 1.95 to 3.65 Å with an average of 2.91 ± 0.56 Å. The surface roughness is in good agreement with existing experimental measurements (1.68-3.7 Å) [148-150,152]. In the surface layers, the number densities (per horizontal cross-sectional area) of Si and O atoms are estimated to be about $n_{\text{Si}} = 8.25 \pm 0.17 \text{ nm}^{-2}$ and $n_{\text{O}} = 10.92 \pm 0.25 \text{ nm}^{-2}$, yielding an Si:O ratio of

1:1.32; however, on average, O atoms are $0.62 \pm 0.06 \text{ \AA}$ more protruded than Si atoms from the $a\text{-SiO}_2$ surface.

Figure 7.3 shows the radial pair distribution functions for Si-Si, Si-O, and O-O in $a\text{-SiO}_2$ bulk [(a)] and surface layer [(b)]. For the bulk structure with a density of 2.26 g/cm^3 (Ref. 172), the calculated first peak positions of $1.63/2.63/3.13 \text{ \AA}$ for the Si-O/O-O/Si-Si pairs are close to the corresponding experimental data of $1.62/2.65/3.12 \text{ \AA}$ [173]. In the surface layers, we notice that the first peak position of Si-Si ($= 2.93 \text{ \AA}$) noticeably decreases in comparison to that ($= 3.13 \text{ \AA}$) in the bulk, which is apparently related to the relatively high Si density compared to the bulk counterpart; while there is no noticeable change in the Si-O and O-O peak positions.

7.3.2 Structure and Adhesion Strength at Graphene/SiO₂ Interface

The structure and adhesive strength of the interface between graphene and $a\text{-SiO}_2$ were calculated by varying the lateral dimension of graphene; special care was taken to ensure that the graphene sheet was conformally adhered to the rough surface of $a\text{-SiO}_2$. Once the optimal topology of graphene was determined, the graphene/SiO₂ adhesion energy was estimated using:

$$E_{ad} = -\frac{1}{A} (E_{Gr/SiO_2} - E_{SiO_2} - E_{Gr}), \quad (7.1)$$

where, E_{Gr/SiO_2} and E_{SiO_2} are the total energies of the graphene/ $a\text{-SiO}_2$ system and the $a\text{-SiO}_2$ slab, respectively, E_{Gr} is the energy of pristine graphene, and A is the $a\text{-SiO}_2$ slab cross-sectional area.

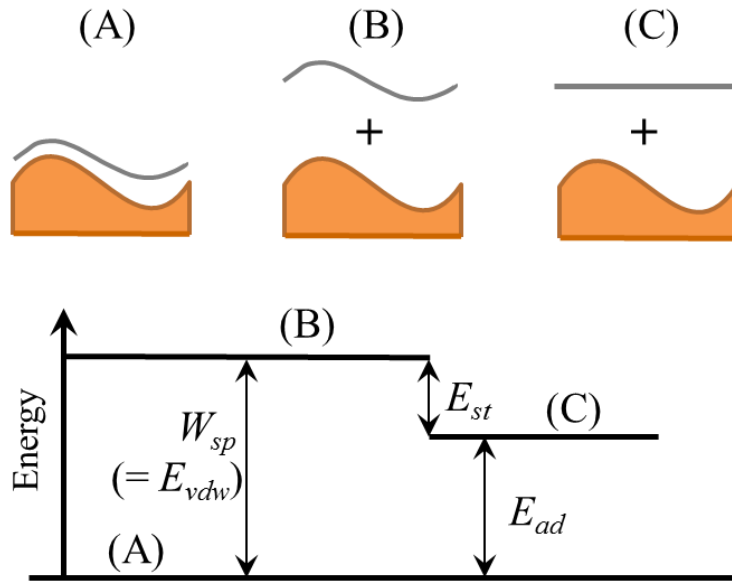


Figure 7.4 Energy diagram that describes separation of a graphene sheet from a rough surface. (A) graphene on a -SiO₂, (B) work of separation ($W_{sp} = E_{vdw}$) which is required to separate the graphene sheet, (C) adhesion energy (E_{ad}) which is obtained by taking into account the structural relaxation of graphene after separation.

The interface strength is also often characterized by the work of separation (W_{sp}) which represents the reversible work required to separate the interface into two free surfaces; that is, $W_{sp} = -(E_{Gr/SiO_2} - \dot{E}_{SiO_2} - \dot{E}_{Gr})/A$, where \dot{E}_{SiO_2} and \dot{E}_{Gr} refer to the total energies of the a -SiO₂ slab and the corrugated graphene sheet attached to the a -SiO₂, respectively, with no relaxation after separation. Note that E_{ad} differs from W_{sp} in that it takes full account of structural relaxation after separation, as illustrated in Fig. 7.4. In our calculations, the a -SiO₂ slab energy is found to merely change before and after the relaxation (i.e., $E_{SiO_2} \approx \dot{E}_{SiO_2}$) and the energy of corrugated graphene can be described in terms of its elastic strain energy (E_{st}). Therefore, for the graphene/SiO₂ interface, E_{ad} can

be approximated by W_{sp} minus E_{st} . In addition, given that the interfacial adhesion is entirely due to the vdW force, W_{sp} should be equal to the vdW interaction energy (E_{vdW}) such that E_{ad} is given in terms of $E_{vdW} - E_{st}$ (i.e., $E_{ad} = E_{vdW} - E_{st}$).

We evaluated the vdW interaction at the interface using three different sets of LJ parameters [LJ(DFT-D2), LJ(Charmm), LJ(Dreiding)] and the elastic strain of corrugated graphene with the AIREBO potential. From the 18 independent interface structures considered, the predicted E_{vdW} values vary from 0.93 ± 0.07 [LJ(DFT-D2)], 1.37 ± 0.08 [LJ(Dreiding)], to 1.56 ± 0.08 eV/nm² [LJ(Charmm)]. Since a stronger vdW interaction at the graphene/*a*-SiO₂ interface causes the graphene sheet to be more corrugated, the predicted E_{st} becomes largest ($= 0.36 \pm 0.10$ eV/nm²) with LJ(Charmm), followed by 0.32 ± 0.11 eV/nm² [LJ(Dreiding)] and 0.25 ± 0.09 eV/nm² [(DFT-D2)]. As a result, E_{ad} ($= E_{vdW} - E_{st}$) is predicted to be 0.68 (DFT-D2), 1.05 (Dreiding), and 1.20 eV/nm² (Charmm). Our results are overall in good agreements with 0.044 - 0.63 eV/nm² as predicted by previous theoretical or experimental studies [148,153,154]; although a very recent measurement based on a blister method suggested a much higher adhesion energy of about 2.81 eV/nm² [152].

As illustrated in Fig. 7.5, the height distribution comparison between graphene and SiO₂ clearly shows that the optimal graphene/*a*-SiO₂ adhesion commonly occurs when the graphene sheet is slightly less corrugated than the underlying *a*-SiO₂ surface, consistent with previous experiments[149,150]. For the 18 model interface systems

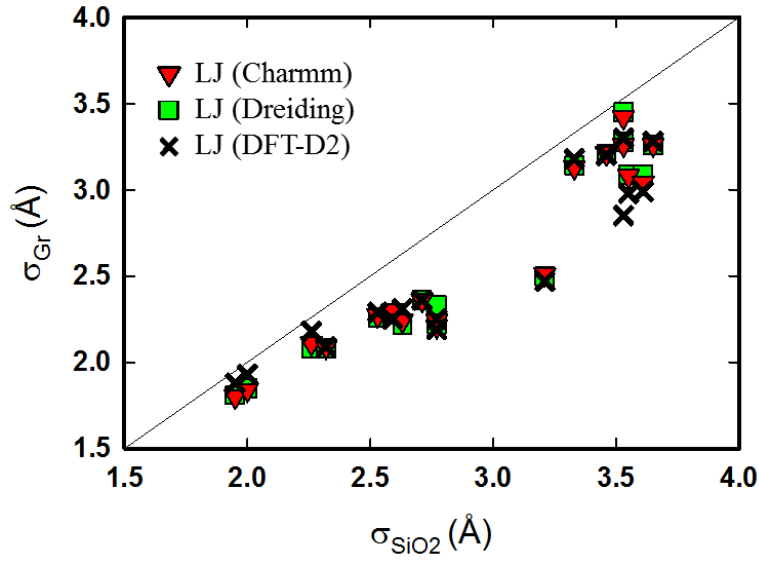


Figure 7.5 Predicted standard deviations of height distributions of graphene (σ_{Gr}) with respect to the a -SiO₂ surface (σ_{SiO_2}) for three parameter sets of LJ parameters employed.

considered, the predicted σ_{Gr} and σ_{SiO_2} with LJ(DFT-D2) are 2.55 ± 0.47 Å and 2.91 ± 0.56 Å, respectively, and the distance between graphene and a -SiO₂ is $d_{Gr-SiO_2} = 4.28 \pm 0.22$ Å. The average value of d_{Gr-SiO_2} decreases to 4.03/4.06 Å when using LJ(Charmm)/LJ(Dreiding), due to the increased vdW forces; however, the topological change of graphene appears to be insignificant with the choice of LJ parameter sets (i.e., σ_{Gr} only varies from 2.55 Å to 2.58 Å). It is also worth noting that there is an insignificant variance in d_{Gr-SiO_2} , although the surface roughness of a -SiO₂ varies significantly from sample to sample; this is apparently due to the fact that graphene is highly flexible and complies well with the morphological change of the underlying a -SiO₂ surface.

For comparison, we also estimated the E_{st} of corrugated graphene using[149]

$$E_{st} = \frac{C}{2} \left\{ \frac{1}{S} \int [\nabla^2 h(r)]^2 d^2r \right\}, \quad (7.2)$$

where, C is the bending rigidity of graphene, S is the integration domain area, and $h(r)$ is the local height of graphene at the spatial position r . As depicted in the inset of Fig. 7.7, a corrugated graphene sheet was mapped into a rectangular grid for the integration with a careful selection of optimal grid size. For the same graphene topologies as obtained with AIREBO/DFT-D2 (*vide supra*), E_{st} is predicted to be 0.17-0.30 eV/nm² for a typical range of $C = 0.85$ -1.5 eV [174-176], which is in good agreement with $E_{st} = 0.25 \pm 0.09$ eV/nm² as estimated with the AIREBO potential. Our calculations clearly demonstrate that the E_{vdW} between graphene and α -SiO₂ can be substantially greater than the E_{st} associated with the resulting corrugation of graphene, permitting high-fidelity topological conformation of graphene to the rough surface of α -SiO₂.

7.3.3 Morphological conformity effect

Next, we turned to examining how the adhesive strength is affected by the morphological conformity between graphene and α -SiO₂. Figure 7.6 shows the variations of E_{vdW} and d_{Gr-SiO_2} with σ_{Gr} (which can be used as a measure of the extent of graphene corrugation); a smaller (larger) value of σ_{Gr} indicates that the graphene sheet is less (more) corrugated as shown in the upper panels [(A)-(C)]. In this case, the optimal adhesion is achieved when the graphene sheet is slightly less corrugated ($\sigma_{Gr} = 3.28$ Å) than the underlying α -SiO₂ surface ($\sigma_{SiO_2} = 3.65$ Å, indicated as the dashed line). The calculation

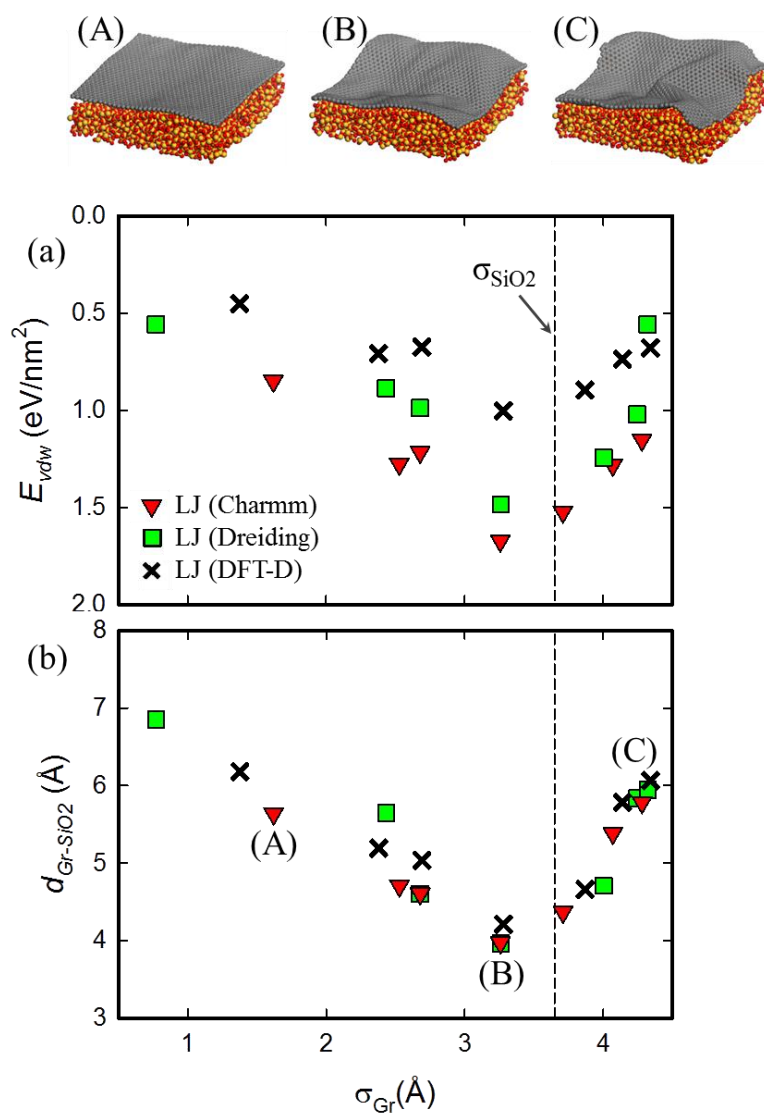


Figure 7.6 Variations in the graphene/*a*-SiO₂ vdW interaction energy (E_{vdW}) and distance (d_{Gr-SiO_2}) for the selected *a*-SiO₂ surface with $\sigma_{SiO_2}=3.65\text{\AA}$ and various morphologies of graphene. Selected graphene/*a*-SiO₂ interface structures [(A)-(C) as indicated in (b)] are shown in the upper panels.

results clearly show that E_{vdW} drops rapidly as σ_{Gr} increases or decreases relative to the optimal case ($\sigma_{Gr} = 3.28 \text{ \AA}$); the reduced vdW interaction is apparently attributed to the decreased graphene/*a*-SiO₂ contact area. Likewise, d_{Gr-SiO_2} is found to increase as the graphene sheet adheres less conformally to the *a*-SiO₂ surface.

We also performed Fast Fourier Transform (FFT) analysis to evaluate the degree of the topological conformity of graphene to *a*-SiO₂ for various σ_{Gr} . When $\sigma_{Gr} = 3.65 \text{ \AA}$ (optimal adhesion), as shown in Fig. 7.7 [(a)], the Fourier amplitudes of graphene and *a*-SiO₂ are nearly identical when the wave length (λ) is greater than 2 nm. However, for $\lambda < 2 \text{ nm}$, we can see a noticeable discrepancy between the graphene and *a*-SiO₂ spectra, implying that the graphene sheet may not conform well to the relatively small jagged features of the *a*-SiO₂ surface. The three-dimensional (3-D) mesh surface plots (insets) of graphene and *a*-SiO₂ also clearly demonstrate that graphene replicates well the surface topology of *a*-SiO₂, except the rough localized features with small curvatures. This implies that the energy cost for conforming to the very bumpy features may exceed the energy gain from the consequently increased graphene/*a*-SiO₂ contact area. A back-of-the-envelope calculation based on Hook's law also suggests that graphene may hardly conform to rough surfaces (which have radii of curvature less than 1.0-1.3nm[177]).

If the graphene sheet is much less [(b)] or more [(c)] corrugated than the *a*-SiO₂ surface, as expected, there are significant discrepancies in the Fourier amplitudes over almost the entire range of wavelengths. At $\sigma_{Gr} = 1.62 \text{ \AA}$ [(b)], the graphene amplitude is consistently lower than the *a*-SiO₂ case, indicating that the graphene sheet remains relatively flat. On the other hand, when $\sigma_{Gr} = 4.28 \text{ \AA}$ [(c)], above 2 nm (in λ), the

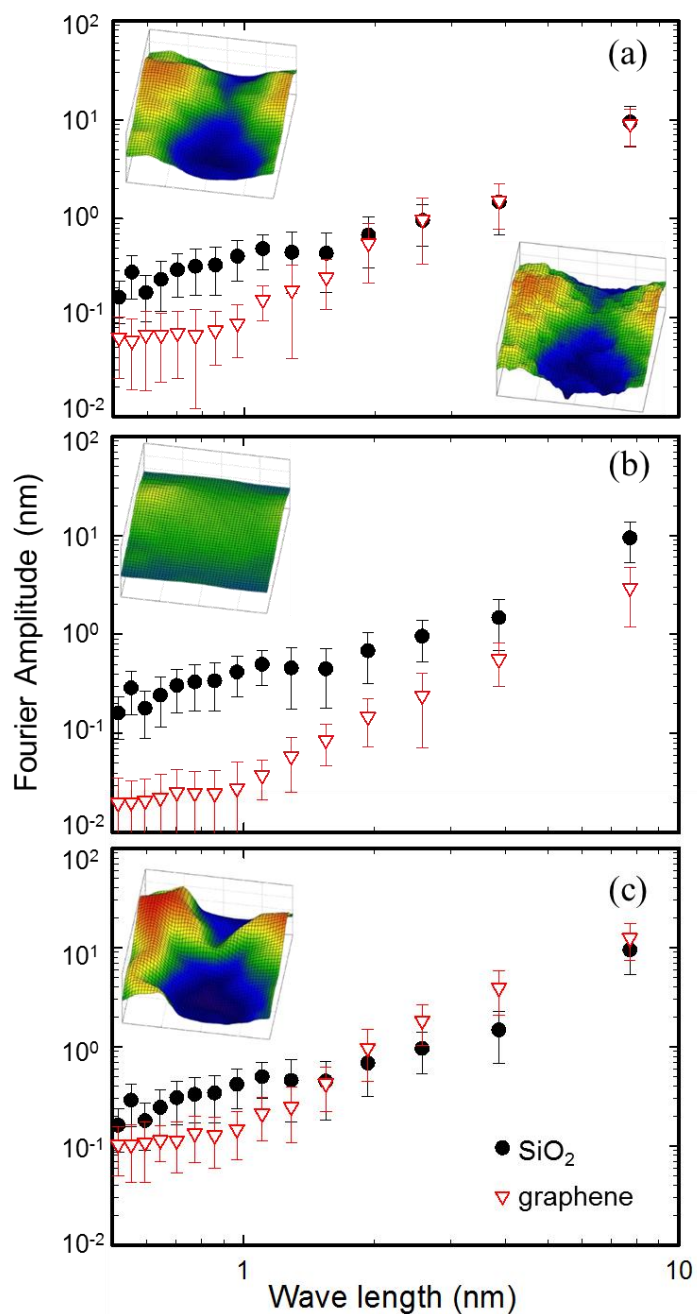


Figure 7.7 Fast Fourier Transform-based morphological analysis of graphene and *a*- SiO_2 surface for three different adhesion conditions; (a) optimal, (b) less corrugated, and (c) more corrugated. Corresponding surface contour plots are also shown as insets.

amplitude of graphene gets larger than that of a -SiO₂, which is apparently due to the more corrugated graphene; however, still the a -SiO₂ surface tends to contain relatively more small/localized roughness features ($\lambda < 2\text{nm}$). For both cases [(b) and (c)], compared to the optical adhesion case [(a)], E_{ad} significantly decreases while d_{Gr-SiO_2} increases because of the reduced graphene/ a -SiO₂ vdW interaction.

7.4 Summary

We performed a computational analysis of the morphology and adhesion strength of graphene on a -SiO₂. The a -SiO₂ surface was modeled with thin-layer slabs each of which provides two surfaces; 18 model surfaces with different degrees of surface roughness were considered. The defect-free a -SiO₂ slabs were constructed using CRN-MMC simulations; they were found to mostly show Gaussian height distributions with an average standard deviation of $2.91 \pm 0.56 \text{ \AA}$, in good agreement with existing experimental measurements (1.68-3.7 \AA). In the surface layers, the number densities (per horizontal cross-sectional area) of Si and O atoms are predicted to be about $n_{\text{Si}} = 8.25 \pm 0.17 \text{ nm}^{-2}$ and $n_{\text{O}} = 10.92 \pm 0.25 \text{ nm}^{-2}$, while on average O atoms are $0.62 \pm 0.06 \text{ \AA}$ more protruded than Si atoms from the a -SiO₂ surface.

Our calculations clearly demonstrate that the optimal graphene/ a -SiO₂ adhesion occurs when the graphene sheet is slightly less corrugated than the underlying a -SiO₂ surface, consistent with previous experiments. The vdW interaction energy at the interface was predicted to vary from 0.93 ± 0.07 [LJ(DFT-D2)], 1.37 ± 0.08 [LJ(Dreiding)], to $1.56 \pm 0.08 \text{ eV/nm}^2$ [LJ(Charmm)], depending on the choice of LJ

parameters as indicated. A stronger vdW interaction at the graphene/*a*-SiO₂ interface causes the graphene sheet to be more corrugated; hence, the predicted E_{st} turns out to be largest ($= 0.36 \pm 0.10$ eV/nm²) with LJ(Charmm), followed by 0.32 ± 0.11 eV/nm² [LJ(Dreiding)] and 0.25 ± 0.09 eV/nm² [(DFT-D2)], yielding the graphene adhesion energy of E_{ad} ($= E_{vdW} - E_{st}$) = 0.68 (DFT-D2), 1.05 (Dreiding), and 1.20 eV/nm² (Charmm). Finally, our Fast Fourier Transform analysis shows a noticeable discrepancy between the graphene and *a*-SiO₂ spectra when the wave length is smaller than 2 nm, suggesting that the graphene sheet may not conform well to the relatively small jagged features of the *a*-SiO₂ surface.

Chapter 8: Summary

The main objective of this dissertation is to investigate the interfacial properties of graphene with ionic liquids (ILs) and amorphous silica ($a\text{-SiO}_2$) using first principles-based atomistic simulations. The first part of this dissertation focuses on studying the microstructure of various ILs including [BMIM][PF₆], [BMIM][TFSI], and [BMIM][Cl] near graphene electrodes at various charge densities. This study provides a molecular description of electric double layers (EDLs) such as ion packing and orientation, cation-anion segregation, and electrode charge screening.

Although the IL interfacial structures exhibit an alternative cation/anion layering extending a few nanometers, calculated potential profiles provide evidence of one-ion thick compact EDL formation. We then present the interfacial capacitance between planar graphene and [BMIM][PF₆] IL, with particular attention to the relative contributions of the EDL capacitance at the graphene/IL interface and the quantum capacitance of graphene. The capacitance-potential curve of the EDL is convex- or bell-shaped, whereas the quantum capacitance of graphene is found to have concave- or U-shaped characteristics with a minimum of nearly zero. Consequently, we find that the total interfacial capacitance exhibits a U-shaped trend, consistent with existing experimental observations at a typical carbon/IL interface. Our work highlights the importance of the quantum capacitance in the overall performance of graphene-based EDL capacitors.

The influence of N doping on the total capacitance is also investigated. We study two types of N-doped (substitutional and trimerized pyridine-type N) graphene (at a 2.7% doping level) in [BMIM][PF₆] IL. Our DFT calculations show both types of N-doping significantly enhance the quantum capacitance of graphene as a result of electronic structure modifications compared to the undoped graphene. MD simulations show N doping insignificantly perturbs the EDL microstructure, thus the EDL capacitance is virtually unaffected by N doping at moderate N concentrations considered. Consequently, we think that the resulting enhanced interfacial capacitance is mainly attributed to an increase in the electrode's quantum capacitance.

We also perform a computational analysis of the morphology and adhesion strength of graphene on *a*-SiO₂. The *a*-SiO₂ model surfaces constructed using CRN-MMC simulations mostly show Gaussian height distributions with an average standard deviation of 2.91 ± 0.56 Å, in good agreement with existing experimental measurements (1.68-3.7 Å). Our calculations clearly demonstrate that the optimal graphene/*a*-SiO₂ adhesion occurs when the graphene sheet is slightly less corrugated than the underlying *a*-SiO₂ surface, consistent with previous experiments. We also find from Fast Fourier Transform-based morphology analysis that the graphene sheet may not conform well to the relatively small jagged features of the *a*-SiO₂ surface (with wave lengths of smaller than 2 nm). The vdW interaction energy at the interface was predicted to vary from 0.93 to 1.56 eV/nm², depending on the choice of LJ parameters.

Bibliography

1. P. R. Wallace, *Phys. Rev.*, **71**, 476 (1947)
2. K. S. Novoselov, A. K. Geim, S. V. Morozov, D. Jiang, Y. Zhang, S. V. Dubonos, I. V. Grigorieva, and A. A. Firsov, *Science*, **306**, 666 (2004)
3. DOE Energy in the United States. from <http://www.eia.doe.gov/emeu/aer/eh/total.html> (2000)
4. DOE Energy in the United States. from <http://www.eia.doe.gov/oiaf/forecasting.html> (2008)
5. J. Goodenough, in Report of the basic energy sciences workshop on electrical energy storage (2007)
6. B. E. Conway, *Electrochemical supercapacitors: scientific fundamentals and technological applications*. Kluwar, 1999
7. P. Simon, Y. Gogotsi, *Nature Materials.*, **7**, 845 (2008)
8. R. D. Rogers, K. R. Seddon, *Science*, **302**, 792 (2003)
9. W. Xu, C. A. Angell, *Science*, **302**, 422 (2003)
10. I. Krossing, and J. M. Slattery, *J. Phys. Chem.*, **220**, 1343 (2006)
11. M. D. Stoller, C. W. Magnuson, Y. Zhu, S. Murali, J. W. Suk, R. Piner, R. S. Ruoff, *Energy Environ. Sci.* **4**, 4685 (2011)
12. A. J. Bard and L. R. Faulkner, *Electrochemical Methods: Fundamentals and Applications*, 2nd ed., p. 12-13, Wiley Interscience, New York, 2000
13. G. Gouy, *J. Phys. Radium*, **9**, 457 (1910); G. Gouy, *Compt. Rend.*, **149**, 654 (1910); D. L. Chapman, *Phil. Mag.*, **25**, 475 (1913); O. Stern, *Z. Elektrochem.*, **30**, 508 (1924)
14. M. M. Islam, M. T. Alam, T. Ohsaka, *J. Phys. Chem. C*, **112**, 16568 (2008)
15. M. M. Islam, M. T. Alam, T. Okajima, T. Ohsaka, *J. Phys. Chem. C*, **113**, 3386 (2009)

16. B. J. Alder, T. E. Wainwright, *J. Chem. Phys.*, **27**, 1208 (1957)
17. B. J. Alder, T. E. Wainwright, *J. Chem. Phys.*, **31**, 459 (1959)
18. F. H. Stillinger, A. Rahman, *J. Chem. Phys.*, **60**, 1545 (1974)
19. L. Verlet, *Phys. Rev.*, **95**, 159 (1967)
20. E. R. Cruz-Chu, A. Aksimentiev, K. Schulten, *J. Phys. Chem. B*, **110**, 21497 (2006)
21. J. Wang, W. Wang, P. A. Kollman, D. A. Case, *J. Mol. Graphics Modell.*, **25**, 247260 (2006)
22. J. Wang, R. M. Wolf, J. W. Caldwell, P. A. Kollman, D. A. Case, *J. Comp. Chem.*, **25**, 1157 (2004)
23. W. L. Jorgensen, D. S. Maxwell, J. Tirado-Rives, *J. Am. Chem. Soc.*, **118**, 11225 (1996)
24. G. Kaminski, W. L. Jorgensen, *J. Phys. Chem.*, **100**, 18010 (1996)
25. V. Perebeinos, J. Tersoff, *Phys. Rev. B*, **79**, 241409 (2009)
26. R. C. Haddon, *J. Am. Chem. Soc.*, **112**, 3385 (1990); R. C. Haddon, *Acc. Chem. Res.*, **21**, 243 (1988)
27. R. C. Haddon, L. E. Brus, K. Raghavachari, *Chem. Phys. Lett.*, **125**, 459 (1986); R. C. Haddon, L. E. Brus, K. Raghavachari, *ibid.* **131**, 165 (1986); R. C. Haddon, *J. Am. Chem. Soc.*, **108**, 2837 (1986)
28. M. A. Hamon, M. E. Itkis, S. Niyogi, T. Alvaraez, C. Kuper, M. Menon, R. C. Haddon, *J. Am. Chem. Soc.*, **123**, 11292 (2001)
29. F. Wooten, K. Winer, D. Weaire, *Phys. Rev. Lett.*, **54**, 1392 (1985)
30. E. Polak, *Computational Methods in Optimization*, Academic, New York, 1971
31. C. P. Ewels, M. I. Heggie, P. R. Briddon, *Chem. Phys. Lett.*, **351**, 178 (2002)
32. L. Li, S. Reich, J. Robertson, *Phys. Rev. B*, **72**, 184109 (2005)

33. J. Kotakoski, A. V. Krashennnikov, U. Kaiser, J. C. Meyer, *Phys. Rev. Lett.*, **106**, 105505 (2011)
34. P. Hohenberg, W. Kohn, *Phys. Rev.*, **136**, B864 (1964)
35. W. Kohn, L. J. Sham, *Phys. Rev.*, **140**, A1133 (1965)
36. X. Wu, M. C. Vargas, S. Nayak, V. Lotrich, G. Scoles, *J. Chem. Phys.*, **115**, 8748 (2001)
37. R. D. Rogers, K. R. Seddon, *Science*, **302**, 792 (2003)
38. W. Xu, C. A. Angell, *Science*, **302**, 422 (2003)
39. I. Krossing, J. M. Slattery, *J. Phys. Chem.*, **220**, 1343 (2006)
40. R. D. Rogers, G. A. Voth, *Acc. Chem. Res.*, **40**, 1077 (2007)
41. A. Lewandowski, M. Galinski, *J. Phys. Chem. Solids*, **65**, 281 (2004)
42. S. Baldelli, *Acc. Chem. Res.*, **41**, 421 (2008)
43. M. Mezger, H. Schroder, H. Reichert, S. Schramm, J. S. Okasinski, S. Schroder, V. Honkimaki, M. Deutsch, E. M. Ocko, J. Ralston, M. Rohwerder and M. Stratmann, *Science*, **322**, 424 (2008)
44. R. Atkin, G. G. Warr, *J. Phys. Chem. C*, **111**, 5162 (2007)
45. J. Vatamanu, O. Borodin, G. D. Smith, *J. Phys. Chem. B*, **115**, 3073 (2011)
46. M. Bazant, B. Storey, A. A. Kornyshev, *Phys. Rev. Lett.*, **106**, 046102 (2011)
47. R. Hayes, G. G. Warr, R. Atkin, *Phys. Chem. Chem. Phys.*, **12**, 1709 (2010)
48. A. J. Bard and L. R. Faulkner, *Electrochemical Methods: Fundamentals and Applications*, 2nd ed., p. 551, Wiley Interscience, New York, 2000
49. W. L. Jorgensen, D. S. Maxwell, J. Tirado-Rives, *J. Am. Chem. Soc.*, **118**, 11225 (1996).
50. G. Kaminski, W. L. Jorgensen, *J. Phys. Chem.*, **100**, 18010 (1996)
51. J. N. C. Lopes, J. Deschamps, A. A. H. Pádua, *J. Phys. Chem. B*, **108**, 2038 (2004)

52. J. N. C. Lopes, J. Deschamps, A. A. H. Pádua, *J. Phys. Chem. B*, **108**, 11250 (2004)
53. O. Borodin, G. D. Smith, R. L. Jaffe, *J. Comput. Chem.*, **22**, 641 (2001)
54. L. Battezzatti, C. Pisani, F. Ricca, *J. Chem. Soc.*, **71**, 1629 (1975)
55. J. Kumelan, A. P.-S. Kamps, D. Tuma, G. Maurer, *Fluid Phase Equilib.*, **207**, 228 (2005)
56. S. Maolin, Z. Fuchun, W. Guozhong, F. Haiping, W. Chunlei, C. Shimou, Z. Yi, H. Jun, *J. Chem. Phys.*, **128**, 134504 (2008)
57. S. A. Kislenko, I. S. Samoylov, R. H. Amirov, *Phys. Chem. Chem. Phys.*, **11**, 5584 (2009)
58. L. Verlet, *Phys. Rev.*, **95**, 159 (1967)
59. W. Hoover, *Phys. Rev. A*, **31**, 1695 (1985)
60. J. Ryckaert, G. Ciccotti, H. J. C. Berendsen, *J. Comput. Phys.*, **23**, 327 (1977)
61. R. W. Hockney, J. W. Eastwood, *Computer Simulation Using Particles*, Adam Hilger, New York, 1989
62. I. Yeh, M. L. Berkowitz, *J. Chem. Phys.*, **111**, 3155 (1999)
63. S. J. Plimpton, *J. Comput. Phys.*, **117**, 1 (1995)
64. S. Wang, S. Li, Z. Cao, T. Yan, *J. Phys. Chem. C*, **114**, 990 (2010)
65. B. L. Bhargava, S. Balasubramanian, *J. Am. Chem. Soc.* **128**, 10073 (2006)
66. R. M. Lynden-Bell, M. Del Pópolo, *Phys. Chem. Chem. Phys.*, **8**, 949 (2006)
67. Y. Liu, Y. Zhang, G. Wu, J. Hu, *J. Am. Chem. Soc.*, **128**, 7456 (2006)
68. S. Bovio, A. Podesta, C. Lenardi, P. Milani, *J. Phys. Chem. B*, **113**, 6600 (2009).
69. The charge was calculated by numerically integrating the charge density over the length of the first layer. We defined the bounds of the layer as the two first z -positions where the total charge density = 0 coincided with the counterion number density = 0.

70. C. Pinilla, M. G. Del Pópolo, J. Kohanoff, R. M. Lynden-Bell, *J. Phys. Chem. B*, **111**, 4877 (2007)
71. F. Tao, S. L. Bernasek, *J. Am. Chem. Soc.*, **127**, 12750 (2005)
72. The probability is equivalent to the normalized histogram of orientations. A bin size of 2° was used.
73. S. Rivera-Rubero, S. Baldelli, *J. Phys. Chem. B*, **118**, 15133 (2004)
74. C. Aliaga, S. Baldelli, *J. Phys. Chem. B*, **110**, 18481 (2006)
75. Y.-Z. Su, Y.-C. Fu, J.-W. Yan, Z.-B. Chen, B.-W. Mao, *Angew. Chem. Int. Ed.*, **48**, 5148 (2009)
76. M. T. Alam, J. Masud, M. Islam, T. Okajima, T. Ohsaka, *J. Phys. Chem. C*, **115**, 19797 (2011)
77. M. T. Alam, M. Islam, T. Okajima, T. Ohsaka, *J. Phys. Chem. C*, **112**, 16600 (2008)
78. V. Lockett, M. Horne, R. Sedev, *Phys. Chem. Chem. Phys.*, **12**, 12499 (2010)
79. A. A. Kornyshev, *J. Phys. Chem. B*, **111**, 5545 (2007)
80. J. Vatamanu, O. Borodin, G. D. Smith, *J. Am. Chem. Soc.*, **132**, 14825 (2010)
81. G. Feng, J. S. Zhang, R. J. Qiao, *J. Phys. Chem. C*, **113**, 4549 (2009)
82. G. Feng, R. Qiao, J. Huang, S. Dai, B.G. Sumpter, V. Meunier. *Phys. Chem. Chem. Phys.*, **13**, 1152 (2011)
83. M. V. Fedorov, N. Georgi, A. A. Kornyshev, *Electrochem. Commun.*, **12**, 296 (2010)
84. N. Georgi, A. A. Kornyshev, M. V. Fedorov, *J. Electroanal. Chem.*, **649**, 261 (2010)
85. Y. Lauw, M. D. Horne, T. Rodopoulos, F. A. M. Leermakers, *Phys. Rev. Lett.*, **103**, 117801 (2009)
86. Y. Lauw, M. D. Horne, T. Rodopoulos, A. Nelson, F. A. M. Leermakers, *J. Phys. Chem. B*, **114**, 11149 (2010)

87. Y. Shim, H. J. Kim, *ACS Nano*, **4**, 2345 (2010)
88. J. Vatamanu, L. Cao, O. Borodin, D. Bedrov, G. D. Smith, *J. Phys. Chem. Lett.*, **2**, 2267 (2011)
89. C. Merlet, B. Rotenberg, P. A. Madden, P.-L. Taberna, P. Simon, Y. Gogotsi, M. Salanne, *Nat. Mater.*, **11**, 1 (2012)
90. G. Feng, D. Jiang, P. T. Cummings, *J. Chem. Theory Comput.*, **8**, 1058 (2012)
91. H. M. Jeong, J. W. Lee, W. H. Shin, Y. J. Choi, H. J. Shin, J. K. Kang, J. W. Choi, *Nano. Lett.*, **11**, 2472 (2011)
92. D.-W. Wang, F. Li, Z.-G. Chen, G. Q. Lu, H.-M. Cheng, *Chem. Mater.*, **20**, 7195 (2008)
93. E. Frackowiak, F. Béguin, *Carbon*, **39**, 937 (2001)
94. J.-P. Randin, E. Yeager, *J. Electrochem. Soc.*, **118**, 711 (1971)
95. J. Xia, F. Chen, J. Li, N. Tao, *Nat. Nanotech.*, **4**, 505 (2009)
96. M. Islam, M. T. Alam, T. Okajima, T. Ohsaka, *J. Phys. Chem. C*, **113**, 3386 (2009)
97. H. Gerischer, *J. Phys. Chem.*, **89**, 4249 (1985)
98. H. Gerischer, R. McIntyre, D. Scherson, W. Storck, *J. Phys. Chem.*, **91**, 1930 (1987)
99. S. Luryi, *Appl. Phys. Lett.*, **52**, 501 (1988)
100. J. P. Perdew, Y. Wang, *Phys. Rev. B*, **45**, 13244 (1992)
101. G. Kresse, J. Furthmuller, *VASP the Guide*, Vienna University of Technology, Vienna (2001)
102. P. E. Blöchl, *Phys. Rev. B*, **50**, 17953 (1994)
103. H. J. Monkhorst, J. D. Pack, *Phys. Rev. B*, **13**, 5188 (1976)
104. V. Lockett, R. Sedev, J. Ralston, M. Horne, T. Rodopoulos, *J. Phys. Chem. B*, **112**, 7486 (2008)

105. The line connecting the unfilled circles was drawn by smoothing the original data points. We used a negative exponential smoothing technique embedded in SigmaPlot 12.0 to give 200 points after smoothing – the spacing between each point was 0.11 V. We then obtained the C_D at any given ϕ by numerically calculating the central difference at each point, i.e.,
- $$C_{d,i} = (\sigma_{i-2} - 8\sigma_{i-1} + 8\sigma_{i+1} - \sigma_{i+2}) / 12\Delta\phi.$$
106. M. Islam, M. T. Alam, T. Ohsaka, *J. Phys. Chem. C*, **112**, 16568 (2008)
107. D. L. John, L. C. Castro, D. L. Pulfrey, *J. Appl. Phys.*, **96**, 5180 (2004)
108. T. Fang, A. Konar, H. Xing, D. Jena, *Appl. Phys. Lett.*, **91**, 092109 (2007)
109. A. K. Geim, K. S. Novoselov, *Nature*, **6**, 183 (2007)
110. P. Wallace, *Phys. Rev.*, **329**, 622 (1947)
111. F. Giannazzo, S. Sonde, V. Raineri, E. Rimini, *Nano Lett.*, **9**, 23 (2009)
112. S. Droscher, P. Roulleau, F. Molitor, P. Studerus, C. Stampfer, T. Ihn, K. Ensslin, *Appl. Phys. Lett.*, **96**, 152104 (2010)
113. L. Ponomarenko, R. Yang, R. Gorbachev, *Phys. Rev. Lett.*, **105**, 136801 (2010)
114. G. Wang, L. Zhang, J. Zhang, *Chem. Soc. Rev.*, **41**, 797 (2012)
115. Conway, B. E. *Electrochemical Supercapacitors: Scientific Fundamentals and Technological Applications*; Kluwar Academic: New York, NY, 1999
116. R. D. Rogers, K. R. Seddon, *Science*, **302**, 792 (2003)
117. W. Xu, C. A. Angell, *Science*, **302**, 422 (2003)
118. P. Simon, Y. Gogotsi, *Nat. Mater.*, **7**, 845 (2008)
119. A. Lewandowski, M. Galinski, *J. Phys. Chem. Solids*, **65**, 281 (2004)
120. H. M. Jeong, J. W. Lee, W. H. Shin, Y. J. Choi, H. J. Shin, J. K. Kang, J. W. Choi, *Nano Lett.*, **11**, 2472 (2011)
121. B. Jiang, C. Tian, L. Wang, L. Sun, C. Chen, X. Nong, Y. Qiao, H. Fu, *Appl. Surf. Sci.*, **258**, 3438 (2012)

122. Y. Qiu, X. Zhang, S. Yang, *Phys. Chem. Chem. Phys.*, **13**, 12554 (2011)
123. L. Sun, L. Wang, C. Tian, T. Tan, Y. Xie, K. Shi, M. Li, H. Fu, *RSC Advances*, **2**, 4498 (2012)
124. J. Xia, F. Chen, J. Li, N. Tao, *Nat. Nanotechnol.*, **4**, 505 (2009)
125. M. D. Stoller, C. W. Magnuson, Y. Zhu, S. Murali, J. W. Suk, R. Piner, R. S. Ruoff, *Energ. Environ. Sci.*, **4**, 4685 (2011)
126. E. Paek, A. J. Pak, G. S. Hwang, *J. Electrochem. Soc.*, **160**, A1–A10 (2013)
127. S. Luryi, *Appl. Phys. Lett.*, **52**, 501 (1988)
128. L. Zhao, R. He, K. T. Rim, T. Schiros, K. S. Kim, H. Zhou, C. Gutiérrez, S. P. Chockalingham, C. J. Arguello, L. Pálová, L., *Science*, **333**, 999 (2011)
129. J. P. Perdew, Y. Wang, *Phys. Rev. B*, **45**, 13244 (1992)
130. G. Kresse, J. Furthmüller, *Phys. Rev. B*, **54**, 11169 (1996)
131. P. E. Blöchl, *Phys. Rev. B*, **50**, 17953 (1994)
132. Y. Fujimoto, S. Saito, *Phys. Rev. B*, **84**, 245446 (2011)
133. W. L. Jorgensen, D. S. Maxwell, J. Tirado-Rives, *J. Am. Chem. Soc.*, **118**, 11225 (1996)
134. G. Kaminski, W. L. Jorgensen, *J. Phys. Chem.*, **100**, 18010 (1996)
135. W. Hoover, *Phys. Rev. A*, **31**, 1695 (1985)
136. S. J. Plimpton, *J. Comput. Phys.*, **117**, 1 (1995)
137. D. L. John, L. C. Castro, D. L. Pulfrey, *J. Appl. Phys.*, **96**, 5180 (2004)
138. M. Mezger, H. Schröder, H. Reichert, S. Schramm, J. S. Okasinski, S. Schöder, V. Honkimäki, M. Deutsch, B. M. Ocko, J. Ralston, *Science*, **322**, 424 (2008)
139. Y. Liu, Y. Zhang, G. Wu, J. Hu, *J. Am. Chem. Soc.*, **128**, 7456 (2006)
140. S. Bovio, A. Podesta, C. Lenardi, P. Milani, *J. Phys. Chem. B*, **113**, 6600 (2009)
141. S. Rivera-Rubero, S. Baldelli, *J. Phys. Chem. B*, **118**, 15133 (2004)

142. C. Aliaga, S. Baldelli, *J. Phys. Chem. B*, **110**, 18481 (2006)
143. A. J. Bard, L. R. Faulkner, *Electrochemical Methods: Fundamentals and Applications*; 2nd ed. p. 541, Wiley Interscience: New York, NY, 2000
144. V. Lockett, R. Sedev, J. Ralston, M. Horne, T. Rodopoulos, *J. Phys. Chem. B*, **112**, 7486 (2008)
145. K. S. Novoselov, D. Jiang, F. Schedin, T. J. Booth, V. V. Khotkevich, S. V. Morozov, and A. K. Geim, *PNAS*, **102**, 10451 (2005)
146. F. Schwierz, *Nat. Nanotech.*, **5**, 487 (2010)
147. M. I. Katsnelson, A. K. Geim, *Phil. Trans. R. Soc. A*, **366**, 195 (2008)
148. M. Ishigami, J. H. Chen, W. G. Cullen, M. S. Fuhrer, and E. D. Williams, *Nano Lett.*, **7**, 1643 (2007)
149. C. H. Lui, L. Liu, K. F. Mak, G. W. Flynn, and T. F. Heinz, *Nature*, **462**, 339 (2009)
150. W. Cullen, M. Yamamoto, K. Burson, J. Chen, C. Jang, L. Li, M. Fuhrer, and E. Williams, *Phys. Rev. Lett.*, **105**, 1 (2010)
151. V. Geringer, M. Liebmann, T. Echtermeyer, S. Runte, M. Schmidt, R. Rückamp, M. Lemme, and M. Morgenstern, *Phys. Rev. Lett.* **102**, 1 (2009)
152. S. P. Koenig, N. G. Boddeti, M. L. Dunn, J. S. Bunch, *Nat. Nanotech.*, **6**, 543 (2011)
153. R. H. Miwa, T. M. Schmidt, W. L. Scopel, and A. Fazio, *Appl. Phys. Lett.*, **99**, 163108 (2011)
154. S. Scharfenberg, D. Z. Rocklin, C. Chialvo, R. L. Weaver, P. M. Goldbart, and N. Mason, *Appl. Phys. Lett.*, **98**, 091908 (2011)
155. T. Yoon, W. C. Shin, T. Y. Kim, J. H. Mun, T.-S. Kim, and B. J. Cho, *Nano Lett.*, **12**, 1448 (2012)
156. Z. Ao, M. Jiang, Z. Wen, and S. Li, *Nanoscale Res. Lett.*, **7**, 158 (2012)

157. A. Rudenko, F. Keil, M. Katsnelson, and A. Lichtenstein, *Phys. Rev. B*, **84**, 1 (2011)
158. F. Wooten, K. Winer, D. Weaire, *Phys. Rev. Lett.*, **54**, 1392 (1985)
159. Y. Tu, J. Tersoff, *Phys. Rev. Lett.*, **84**, 4393 (2000)
160. S. J. Stuart, A. B. Tutein, J. A. Harrison, *J. Chem. Phys.*, **112**, 6472 (2000)
161. D. W. Brenner, O. A. Shenderova, J. A. Harrison, S. J. Stuart, B. Ni, S. B. Sinnott, *J Physics: Condensed Matter*, **14**, 783 (2002)
162. A. Carr´e, J. Horbach, S. Ispas, W. Kob, *Europhys. Lett.*, **82**, 17001 (2008)
163. S. Plimpton, *J. Comp. Phys.*, **117**, 1 (1995)
164. E. R. Cruz-Chu, A. Aksimentiev, K. Schulten, *J. Phys. Chem. B*, **110**, 21497 (2006)
165. S. L. Mayo, B. D. Olafson, W. A. Goddard III, *J. Phys. Chem.*, **94**, 8897 (1990)
166. X. Wu, M. C. Vargas, S. Nayak, V. Lotrich, and G. Scoles, *J. Chem. Phys.*, **115**, 8748 (2001)
167. J. P. Perdew, K. Burke, M. Ernzerhof, *Phys. Rev. Lett.*, **77**, 3865 (1996)
168. G. Kresse, J. Furthmuller, *VASP the Guide*, Vienna University of Technology, Vienna, 2001
169. P. E. Blochl, *Phys. Rev. B*, **50**, 17953 (1994)
170. H. J. Monkhorst, J. D. Pack, *Phys. Rev. B*, **13**, 5188 (1976)
171. S. Grimme, *J. Comp. Chem.*, **27**, 1787 (2006)
172. S. Lee, R. J. Bondi, G. S. Hwang, *Phys. Rev. B*, **84**, 045202 (2011)
173. R. L. Mozzi, B. E. Warren, *J. Appl. Cryst.*, **2**, 164 (1969)
174. B. I. Yakobson, C. J. Brabec, J. Bernholc, *Phys. Rev. Lett.*, **76**, 2511 (1996)
175. A. Incze, A. Pasturel, P. Peyla, *Phys. Rev. B*, **70**, 212103 (2004)
176. K. N. Kudin, G. E. Scuseria, B. I. Yakobson, *Phys. Rev. B*, **64**, 235406 (2001)

177. E_{st} of graphene due to bending can be calculated using a simple formula for bending energy ($E_b = \frac{1}{2}C\kappa^2$, where κ is the curvature and C is bending rigidity). In order to explore this, E_b term is substituted to E_{vdW} (0.93 eV/nm²) in the uniaxial bending energy formula. When C is bounded at 0.85-1.5 eV, it is found that graphene would be off when $D < 1.9$ -2.5 nm. Here, D is the diameter of the rough area, and we considered the symmetric biaxial bending.

Vita

Eunsu Paek was born in Daegu, South Korea on September 15, 1980, the daughter of Yunnam Kim and Youngjo Paek. She received a B.S. degree in Chemical Engineering from Seoul National University, Seoul, South Korea in February of 2004. She received a M.S. degree under the supervision of Dr. Seung Jong Lee in Chemical Engineering from Seoul National University in February of 2006. In June 2006, she entered Graduate School of the University of Texas at Austin. She joined Computational Nanoengineering Laboratory Group and began doctoral research in Chemical Engineering under the guidance of Professor Gyeong S. Hwang. She was admitted to Ph.D. candidacy in February of 2012.

Permanent address: 77-3, Songhyun 2 Dong, Dalseogu
Daegu, 704-342, Korea

This dissertation was typed by the author.